OPTICAL STUDY OF 2-D DETONATION WAVE STABILITY

THESIS

Eulalie T. Grodner, First Lieutenant, USAF

AFIT-ENG-MS-21-M-043

DEPARTMENT OF THE AIR FORCE
AIR UNIVERSITY

AIR FORCE INSTITUTE OF TECHNOLOGY

Wright-Patterson Air Force Base, Ohio

(IF your document is limited, place your Destruction Notice Here)

AFIT-ENY-MS-21-M-043

OPTICAL STUDY OF 2-D DETONATION WAVE STABILITY

THESIS

Presented to the Faculty

Department of Aeronautics and Astronautics

Graduate School of Engineering and Management

Air Force Institute of Technology

Air University

Air Education and Training Command

In Partial Fulfillment of the Requirements for the

Degree of Master of Science in Electrical Engineering

Eulalie T. Grodner, BS

First Lieutenant, USAF

March 2021

AFIT-ENG-MS-21-M-043

OPITCAL STUDY OF 2-D DETONATION WAVE STABILITY

Eulalie T. Grodner, BS

First Lieutenant, USAF

Committee Membership:

Maj L. M. Thomas, PhD
Chair

Dr. S. C. Cain
Member

Maj D. J. Becker, PhD
Member

Dr. F. R. Schauer
Member

AFIT-ENG-MS-21-M-043

Abstract

For this research, detonation wave stability was studied in two different experiments. The first study consisted of using a straight 2-D channel and imaging the detonation traveling down the channel. The second study consisted of using horseshoe-shaped channels and tracking the detonation traveling around a curve. In both cases the waves were tracked using a computer program designed specifically for this research.

High-speed shadowgraph, and Schlieren were performed on a 2-D detonation channel – a channel where the internal flow path was too thin to support transverse waves in one of the dimensions – to study the wave behavior limiting the motion of transverse waves to a 2-D plane. The channel design was 2 inch by 0.25 inch, giving it a channel aspect ratio of eight. The viewing window was 1 inch by 1 inch. Stoichiometric hydrogen-oxygen, ethylene-oxygen and mixed-fuel reactants were diluted with argon or nitrogen to vary reaction rates and thereby detonation speed and cell size. All detonations were allowed to become stable before entering the optical window. A computer program with modern digital image processing techniques was designed to track the detonation. Velocity, optical soot foils, and detonation wave thickness were computed using the computer code. Among the more significant trends observed were: 1) increased variance in velocity with dilution; 2) increase in the thickness of the detonation wave with diluent heat capacity; and 3) decrease in the thickness of the detonation wave with increase in heat of combustion of the reactants. The detonation thickness is believed to correlated to

the difference in position of the combustion wave and shock wave of the detonation corresponding to the commonly named *induction* and *reaction* zones.

High-speed chemiluminescence was performed on rectangular curve detonation channels which had the overall shape of a horseshoe. The channels were designed with varying R_i/R_o to determine impact of the ratio on wave stability. Ethylene-air and hydrogen-air detonations were used with varying equivalence ratios. A computer program was designed to track the inner and outer waves of the detonation as it circled the horseshoe. Different stability regimes were identified based on video and velocity data. It was found the different regimes did correlate to the R_i/R_o of the test section. Diagrams were created to map the different wave stability regimes compared to cell size. One significant finding of this experiment was that detonations were observed to successfully propagate around the full 180-degree curve only when the channel dimensions were wide enough to support four or more cells. For stable waves, smaller cells were preferred. Therefore, the channel design in terms of cell size is critical for wave stability.

For both experiments of this wave stability research, the velocity mean and variance were tracked. In both cases, cell size correlated to wave stability. In general, larger cells correlated with variance in velocity. This variance of velocity correlated with instabilities found in detonation waves.

Acknowledgments

I am grateful for the support of my professors, committee members, and my thesis advisor, Maj Thomas. I am also thankful for the researchers in RQTC who supported me through this research (Matt Fotia, Andrew Knisely, Steve Grib, Rob Fievisohn, and RJ Heckel). Without their support, this thesis would have never ignited and became what it is now.

I am also grateful for my fiancée, who supported me through some broken teeth and a torn shoulder which transpired in the period of writing this thesis. Without her support, writing this thesis would be more than a kick in the teeth.

Eulalie T. Grodner

Table of Contents

Page

List of Figures

Page

List of Tables

Page

OPTICAL STUDY OF 2-D DETONATION WAVE STABILITY

I. Introduction

1.1 Background

There are two types of stable combustion which can occur in engines. These two types are deflagration and detonation. Deflagration is the typical type of combustion found in car engines where a flame will burn the reactants to create energy. In car engines 'knocking' can occur. The most extreme form of knocking is when a detonation occurs. A detonation occurs when a combustion wave passes rapidly enough through the reactants that the pressure waves coalesce into a shockwave. The high temperature produced by the shock heating promotes the high reaction rates required to sustain the rapid combustion wave. When the combustion reaction and shockwave are coupled in this way it is called a detonation wave. Having a detonation occur in an engine designed for deflagration can be dangerous due to the strong and rapid pressure rise. However, engines designed to utilize detonations as the combustion process hold the promise of increased thermodynamic efficiency.

Detonations, when used for combustion, create a pressure-gaining system. This system produces a thermodynamic benefit such as an increase in pressure, higher enthalpy, and lower entropy when compared to deflagration. The T-S diagram helps support this claim over the standard engine T-S. Figure 1 shows the T-S diagram for both the standard engine and the detonation engine. The detonation engine T-S is in blue while the standard engine is in black.

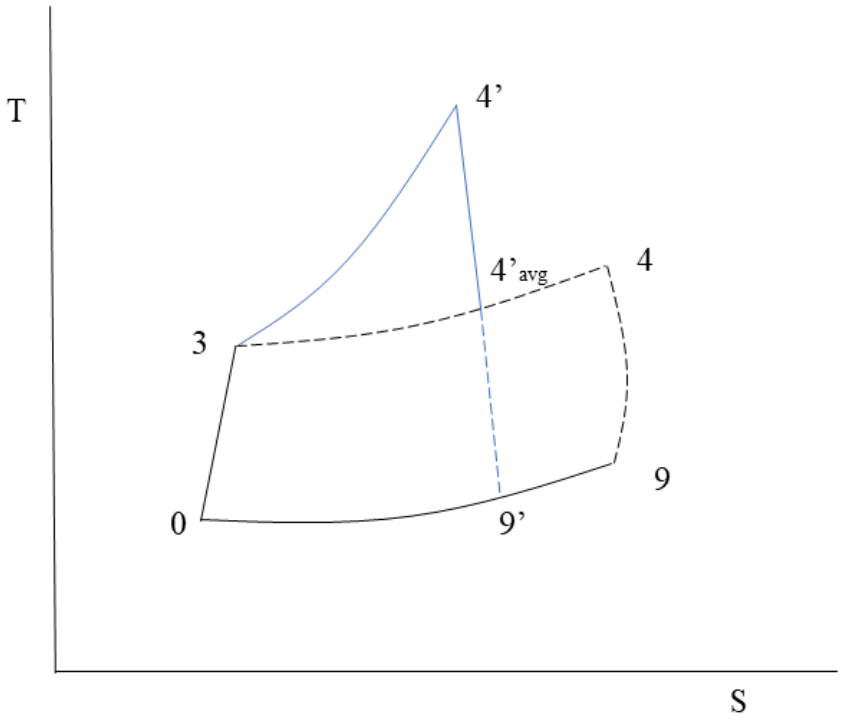

Figure 1. T-S diagram of a detonation engine and a standard engine.

Rotating Detonation Engines (RDE) are a current hot topic for future propulsion systems. RDEs are being researched since they are considered a pressure gaining combustion system. Pulse detonation engines (PDE) are another type of propulsion which is pressure gaining. PDEs send one detonation down the combustor chamber, while RDEs have a continuous cycling detonation rotating in the annulus of the combustor. Due to PDEs having to continuously create new detonation waves while an RDE only has to create one, pressure gaining combustion research has focused on the RDE. But there are fundamental questions about how these engines work such as how detonations propagate.

1.2 Motivation

The purpose of this research is two-fold. The first question this research answers is how detonations propagate when constricted to a 2-D plane. This limits the ability of the detonation wave to move. The detonation itself can only move from front to back of the test section, with the transverse wave limited to moving only left and right of the wave. Through test parameters, the detonation itself is forced to be stable. This will enable the observation of the detonation wave travels when optically resolved, decreasing the error of tracking the wave. High-speed imaging will allow tracking of the detonation and allow the examination of the chemical reactivity of different fuels with varying diluents. The two diluents are nitrogen and argon. Nitrogen is used to better simulate air-breathing propulsion application. The use of argon gives the ability to determine whether the diluent is affecting the chemical reactivity or the heat capacity of the diluent: argon has a higher mass while nitrogen has a larger heat capacity.

The second purpose is to analyze how a detonation propagates around a curve. This is especially important relating to RDE research, because the detonation is continually circulating an annulus. All data will be taken utilizing a high-speed camera. This research uses rectangular round tubes shaped in a horseshoe as a detonation channel. Here 2-D channels are also utilized (but not as constricting as the straight test section). Waves are not restricted to only stable waves propagating, and unstable waves were observed around the curve. The purpose of this section is to classify the different types of wave (stable and unstable manifestations) and why these instabilities occur. This research utilizes ethylene-air and hydrogen-air detonations with varying equivalence ratios (and

ultimately the chemical reactivity). The ratio of the inner and outer radius for horseshoe is varied throughout the different test sections.

Both of these different configurations study different parts of the puzzle of wave stability. The 2-D straight channels studies limiting a detonation to a 2-D plan and how varying the chemical reactivity fundamentally changes the detonation. The horseshoe configuration studies how detonations with varying chemical reactivity and varying construction constrictions vary the wave stability along a curve. They both utilize high-speed cameras and image processing techniques to track and analyze the wave along their given test sections.

1.3 Objective

The primary objective of this research is to apply image processing techniques to the image data sets. From these images, wave velocity can be garnered. From examining how velocity varies throughout the data set, wave stability when compared to velocity can be examined. Comparison of stability with cell size, chemical reactivity, different diluents, and possible operating limits will be made.

1.4 Hypothesis

The main idea behind this research examines how much wave velocity varies with stability. The other part of this research examines how the stability varies with cell size. Velocity in this case is a stand in for chemical reactivity. It is believed that this reactivity varies greatly with the instability wave and larger cell sizes create more wave instability.

For detonations propagating around a curve, it is also believed the ratio R_i/R_o and the cell size effects wave stability.

1.5 Contributions

This thesis contributes to the fundamental detonation research. Using the 2-D channels, the experimental study of how detonations propagate in a 2-D plane can be examined. Dilution is added to two different fuels to examine how wave stability changes. For the study using the horseshoe, how oblique detonations travel can be examined. Different classifications of wave stability will be made and compared to velocity. The radius ratio, R_i/R_o of the horseshoe set up will be examined for wave stability and compared to cell sizes. Further improvements of image processing techniques for detonation waves will be made.

1.6 Thesis Overview

This thesis contains five different chapters. Chapter 2 is a summary of RDE and fundamental detonation research relevant to this research. Chapter 3 is the methodology on how the research was conducted and analyzed. Chapter 4 contains the results and analysis of the research conducted. Chapter 5 contains the summarizes the important conclusions made from this research and why it is important in the grand scheme of detonation research. The chapter also discusses the future work of 2-D channels, and horseshoe detonations.

II. Literature Review

Rotating Detonation Engines (RDE) are being studied extensively because of their potential for pressure gain during the combustion process. They are especially of interest for engines in the hypersonic speed regime, but there are some fundamentals not well understood for RDEs such as detonation wave dynamics. Many research groups use high-speed cameras to help investigate wave dynamics. Image processing techniques can be applied to the RDE data to gain more insight. Optical access to the RDE itself is limited. Optical techniques usually consist of studying the detonation propagating down a straight channel. RDE's inherently have an oblique detonation wave, meaning it is also important to study how detonations curve. This research focuses on advanced image processing and optical techniques used to study fundamental detonation physics.

This chapter covers relevant topics for analyzing and discussing detonations found in two-dimensional linear channels and oblique detonation curved dynamics. Discussion of imaging techniques typical for combustion applications are presented in Section 2.1. Basics of image processing and their application to RDEs are presented in Section 2.2. Discussion of how imaging is done to capture the detonation dynamics in a wave is presented in Section 2.3. A specific way of capturing detonation dynamics in a Linear RDE, along with their detonation structure are presented in Section 2.4. Two-dimensional linear channels with their cell structures are presented in Section 2.5. Curved detonation dynamics are presented in Section 2.6.

2.1 Imaging Techniques

Schlieren imaging is a technique used to visualize changes in density gradients found in the air. The basic principle of Schlieren imagery is a laser sources shines light to a mirror. The mirror collimates the light into parallel rays. The columnated light then passes through the region of interest. Density gradients from the region of interest causes the light to bend. The incoherent light then comes to another mirror. The second mirror focuses the light to a knife edge. The knife edge cuts the light in half, as well as removing the light bent by the density gradients. The light continues to the camera. In the image produced, the density gradients appear as dark lines since the bent light was cut by the knife edge. This technique is very useful in imaging shockwaves or simple density gradients presented in the air, such as a candle's plume [1].

Planar Laser-Induced Fluorescence (PLIF) is an imagining technique used for gaining qualitative information on species concentration, temperature, pressure, or density. The basic principle for PLIF is the laser excites the photons up an energy level and causes the photons to fluoresce. The fluoresce is captured in image. Figure 2 is a diagram of a typical PLIF set-up. PLIF can be divided into three different categories: excitation, detection, and post-processing. For excitation, usually a pulse laser is chosen due to the pulses creating a short lifetime of fluorescence (about 100 ns). Wavelengths of the laser are chosen based on what species selected for excitement. Typical species used are O_2, NO, H_2O, and OH. Species imaging results in intensity maps, which in the case for combustion are useful for locating flames, burned/unburned regions, recirculation zones and shockwaves. Temperature imaging is typically done using two different lasers

(but there are monochromatic methods). Temperature imaging using PLIF, is complex and requires multiple cameras, making it cost prohibitive. PLIF is capable of exciting multiple wavelengths. Often, the intensities are much weaker than if one-color PLIF, but the lesser intensity values can be overcome by using an intense laser source. For processing images produced by PLIF, typically image correction is done first. After applying image correction, image enhancement, transmission, and pattern recognition can be applied. One of the main combustion applications of PLIF image processing is gaining structural data such as turbulent eddies and location of flame front [2].

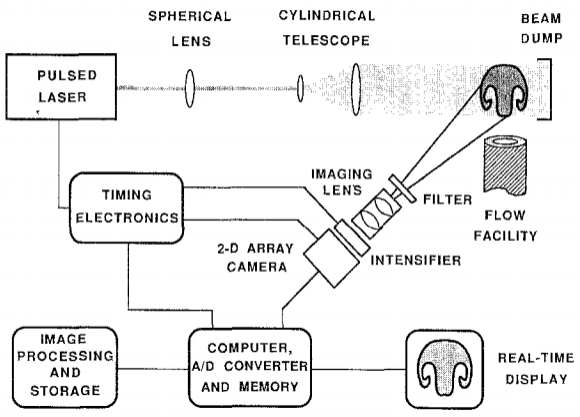

Figure 2. Schematic for a typical set-up using PLIF [2].

2.2.1 Image Processing Basics

The Fourier transform is a mathematical tool used across many different engineering and mathematic disciplines. Fourier transforms are mostly done to find a frequency of an event in a time-based signal. This is not always the case with a two-dimensional Fourier transform being done on an image. The technique was to look at a

frequency of an event, but the event does not necessarily need to be time. To get a real image in the frequency domain, a two-dimensional discrete Fourier transform must be done. Equation 3.1 is the discreate Fourier transform.

$$G_{p,q} = \sum_{n=0}^{N_X-1} \sum_{m=0}^{N_y-1} g_{n,m} \exp\left(-j2\pi\left(\frac{np}{N_x} + \frac{mq}{N_y}\right)\right) \quad \textbf{(2.1)}$$

The representation of an image in the frequency domain can be manipulated by multiple transfer functions which also modify the reconstructed image when transformed back into the spatial domain. To take an image out of the frequency domain into the spatial domain, a two-dimensional inverse Fourier transform must be applied. This process of modifying an image in the frequency domain is called frequency domain filtering. Equations 2.2 is the discrete inverse Fourier transform [3].

$$g_{n,m} = \frac{1}{N_x N_y} \sum_{p=0}^{N_x} \sum_{q=0}^{N_y-1} G_{p,q} \exp\left(j2\pi\left(\frac{np}{N_x} + \frac{mq}{N_y}\right)\right) \quad \textbf{(2.2)}$$

Spatial filtering is one of the fundamental tools to image processing. Typically, with a spatial filter, the value of an individual pixel is considered with respect to the values of neighboring pixels. The neighborhood performs an operation on the original image based on the pixels in the neighborhood. One common spatial mask is the convolution filter. Convolution can be thought of as a flip and a slide, where the mask is

flipped 180 degrees than slid over the image. Equation 2.3 is the mathematical equation for convolution [4].

$$g(x,y) * h(x,y) = \sum_{s=-a}^{a} \sum_{t=-b}^{b} g(s,t)h(x-s,y-t) \quad \textbf{(2.3)}$$

In the equation g is the image while h is the mask being applied. The image size is m by n, with m and n being the pixel count in a given direction. The variable a is equal to (m-1)/2 and the variable b is (n-1)/2. [3] Convolution can also be done by applying a Fourier transform on both the mask and the image, multiplying them together, and then taking the inverse Fourier transform [3].

There are two types of spatial filters. Filters belonging to the first type are known as linear spatial filters. A linear spatial filter must have coefficients in the mask which perform linear operations onto the actual image. An example of a linear spatial filter is a lowpass filter otherwise known as an averaging filter. The basic rule for an averaging filter is the sum of the neighborhood must equal one. The second type of spatial filters are known as non-linear. An example of a non-linear spatial filter is the median filter. The way median filtering works is it considers the neighborhood of values and selects the median value to assign the point to. The median filter forces intensity fluctuations to be more like their neighbors. It is highly effective in reducing speckling found in an image [4].

2.2.2 Edge Detection/Curve Fitting

Edge detection can be done by using non-linear, first-order derivatives by use of gradients. Derivatives are linear operators, but calculating the gradient is non-linear. The gradient works by calculating the change occurring in both the x and y direction and then taking the magnitude of these changes. The masks, when summed, always equal zero. One popular gradient mask employs the Sobel operators. Below are the Sobel operators, and how they are used as a gradient operator.

$$g_x = \begin{matrix} -1 & 0 & 1 \\ -2 & 0 & 2 \\ -1 & 0 & 1 \end{matrix} \quad \textbf{(2.4)}$$

$$g_y = \begin{matrix} -1 & -2 & -1 \\ 0 & 0 & 0 \\ 1 & 2 & 1 \end{matrix} \quad \textbf{(2.5)}$$

$$M(x,y) = \sqrt{G_x^2 + G_y^2} \quad \textbf{(2.6)}$$

The Sobel operators, g_x and g_y are the masks applied to the image. G_x and G_y are the changes found their respective directions. G_x and G_y are the same size as the original image. They are then both summed and taken the magnitude, M(x,y). The image produced from the magnitude shows the edges found in the image [4].

The Taubin fit estimates a position in relation to a planar curve. It is a dimensional independent technique designed for curve fitting, but with the main focus for

2-dimensional and 3-dimensional fits. It works by minimizing a means square distance from a set of data points. This minimization of mean squares further reduces into a generalized eigenvector fit. [5]

2.2.3 Application of Imaging Techniques to RDE

Bennewitz [6] uses a slew of different image processing techniques to determine the number of waves and wave speed for a rocket RDE. Rocket RDEs can have up to seven different waves and be moving in both CW and CCW directions [6, 7]. Figure 3 gives a visual demonstration how they determined location of the waves for the series of images. Images are taken from a top-down view of the RDE. The raw image is taken, and background subtraction is applied to all images in the set. A cartesian mesh is applied to find the locations of the annulus. The top 100 boxes based on intensity are used for the Taubin fit. The Taubin fit gives the location of the origin of the annulus, through use of curve fitting. Using location of the origin, a polar mesh is applied to the images. An azimuthal bin was created to contain all the angles with their intensity values. The mesh consisted of 200 bins, each bin being 1.8 degrees.

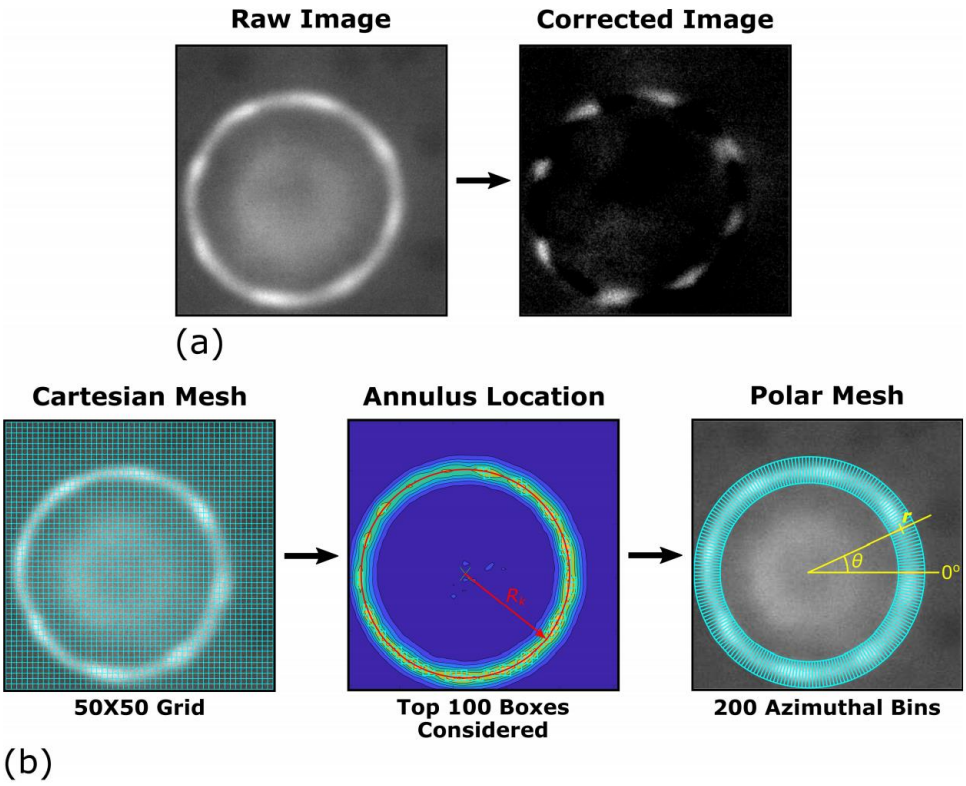

Figure 3. Order of steps taken for the azimuthal bins to be created [6].

The intensity values are placed in the azimuthal bins for each image. A new image is created using the intensity values and the time stamp for each frame. A two-dimensional Fourier transform is done to calculate the frequency, number, and direction of the waves. Figure 4 contains the image of the azimuthal bins in a while b shows the Fourier transform and how the number, direction and frequency of the waves are calculated.

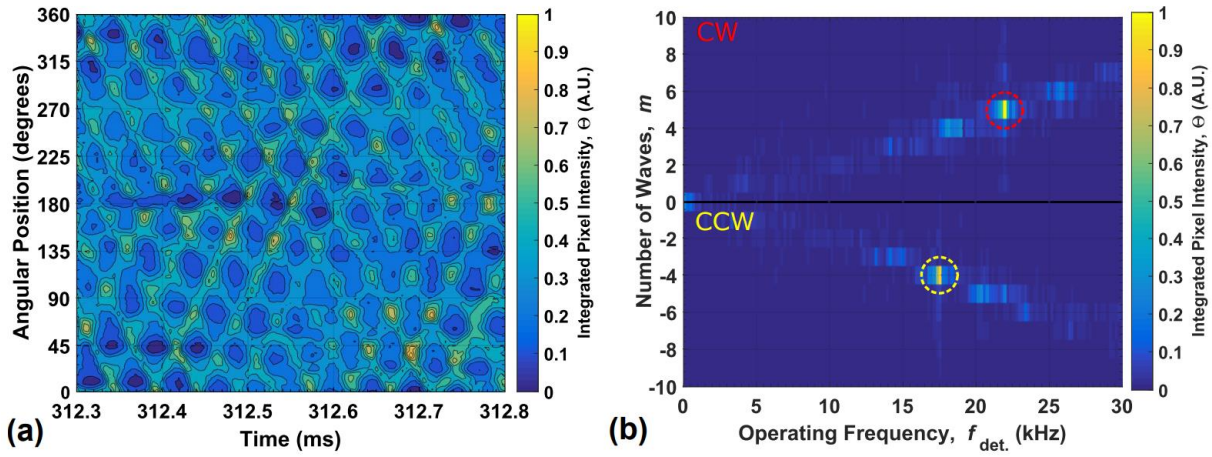

Figure 4. (A) Azimuthal bins with corresponding angles for time of series of images. (B) Fourier transform of A [6].

2.3. Wave visualization in RDE

To gain optical access to an RDE for purpose of studying detonation dynamics, Chacon [8] used a racetrack RDE. As the name describes, the RDE looks like a racetrack, with long straightaways with curves connecting the two straightaways. Optical access is obtained by having a window placed in one of the straightaways. OH PLIF visualization are performed using the optical window in the straightaway. High-pressure transducers are utilized to correlate events observed in the optical window to other events occurring in the racetrack. Chacon used the racetrack RDE to identify flow field features of the detonation wave.

The flow field features are identified and labeled in Figure 5. In the figure, DW stands for the detonation wave, CC stands for commensal combustion, CB stands for contact burn (a number one follows it in the image), BR stands for buffer region, FFR is

fresh reactants, AIK is auto ignition of a kernel, and PC marks the parasitic combustion. The CC region occurs due to chemical reactions happening after the detonation wave has passed. CB occurs when the fresh reactants come into contact with the products. The BR occurs when no chemical reactions occur. In Figure 5, the BR region is between two CB regions [8].

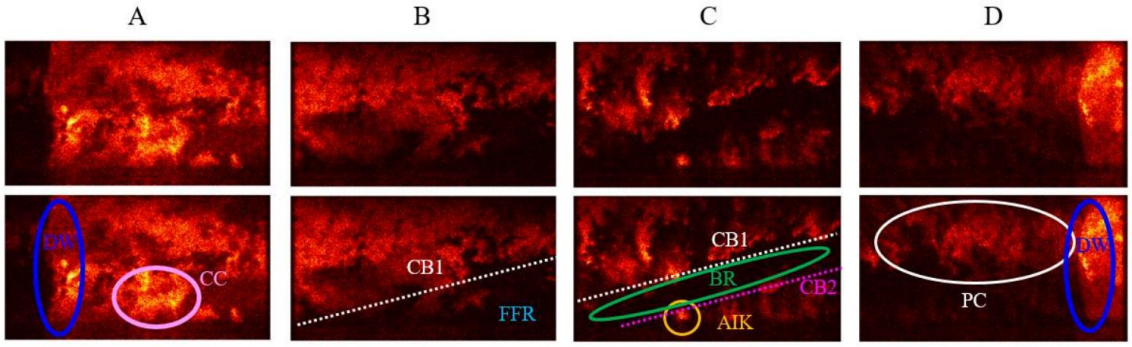

Figure 5. OH PLIF visualization of detonation wave in racetrack RDE. [8]

Another way researchers have gained optical access to an RDE is making the RDE entirely out of quartz [9]. Cho [9] performed OH chemiluminescence within the quartz RDE using a high-speed camera. A second high-speed camera is used to study the wave dynamics at the top of the RDE. For this study, ethylene-air was used. The equivalence ratios all varied slightly around one. Lift-off occurred for the ethylene-air mixture due to poor mixing. The region between the detonation wave and the oblique shock was noted for its low temperature. The low temperature region was caused by left-over products quenching from the previous RDE cycle [9].

2.4 Linear RDEs

Linear RDEs can be thought of as an RDE which has been ‘unwrapped’. Figure 6 is an example of an RDE that has been unwrapped [10]. The reactants are supplied axially, passing through the injection boundary. The detonation wave flows in the x direction. The wave itself can leave the linear portion in both the x and z direction. One of the reasons for using a linear RDE, instead of a normal RDE, is to gain optical access to wave dynamics in an RDE.

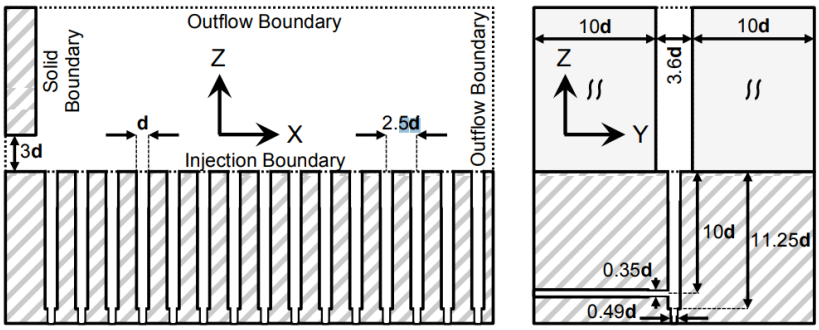

Figure 6. Schematic of a linear RDE [10].

Burr and Yu [10] studied a linear RDE with the purpose for analyzing the flow structure of a detonation in an RDE like environment. Their specific linear RDE was built with the purpose of simulating a six-inch RDE. Layout of the RDE is featured in Figure 6. Injection holes are at the bottom. The image on the left is the plane in which the detonation travels through. The detonation travels in the x-direction with new reactants being pumped in the z-direction. The image on the right is the plane in which the detonation exits. The linear RDE ran on ethylene and oxygen [10].

Images were taken using high-speed Schlieren and shadowgraph imagery. Results of the experiment detailed regions on the detonation wave before and after passing over the reacting gas. These results are shown in Figure 7. The numbers in the left image in Figure 7 detail the region of the detonation wave. The region **I** is the background gas, region **II** contains the reactant-cross flow, region **III** is where the reacted gas is, region **IV** is background gas that has experienced a shock wave. The letter A marks the detonation front, while the letter B marks the oblique shock wave. The letter C marks where the reacted gas and unreacted gas interact, the letter D marks where the purged gas and the reactants interact, and the letter E marks the shocklets that occur in region **IV**. Last, the letter F marks the transverse waves. Transverse waves are found in the image, which indicates the existence of triple-points. Detailing where the triple points were and determining the cell size was not possible in this rig configuration. The reason for the inability to determine cell size is the ability of the transverse waves to travel in three dimensions [10].

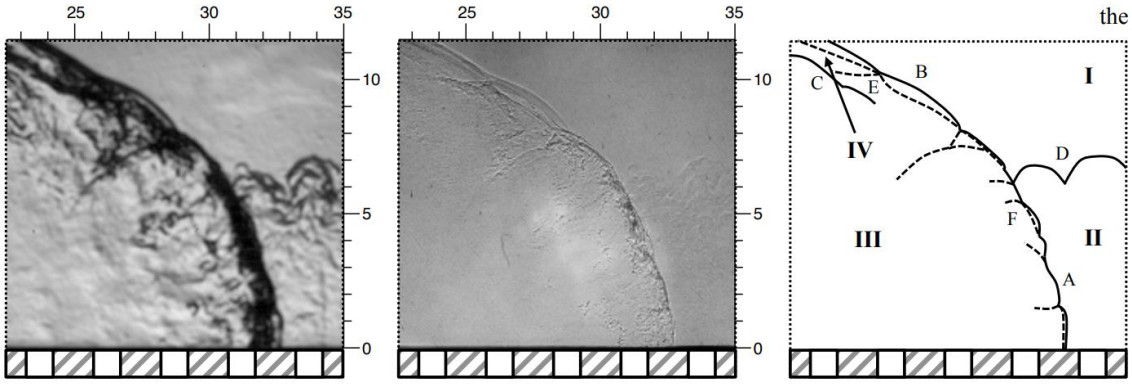

Figure 7. Image on left is Schlieren image of detonation in Linear RDE, image in the middle is shadow graph of the same detonation, and image on right is cartoon drawing with labels indicating regions of the detonation. Figure taken from [10].

A ρDE is an RDE connected to a linear channel. Sosa [11] describes the purpose of the ρDE is to produce repeatable detonations at a high frequency through the linear channel. Chambers [12] used the ρDE to study how turbulence intensities affect the detonation wave propagation dynamics. To create the turbulence, a castellated obstacle (such as a nut or bolt) was added to the linear portion. Her research used hydrogen-air, with equivalence ratios varying but mass flow held at a constant 2 lb/s. Conditions found in the RDE portion were the same in the linear portion. For imaging of the linear portion, Schlieren was used along with a high-speed camera operating at 30 kHz. Images of the linear portion without the castellated objected were compared to images with the castellated object inserted. Figure 8 depicts the comparison of the two different configurations. The image on the left corresponds to the run without the castellating object inserted into the linear portion of the ρDE, and images on the right correspond to the castellated run in the linear RDE. Both ran hydrogen-air at stoichiometric conditions. The only noticeable difference between the baseline run and the castellated run were the reacting jets found in the turbulent run [12].

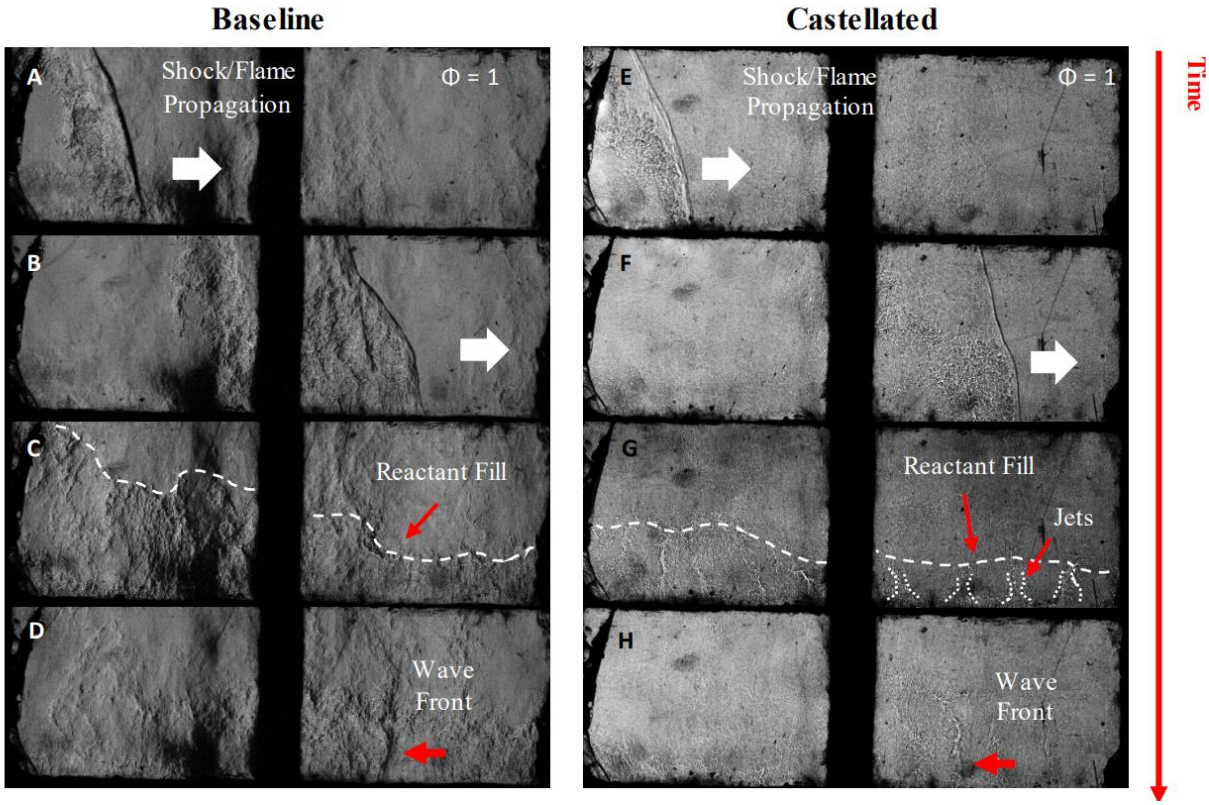

Figure 8. Detonation wave produced in linear section with and without turbulence. Sequence of images is in descending order. All images appear cut in half due to the strut on the window [12].

2.5 2-D Linear Channels

Detonation tubes are used to find information pertaining to the detonation cell size and ultimately their structure. Cell structures can be identified by using soot foils or Schlieren imaging. Figure 9 is a diagram of a shock tube from Fugger [13]. Fuel and oxidizer flow into the tube and are ignited by the spark plug. The flame then undergoes a deflagration to detonation transition (DDT) process, allowing a detonation to be image in the optical portion [13].

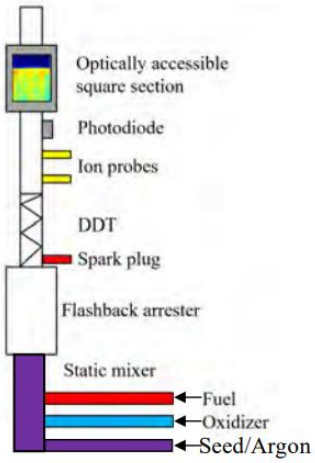

Figure 9. Schematic of a detonation tube from [13].

Two-dimensional channels are designed in a way in which the transverse waves cannot travel in the third dimension. The reason for constricting the transverse waves is to get an accurate description of the cell structure. The majority of two-dimensional channel research has been conducted on a large-aspect-ratio channel at the Narrow Channel Facility (NCF). The aspect ratio at the NCF was 8.44 with the actual dimensions being 152mm by 18mm. NCF also uses eight different detonations to create their detonation front. The reason for doing this is to reduce the length of the detonation tube [14,15,16].

The triple points in the shock wave are what create the cells. Figure 10 shows the diagram of how triple points occur with labels for other significant features. Figure 10 also contains a soot foil of $2H_2$-O_2-17Ar with the cells showing. Triple points occur due to the transverse waves colliding with one another. These transverse waves move

perpendicular to the detonation wave. Transverse waves can move up and down throughout the wavefront, allowing collisions to happen. After these collisions occur, gasses can form behind the Mach stem, slowing the localized wave velocity until another triple point occurs, speeding up the local wave. Soot foils can be used to capture the cells of the detonation. The regularity of the cells in the soot foil can help qualify the stability of the detonation [16]. Figure 11 shows images of a detonation wave propagating down the narrow channels sequentially. The mixture was $2H_2$-O_2-17Ar at a pressure of 20 kPa. The FOV of the image is 138 mm while time between images is 1.7 μs [15].

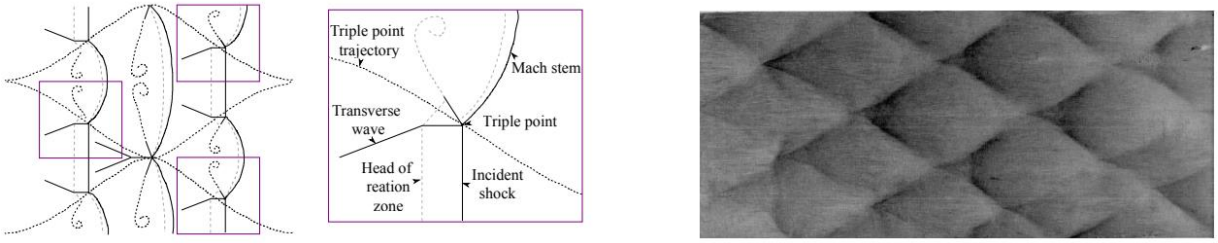

Figure 10. (a) is cartoon of the detonation structure (b) is a soot foil showing the cells of a detonation [16].

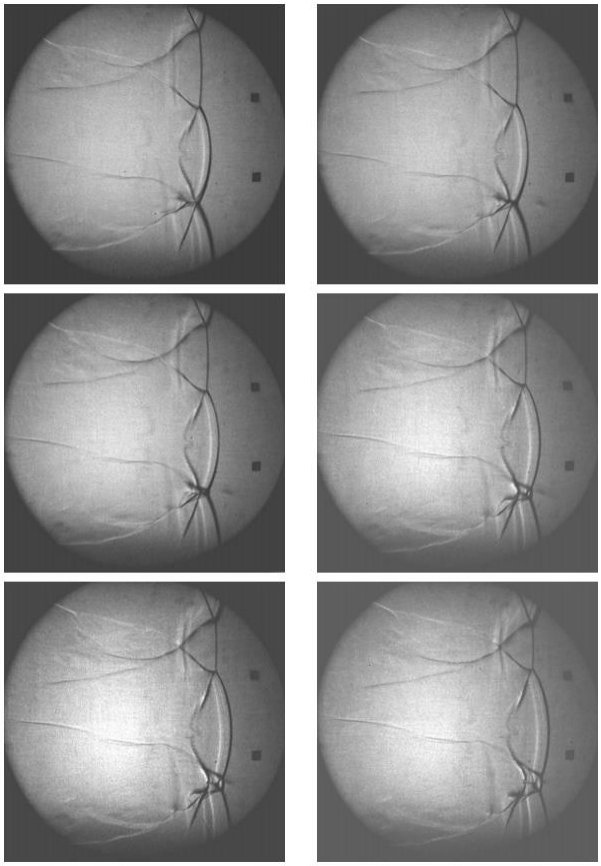

Figure 11. Detonation wave propagating down the narrow channel [15].

Stability of the wave can be determined through visual inspection. Figure 12 presents detonation waves in decreasing stability. Wave separation can lead to a Mach stem, and keystone formation. Figure 13 shows development of the Mach stem and the keystone sequentially. Images are taken 10.1 μs apart. Formation of the Mach stem can be examined in frames (b) and (c). Further separation occurs in frames c and d until the transverse waves hit the top of the tube. A keystone structure development can be examined in frames f and g. Figure 13 is under the same conditions as Figure 12, frame (e). It is considered moderately unstable with a mixture of $2H_2$-O_2-$5.7N_2$ [16].

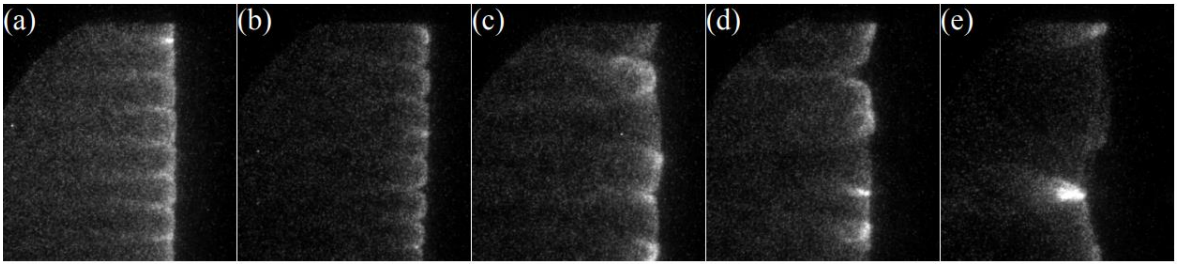

Figure 12. Chemiluminescence of detonation waves in order of decreasing stability with (a) being the most stable and e being the most unstable. [16]

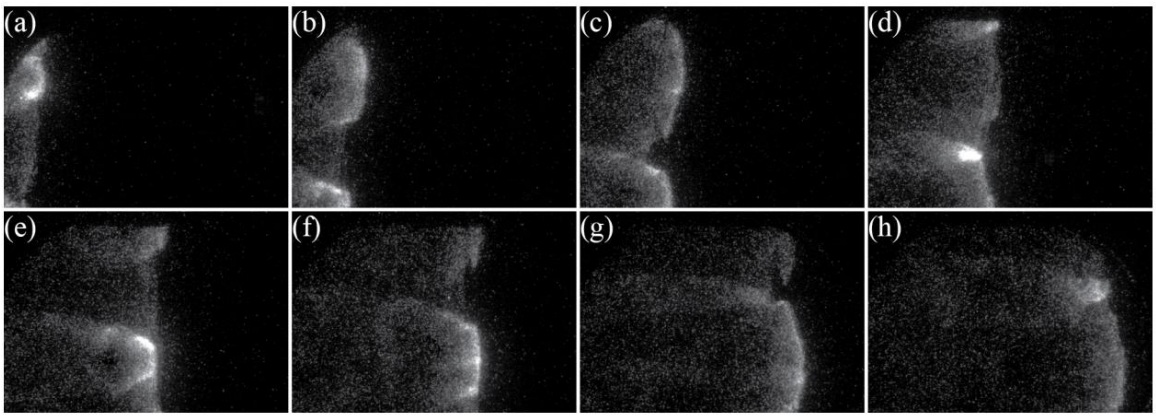

Figure 13. Chemiluminescence of an unstable detonation wave propagating down the narrow channel. [16]

Unlike the NCF, Cho and Fugger [13,17] used one detonation in their narrow channel. Their detonation channel was 12.5mm by 12.5 mm. Cho [17] used both formaldehyde PLIF and PIV to visualize the detonation wave front in a linear detonation tube. Both PLIF and PIV were performed separately for this experiment. PLIF was performed using 355 nm, burst-mode laser. A bandpass filter of 380-420nm was used to spectrally select the chemiluminescence signal, and a high-speed camera was used to capture images. PIV was done using a 532-nm pulse and CMOS camera. Cho performed

line of sight chemiluminescence to image the detonation wave moving from top to bottom in Figure 14. Figure 15 is an image from Figure 14 with an edge detection algorithm performed. The shear layer can be seen with the separation occurring. Even in the small 2-D channel, unburned pockets of fuel can be examined. The curve of the Mach shock can be seen using the edge detection, as well as the incident shock.

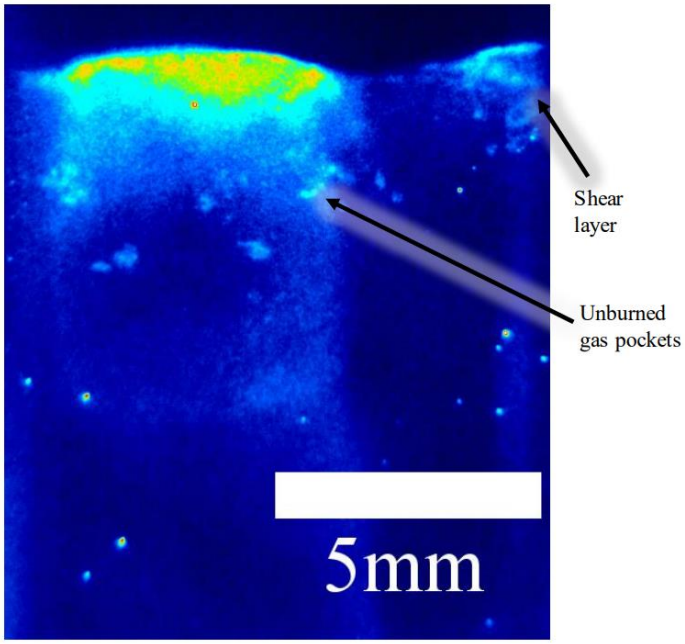

Figure 14. Image is of Formaldehyde PLIF performed on a detonation in the linear detonation channel. Detonation is moving from bottom to top in image [17].

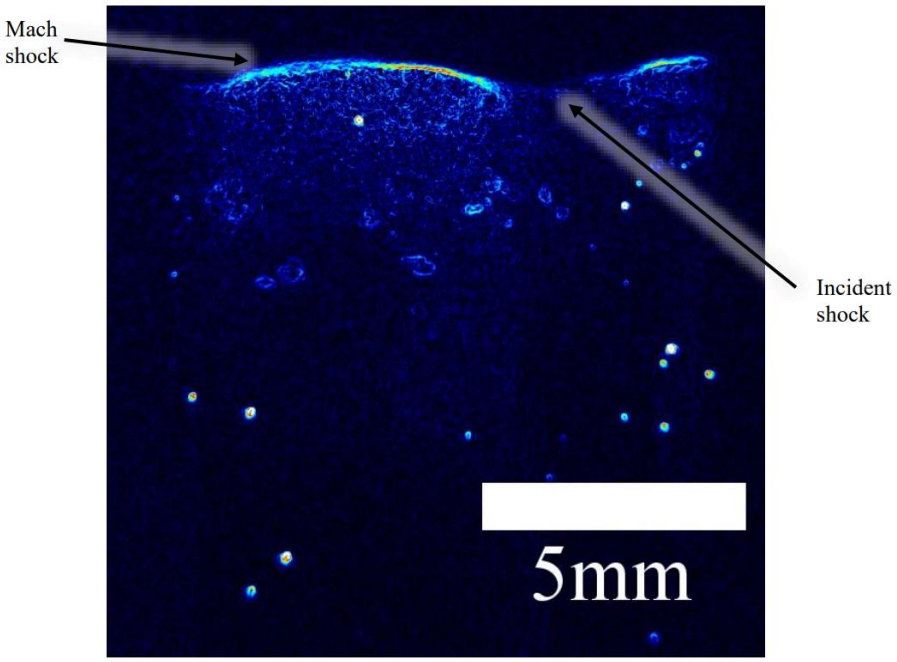

Figure 15. Detonation wave with edge detection algorithm applied [17].

Physical soot foils are not always needed to see the cells of a detonation. Optical soot foils can be created as well. Fugger [17] created these optical soot foils through use of Chemiluminescence and PIV. Figure 16 is an example of an optical soot foil from Fugger. These optical soot foils are created by taking the peak intensity of the transverse waves and combining all these peak intensities during specific time intervals. All images were taken using a Shimadzu camera operating at the 1-10 MHz range. The mixture in the detonation tube was nitrous-propane at stoichiometric equivalence. Even though the detonation tube was considered 2-D, the transverse waves still traveled in all three directions. The highest intensities did not necessarily correspond to the triple point locations do to the three-dimensional nature. The cells in the figure do not necessity have

the diamond shape typical of a cell due to ambiguity of where the triple points occurred [17].

Figure 16. Optical soot foil formed at 10 MHz [17].

Cho [18] applied two color PLIF to the 12.7mm by 12.7mm linear channel. Two color PLIF was chosen due to its ability to work in a wide-range of operating conditions. Two-MHz chemiluminescence was also used during the experiments to assess the detonations' quality. The molar fraction for the experiment was maintained as $2H_2+O_2+3D$, with D being either Nitrogen or Argon. Nitrogen and argon acted as the diluent/seed for the experiment. Figure 17 shows the chemiluminescence of the detonation diluted with Argon. Figure 18 shows the chemiluminescence diluted with Nitrogen. The argon-diluted detonation wave presented a uniform detonation wave front,

with the wave being straight. The detonation wave diluted with nitrogen was non-uniform, with the wave front being jagged.

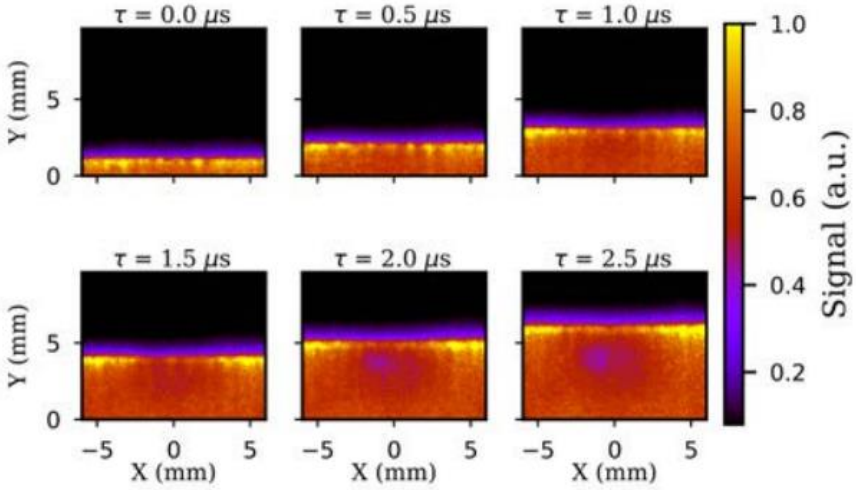

Figure 17. Image is of detonation front in the linear channel using argon as the diluent. Detonation wave flows in the positive y-direction [18].

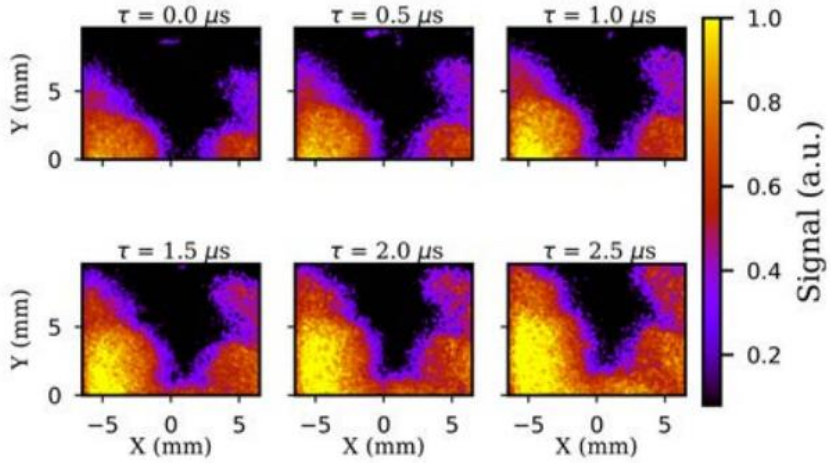

Figure 18. Chemiluminescence imaging at 2-MHz of the detonation wave with nitrogen as the diluent. Wave moves in the positive y-direction [18].

To examine how cell size is affected by the ratio of diluent and oxygen, the ratio was varied for both nitrogen and argon. Changing the ratio of argon to oxygen did not significantly change the cell size. Varying the ratio of nitrogen to oxygen did affect the cell size. Figure 19 shows the results of the variation. [18]

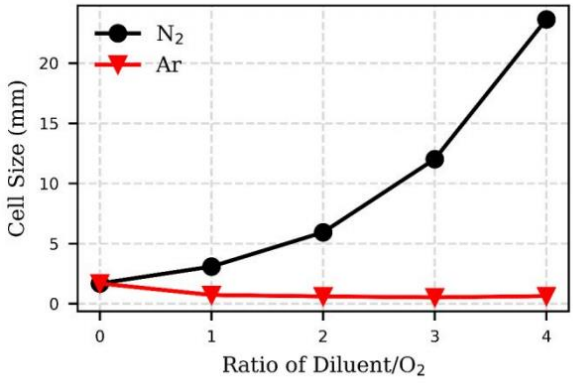

Figure 19. Comparison of cell sizes for nitrogen and argon diluent [18].

2.6 Wave Dynamics

The main component of an RDE is the detonation wave rotating around an annulus, meaning that the detonation wave must behave according to the physics of an oblique detonation. These physics introduce some complications. Rotating around can lead to wave death but also lead to the wave increasing wave speed. The inner radius of the wave can lag the outer wave at one instant, but then suddenly be leading based on interactions among the transverse waves. There are three different regimes of stability for a wave circulating an annulus: stable, unstable, and critical [19]. Figure 20 is a diagram of a detonation wave propagation in the curved channel. Figure 21 is an image showing

how a stable detonation wave propagates down a curved channel. The reason the inner portion of the wave is slower than the outer portion of the wave is due to the expansion waves from the inner wave [20].

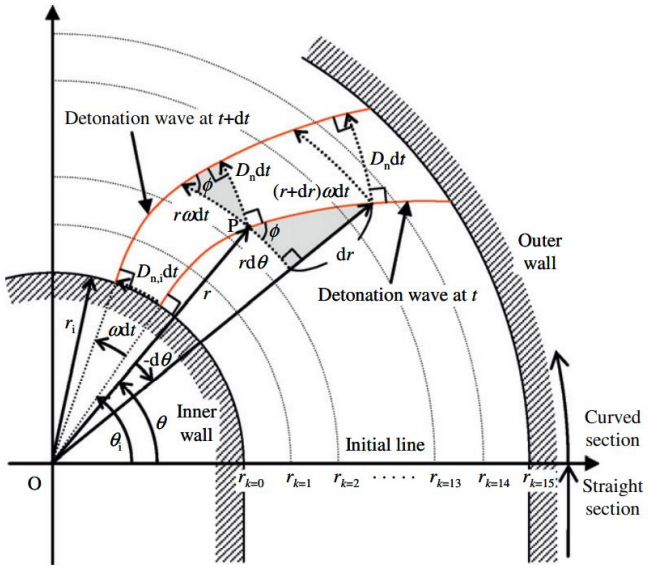

Figure 20. Geometry of how a stable detonation propagates around a curved channel [20].

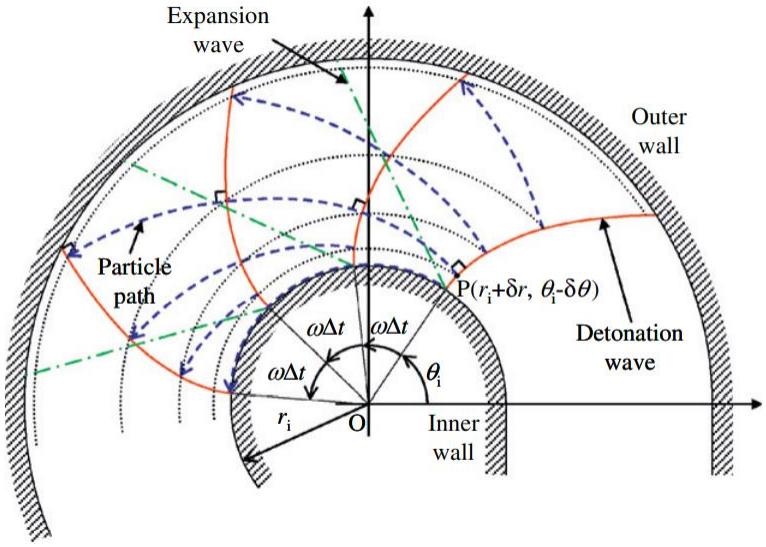

Figure 21. Diagram of how a stable detonation wave propagates down a curved channel [20].

Kudo[19] studied these oblique waves and how they propagated around rectangular tubes in a circle. Wave speeds were determined using piezoelectric sensors, and speeds were compared to the results from the high-speed camera. Figure 22 shows stable and unstable waves propagating at different radii. Lower radii and lower pressures produced unstable waves. Figure 23 is a graph of how the non-dimensional detonation speed varies for the three regimes as a function of wave angle. The non-dimensional variable is found by non-dimensionalizing the perpendicular detonation velocity by the detonation velocity found in the straight portion of the tube [20].

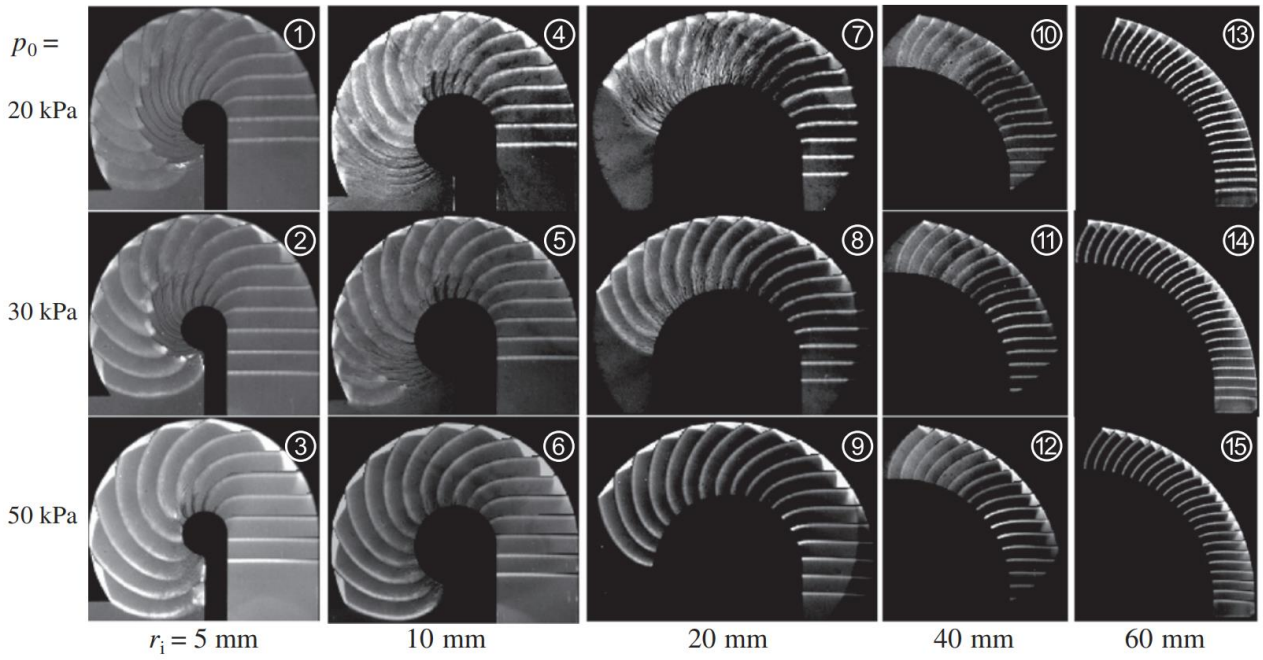

Figure 22. Images are of detonation wave fronts that have been over-lapped. Images 9, 11, 12, 14l 15 are steady waves. Images 1-8, 10 and 13 are unsteady detonations [19].

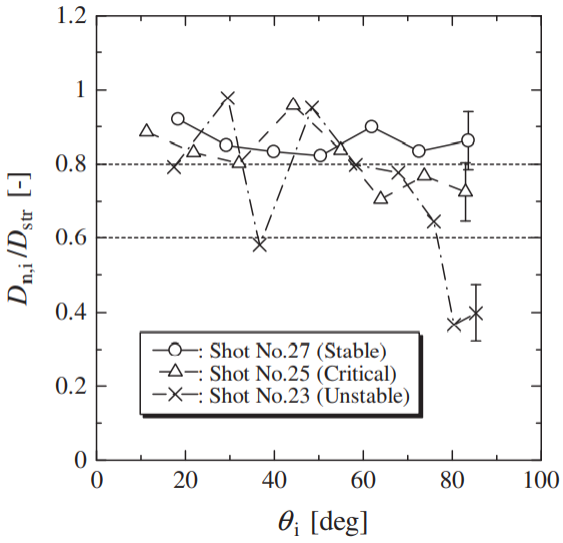

Figure 23. Non-dimensional detonation speed vs. wave angle for stable, critical, and unstable waves [19].

Inner waves can run at slower speeds than the CJ point. The inner wall detonation speed is slower due to the expansion wave [19]. The expansion wave causes the detonation velocity normal to the wave to decrease. The expansion wave effects are closest to the inner radius, meaning the detonation wave speed in a stable wave will be the smallest at the inner radius [20]. Figure 24 shows the inner wall velocity versus the angel of the wave. The rapid increase in velocity for the radius of 10 mm and 5 mm is attributed to the wave reinitiating [20].

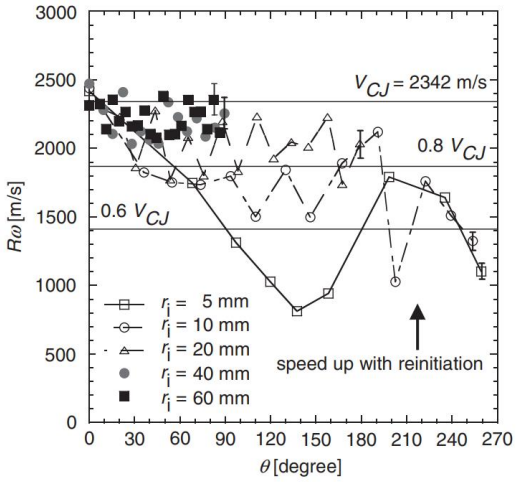

Figure 24. Inner wall detonation velocity vs. angel of the wave [20].

Figure 25 shows a re-initiation event through chemiluminescence of an unstable detonation [21]. The equivalence ratio was 1.2 for a hydrogen-air mixture. The frame rate was 10,500. Frames VI and VII are quite important as they show the inner wave lagging behind and then catching up. After the re-initiation event, the inner wave catches up with the outer wave, allowing the detonation take up the full channel width. An oscillating behavior can be observed before the wave had been reignited. This oscillating behavior is

caused by the wave of the inner radius diffracting and extinguishing. Once the diffracting wave glances off the outer radius, reignition can occur.

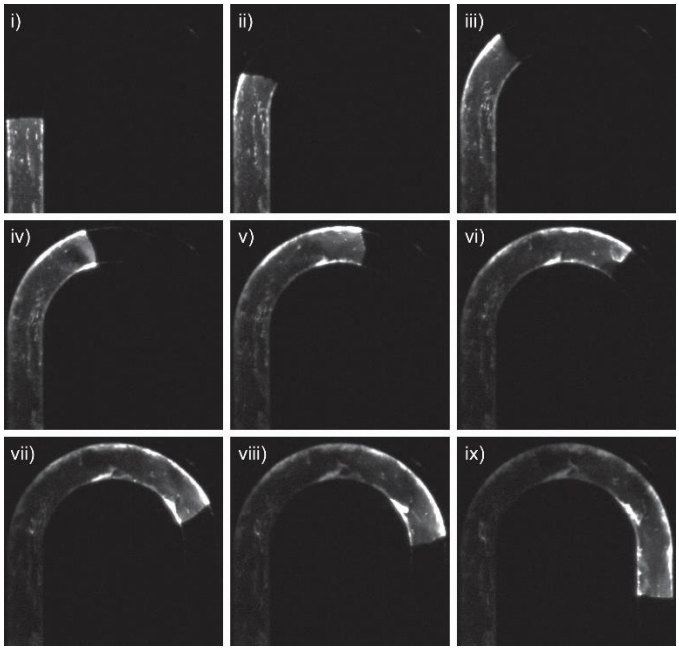

Figure 25. Chemiluminescent of a detonation in a curved channel at 10,500 fps. Detonation was classified as unstable. Detonation was hydrogen-air with equivalence ratio of 1.2 [21].

Cells can be observed in the detonations through use of photography techniques such as short-time open shutter photography (SOP). SOP works by having the exposure time be of a few microseconds. Through this method, only the triple points are imaged. Multi-frame SOP occurs when SOP is performed for each frame. This allows the images to be superimposed, allowing the full cell-structure to take shape [20]. Figure 26 shows MSOP on stable, critical, and unstable detonation. For all images in Figure 26, the radius was 40 mm. Cells structure vary widely depending on what regime the wave is operating [20].

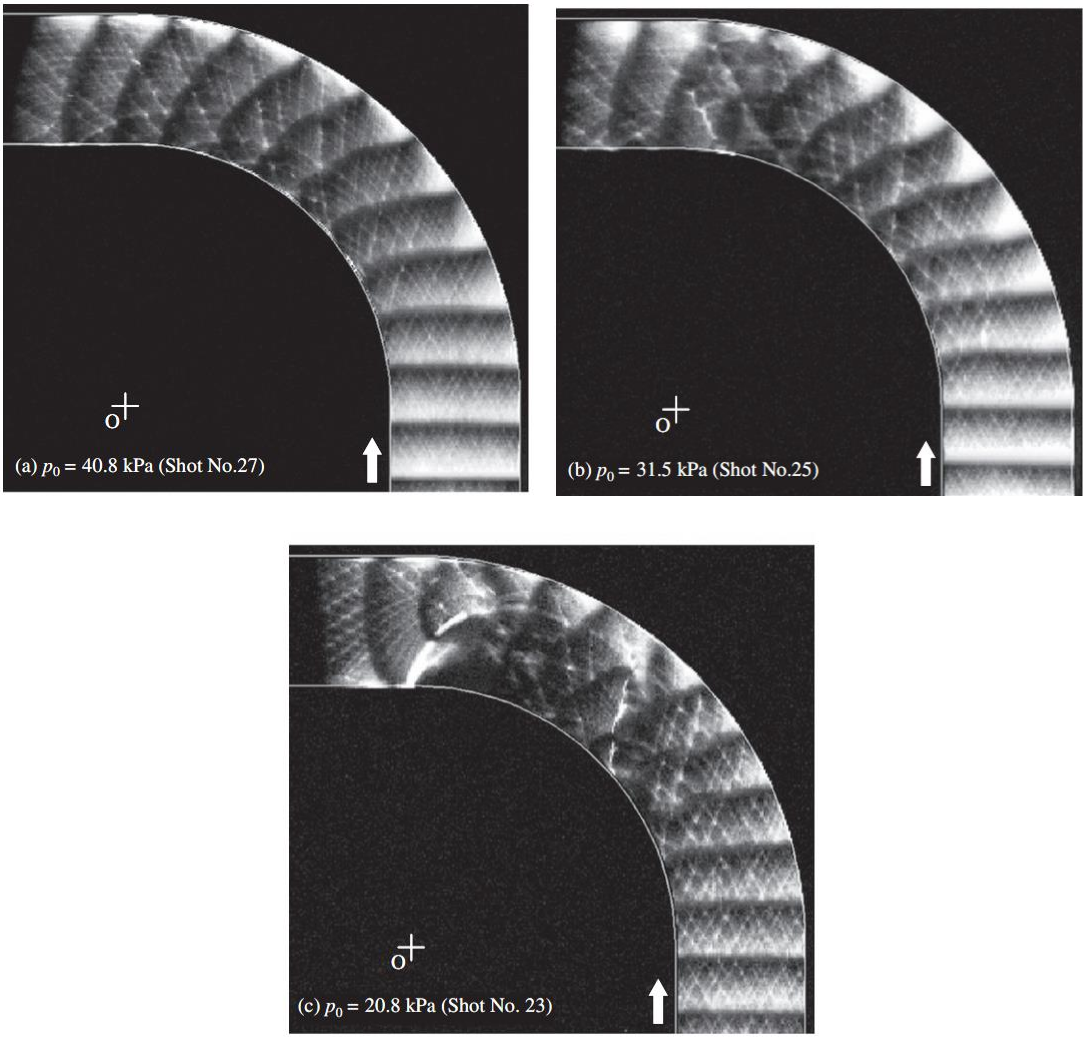

Figure 26. Cell structure of three different regimes of a curved detonation. Figure (a) is stable, (b) is in critical mode, and is in unstable mode. All figures had a radius of 40 mm [20].

III. Methodology

3.1 Pre-Detonator, Pre-Mixed Two-Dimensional (2-D) Channel

The purpose of the pre-detonator, pre-mixed 2-D channel is to further the research on two-dimensional detonation waves. Previous research has been done using the Narrow

Channel Facility (NCF) [14,15,16]. The purpose of making a channel two-dimensional is to force the transverse to only move left, right, and down the path of the detonation wave, ultimately suppressing the transverse waves. Making the waves as such will enhance the structure of the detonation allowing further study on cell sizes and the movement of these transverse waves. Additionally, the line-of-sight optical methods used in this research integrate in this third spatial dimension. By constraining the flow path to the two dimensions perpendicular to the optical path, a major source of error is eliminated. The rest of Section 3.1 will discuss the method on which the 2-D channel has been researched.

3.1.1 Shock Tube Set-up

The detonation tube set-up was similar to Fernilius [22] and Gribs [18]. Alicat flow controllers were used to control the gases for the experiment. The fuel, oxidizer, and diluent were then mixed. Once mixed, the gases passed through a flame arrestor. After the flame arrestor, a spark plug ignited, causing deflagration. A deflagration-to-detonation (DDT) spiral was placed after the spark plug, initiating the detonation process. A view port was placed further downstream allowing placement of a photodiode to act as a trigger for the timing control and data acquisition system. The detonation then passed through a transition section, an extension section in some cases, and then the optical test section.

A transition section was created to bring the detonation from quarter-inch tubing to the rectangular-shaped test section. The transition section was made from stainless steel. The transitional section starts from a quarter-inch circle in cross section and then

diverges into an opening of 2 inches in length and 0.25 inches in width. The angle used to diverge the shock was 8 degrees. The transition section can be attached to the test section, or the extension through use of screws. The transition section was matched with the test section or the extension by use of screws and locator pins. Figure 27 presents the transition section.

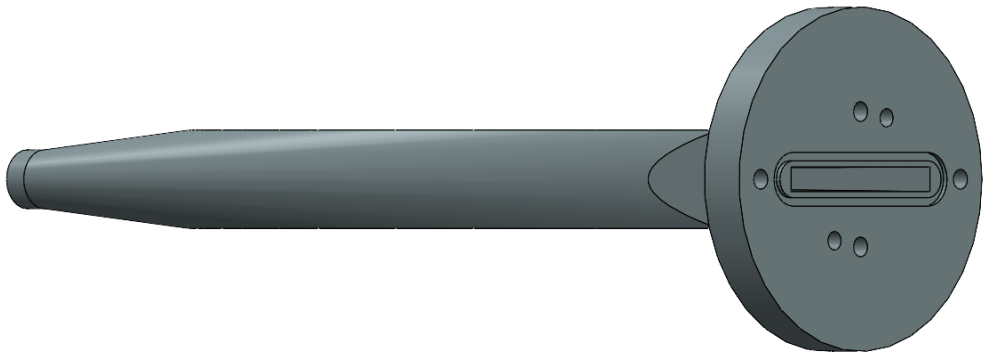

Figure 27. Transition section

The purpose of the extension was to allow more length for the detonation to stabilize. The extension overall was 12 inches in length, machined using stainless steel, and located between the transition piece and test section. The channel inside the extension possessed the same dimensions as the end of the transition and the test section which were 2 inches in length, and 0.25 inches in width. Not all test cases utilized the extension. Figure 28

shows a CAD model of the extension. The extension also features four holes for ion probes. The ion probes are located evenly through the 12 in length on the wide side of the extension. The timing difference, or ‘delta t’ of the ion probs was recorded between the first and fourth ion probs.

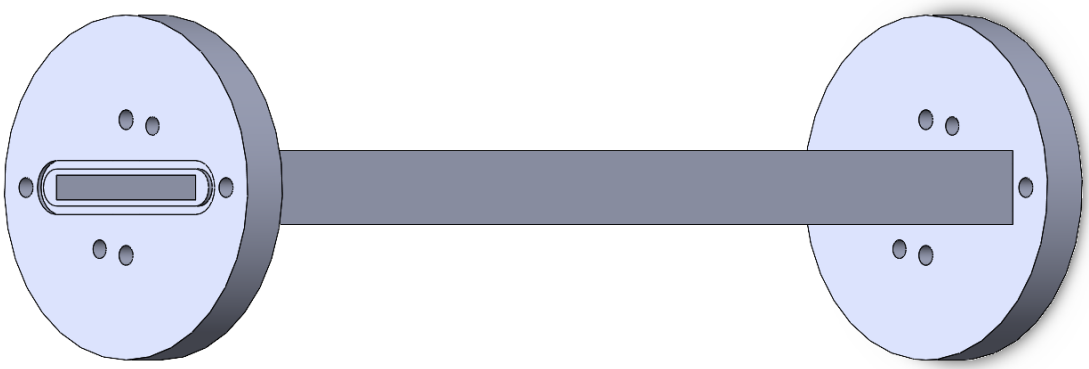

Figure 28. Extension (ion prob location not shown)

The channel had width of 2 inches and a length of 0.25 for an aspect ratio of 8. The channel ratio of was based off of previous 2-D channel work using the NCF [14,15,16]. The length of the detonation test section was 6 inches with a width of 2 inches. The window of the channel was made out of quarter-inch-thick quartz. The window was held in place by room-temperature-vulcanizing (RTV) silicon. The window was 1 in in length and width. The test section was made out of four different parts held together by screws and locator pins. The purpose of using different parts was to allow the

placement of the optical window. The window was held in place by use of RTV. Figure 29 presents the test section design.

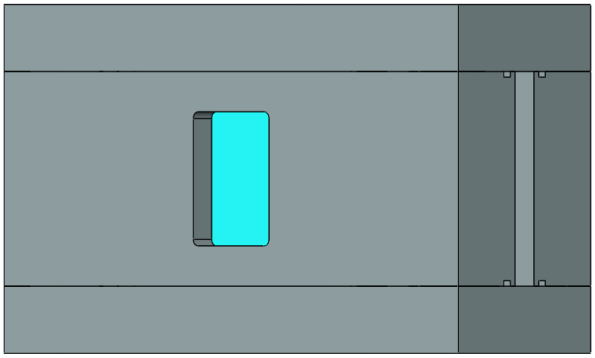

Figure 29. Test section

For the tests that utilized only the transition and test section configuration, ethylene, hydrogen, and air varied throughout the run. It was also diluted with either nitrogen or argon. Dilution of Argon and Nitrogen maintained 20.7% through all cases when compared to air. Overall dilution varied throughout test cases. The comparison of the data was done using percentage of hydrogen fuel used. Table 1 presents the test cases.

Table 1. List of test parameters for 2-D test section without extension.

Test	H_2 [SLPM]	C_2H_4 [SLPM]	O_2 [SLPM]	N_2 [SLPM]	Ar [SLPM]	H2 Fuel Percent	Overall Dilution
1	18	0	9	7	0	100%	21%
2	12	1	9	7	0	92%	24%
3	6	2	9	7	0	75%	29%
4	0	3	9	7	0	0%	37%
5	3	2.5	9	7	0	55%	33%
6	0	3	9	0	7	0%	37%
7	3	2.5	9	0	7	75%	23%
8	6	2	9	0	7	75%	29%
9	12	1	9	0	7	92%	24%
10	18	0	9	0	7	100%	21%

Argon and nitrogen dilution were done for hydrogen, ethylene, and mixed-fuel blends. Argon dilution was only done with ethylene. For these experiments, the ion probs were plugged and not recorded. For the nitrogen dilution, three ion probs (first, second and fourth ion probs) were in place but only the time between the first and fourth were recorded. Table 2 through Table 7 list all test conditions using the extension.

Table 2. Extension test conditions for shadowgraph ethylene-oxygen diluted with argon.

C_2H_4 (Mol)	O_2 (Mol)	Ar (Mol)
1	3	9
1	3	10
1	8	6
1	3	3
1	3	0
1	3	0

Table 3. Extension test conditions for shadowgraph ethylene-oxygen diluted with nitrogen.

C_2H_4 (Mol)	O_2 (Mol)	N_2 (Mol)
1	3	0
2	6	2
2	6	6
2	6	7
2	6	10

Table 4. Extension test conditions for shadowgraph hydrogen-oxygen detonation diluted with nitrogen.

H_2 (Mol)	O_2 (Mol)	N_2 (Mol)
8	4	8
8	4	10
8	4	6
8	4	4
8	4	4
8	4	2
8	4	0
8	4	0

Table 5. Extension test conditions for shadowgraph mixed fuel oxygen detonations diluted with nitrogen.

H_2 (Mol)	C_2H_4 (Mol)	O_2 (Mol)	N_2 (Mol)
0.5	1.5	4.75	4.75
1	1	43.5	3.5
3	1	4.5	4.5

Table 6. Extension test conditions for vertical Schlieren mixed fuel oxygen detonations diluted with nitrogen.

H_2 (Mol)	C_2H_4 (Mol)	O_2 (Mol)	N_2 (Mol)
0	2	6	6
0	2	6	8
0	2	6	0
0.5	1.5	4.75	4.75

Table 7. Extension test conditions for horizontal Schlieren mixed fuel oxygen detonations diluted with nitrogen.

H_2 (Mol)	$C2H_4$ (Mol)	O_2 (Mol)	N_2 (Mol)
0	2	6	8
0	2	6	0
0	2	6	0
0	2	6	8

3.1.2 Optical Setup

Schlieren and shadowgraph were performed using a Cavilux laser for the light source. The laser diameter was controlled by an adjustable iris. The laser light was then shined through a 55-mm focal-length lens to collimate the light. The collimated light then passed through the test region. After passing through the test region, the light traveled to a 150-mm focal-length lens. For the case of shadowgraph, the light was then sent to the lens on the Shimadzu camera. For Schlieren the light was cut with a knife edge (done both vertical and horizontal) and then passed to the lens on the Shimadzu. The images were then recorded using the Shimadzu camera. Figure 30 is the general optical setup. For Shadowgraph the knife edge was not present.

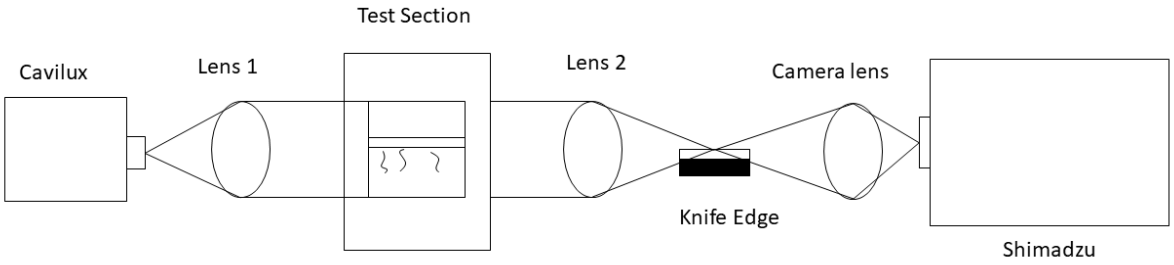

Figure 30. Optical Schlieren Setup.

The Shimadzu camera was used to image the windowed test-section. The camera only captured a portion of the test-window while imaging. To combat this, the camera was calibrated placing a clear ruler in the test section and imaging it before the test series. The test series used various different imaging techniques. Imaging techniques applied were Schlieren, shadowgraph, and chemiluminescence. The size of the images were 250 x 400 pixels^2. The framerate utilized without the extension was 2 MHz. The framerate used with the extension was 5 MHz and 10 MHz. The exposure time was 200 ns when not employing the extension and set to the minimum value when employing the extension. Figure 31 is an example of the shadowgraph at these settings.

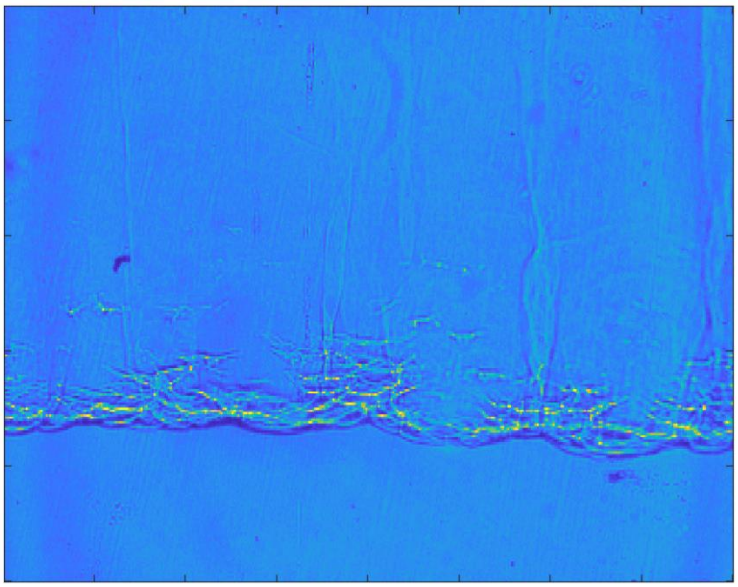

Figure 31. Shadowgraph of a detonation in 2-D section.

3.1.3 Calculation of Detonation Speed

A MatLab computer code was created to calculate the speed of the detonation wave inside the 2-D channel from the shadowgraph imagery. Frames possessing the detonation wave front were read into the code. The detonation wave front was identified and isolated in each frame. The speed of the detonation was calculated from the change in the location of the wave front.

Background subtraction was performed by averaging the first four images in an image set and considering the average the background. The background was then subtracted from each image in the detonation set. Figure 32 is an example of background subtraction. Isolation of the wave front first consisted of using the Sobel operators. Convolution was performed to output the edges produced from the Sobel operators.

Equation 3.1 and 3.2 shows the Sobel operators convolved with the image f_x. To produce the new images with the edges the magnitude squared of both outputs of the Sobel operators is taken. This is shown in Equation 3.3 [4].

$$g_x = \begin{matrix} -1 & 0 & 1 \\ -2 & 0 & 2 \\ -1 & 0 & 1 \end{matrix} * f_x \quad \textbf{(3.1)}$$

$$g_y = \begin{matrix} -1 & -2 & -1 \\ 0 & 0 & 0 \\ 1 & 2 & 1 \end{matrix} * f_x \quad \textbf{(3.2)}$$

$$g = \sqrt{(g_x)^2 + (g_y)^2} \quad \textbf{(3.3)}$$

A binary image of the lines was produced by thresholding the Sobel image by 0.1 of the max counts intensity. Figure 33 is an example of the Sobel threshold. A median filter of either 3 x 3 pixels^2, 5 x 5 pixels^2, or 10 x 10 pixels^2 were applied to create a so-called 'blob' of the wave front. To further isolate the detonation wave, wave blob tracking was applied which is also known as connected components extraction. This method works by having an array A containing one or more set of connected components. The array forms X_0 which contain the values of 0's for background components and 1's for foreground components. The objective is to find all the connected components of 1's starting with X_0. The iterative equation to find these regions are presented in Equation 3.4 [4].

$$X_k = (X_{k-1} \oplus B) \cap A \qquad k = 1,2,3, \ldots. \quad \textbf{(3.4)}$$

Where B is a structuring element and X_k is all inputs of the image [4]. Figure 34 is an example of the median filter. Figure 35 is an example of detonation isolation. A blob with an area above 500 pixels was considered the detonation wave and only blob kept in image.

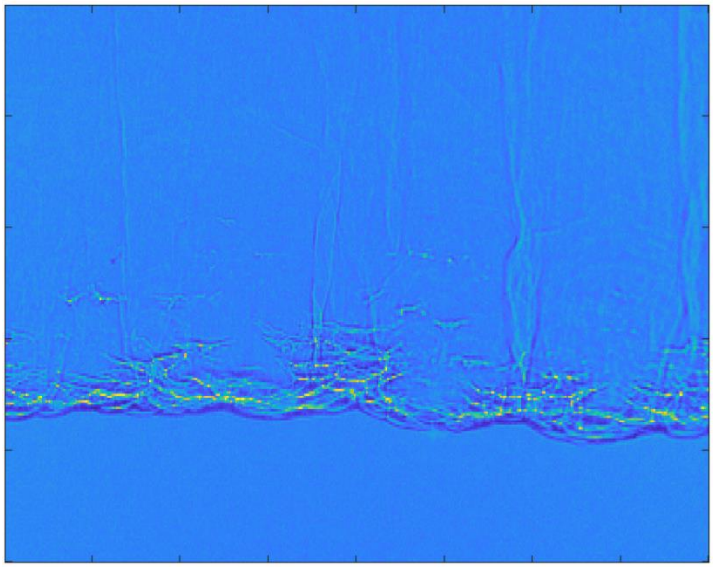

Figure 32. Background subtraction performed on same image as Figure 31.

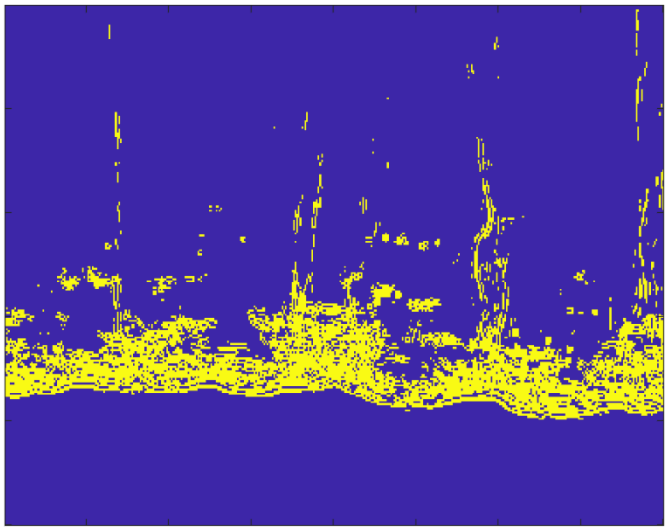

Figure 33. Sobel Threshold applied on Figure 32.

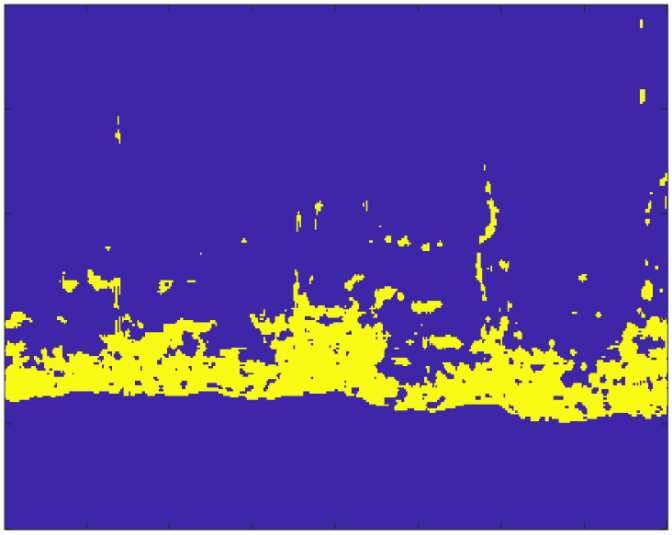

Figure 34. 3 x 3 Median filter applied to Figure 33.

Figure 35. Noise reduction of only detonation present of Figure 34.

To find the location of wave front, the code iterated through the locations in the x-direction and then the y-direction. The last value were a non-zero values was presented was recorded as the location of the detonation in the column. The change in pixels of the location detonation wave was used to determine the velocity of the wave. The change in pixels between the detonation wave front was multiplied by the resolution and then divided by the frame rate. Equation 3.5 is how velocity is calculated with Δy being the change in pixels in the y-direction.

$$velocity = \Delta y * fps/resolution \quad \textbf{(3.5)}$$

To better track the detonation wave speed across the wavefront, the detonation was divided into five different regions. The regions were split into five identically sized vertical strips. The mean value of the speed was recorded based on the region. From each region, the mean value of all five regions became the average speed of the detonation wave. All regions and detonation average value were plotted for comparison. Figure 36 is an example of detonation wave speed in the 2-D channel.

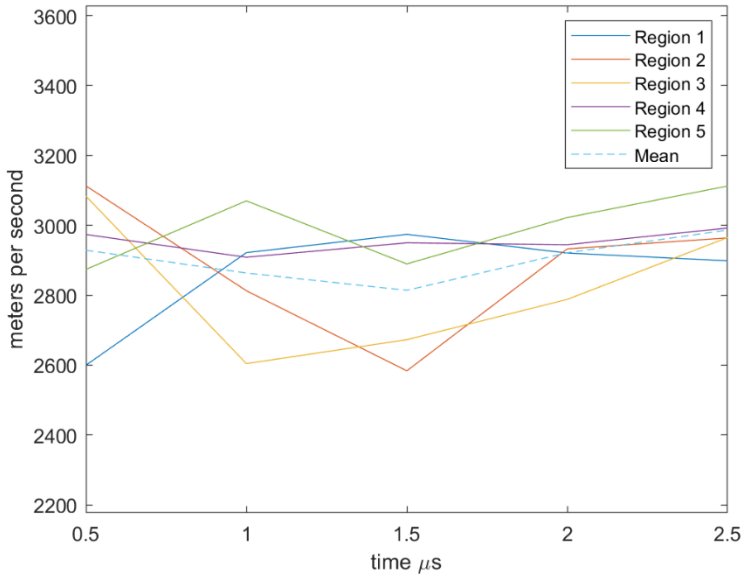

Figure 36. Example of detonation speed.

3.1.4 Soot Foil Formation and Cell Size

Detection of the triple point location followed the velocity code up until the actual velocity was calculated. The triple points were located by locating the local minima in the detonation wave front. Local minima of the wave front are found with a prominence of two. These local minima generally correlate to a triple point location. The median filter used were either 5 x 5 pixels^2 or 10 x 10 pixels^2. The code only works when the frame rate is 5-10 MHz in fps because of the Nyquist sampling limit criterion. Figure 37 is an example of a soot foil produced from a data set taken at 10 MHz. The width of the cell was calculated by locating the diamond shape pattern and finding the location difference of the horizontal tips. This method was done visually only.

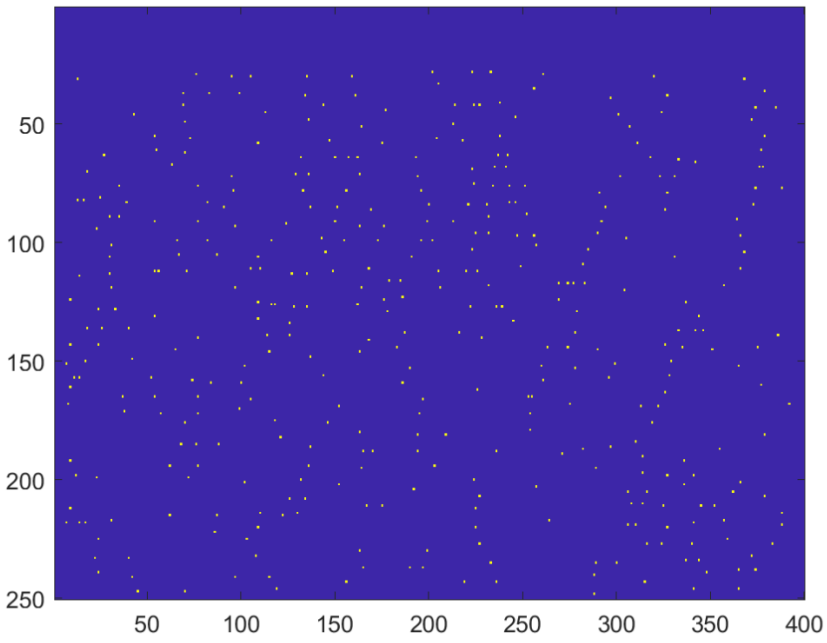

Figure 37. Example of soot foil taken at 10 MHz with a 5-x-5 pixels median filter.

3.1.5 Detonation Wave Thickness

The detonation wave thickness was determined by following the same method as the velocity code. The only difference was that a median filter of 5 x 5 pixels^2, or 10 x 10 pixels^2 was used. The code works by using the same algorithm to determine the location of the wave front and finding the last non-zero number. The code also uses another algorithm to locate the first occurrence of a non-zero number in the y-direction. The thickness is determined by the difference in the location of the end and beginning of the detonation wave front. Equation 3.6 is how the detonation thickness is calculated per frame.

$$\det \text{thickness} = \left(\frac{1}{N} \sum_{i=1}^{N} \left(\sum_{j=1}^{249} \delta\big(f(i,j+1)\big)\delta(f(x,j)-1)j - \sum_{j=1}^{249} \delta(f(i,j)-1)\delta(f(i,j-1))j \right) \right) * resolution \quad \textbf{(3.6)}$$

Where f(i,j) is the pixel value of the image in that index. N is the number of values in the x-direction of the binary image. This thickness is then averaged across the wave. It is furthered averaged across the data set of the wave. This method can only be applied to shadowgraph.

3.2 Study of Detonation Travel through a Rectangular Tubed Curved Channel

The purpose of this section of study is to simplify the study of how detonations travel around the annulus of a combustor. For this study, rectangular tubed curved channel resembling a horseshoe shape is utilized. Work specifically using the Horseshoe test section shape has been researched previously [21]. The remainder of Section 3.2 consists of how the study was conducted.

3.2.1 Horseshoe Rig Set-up

To study how detonations behave while rounding a curve, curved tubes of rectangular cross section are used. The rectangular round tubes are constructed using

carbon steel. There is a run-up straight section before the curved portion, giving the shape of a horseshoe. To contain the detonation, the steel is placed between two sheets of half-inch-thick polycarbonate. The polycarbonate is clear, allowing optical access to the detonation. Figure 38 is a schematic of the horseshoe detonation channel. A pre-detonator is used to create the detonation wave. The DDT obstacles are placed to ensure the formation of the detonation wave. The length of the run-up section is ten times the channel width, allowing time for the detonation to form. The pre-detonator and the exhaust were both open to the atmosphere.

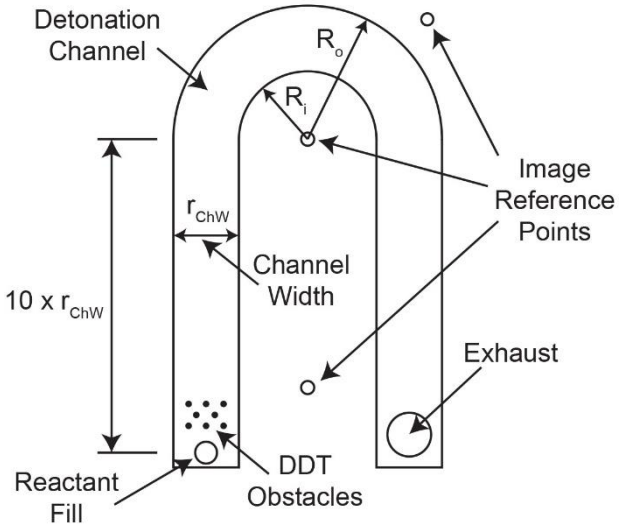

Figure 38. Schematic of Horseshoe Test Section [21].

The R_i and Ro were varied. For the cases using ethylene the Ri/Ro ratio were held constant at 4/5. For the cases using hydrogen, Ri and Ro varied as well as the ratio. Table

8 shows the test section geometry for the ethylene cases. Table 9 shows the test section geometry for all the hydrogen cases.

Table 8. Ethylene Test section Geometry

Test-Section	Inner Radius of Curve, R_i [in]	Outer Radius of Curve, R_o [in]	Detonation Channel Width, [in]	R_i/R_o
C1	6	7.5	1.5	0.800
C2	8	10	2	0.800
C3	9.6	12	2.4	0.800

Table 9. Hydrogen Test Section Geometry

Test-Section	Inner Radius of Curve, R_i [in]	Outer Radius of Curve, R_o [in]	Detonation Channel Width	R_i/R_o
C1	5.02	6	0.98	0.837
C2	4.65	6	1.35	0.775
C3	4.25	6	1.75	0.708
C4	7.53	9	1.75	0.837
C5	6.98	9	2.02	0.776
C6	6.37	9	2.02	0.708
C7	10.04	12	1.96	0.837
C8	9.3	12	2.7	0.775
C9	8.49	12	3.51	0.708

Equivalence ratio (Φ) varied between 0.7-1.8 for ethylene-air. The cell sizes were calculated from the data provided by the Cal Tech database using Knystautas [23] data set. Interpolation of the cell sizes were used to calculate the equivalence ratios not found in the Knystatus [23] data set. Allicat flow controllers were used to control the overall flow rate and equivalence ratio of the gases flowing into the horseshoe detonation channel. The error rate of the flow controllers was ±0.05 of the equivalence ratio. Table

10 presents the cell sizes of the equivalence ratios for the ethylene experiments with their error provided.

Table 10. List of tested Equivalence ratios with their calculated cell size.

Equivalence Ratio	Cell Size (in)	±Error (in)
0.7	2.41	1.37
0.8	2.20	0.29
0.9	1.43	0.48
1.0	1.02	0.21
1.1	0.85	0.04
1.2	0.93	0.05
1.3	1.04	0.07
1.4	1.18	0.07
1.5	1.30	0.06
1.6	1.48	0.22
1.7	1.92	0.23
1.8	2.28	0.12

For the hydrogen data set, the equivalence ratio varied from 0.5-2.0. Cell widths were calculated from the data provided by the Cal Tech data base. The data sets used to calculate these widths were Tiezen [24] and Circcarelli [25]. Linear interpolation through the data set were used to calculate the cell sizes. Error was calculated based on the Alicat flow controllers possessed an ±0.05 equivalence ratio error. Error was calculated by subtracting the largest cell size created by the ± 0.05 equivalence ratio from the actual and then taking the absolute value. Equation 3.7 presents how this was done.

$$Error = \left|Cellsize_{\Phi} - \max\left(Cellsize_{\pm 0.05\Phi}\right)\right| \quad \textbf{(3.7)}$$

Table 11 presents the cell widths with their errors.

Table 11. List of tested Equivalence ratios with their calculated cell size.

Equivalence Ratio	Cell Size (in)	±Error (in)
0.5	4.14	4.98
0.6	1.63	1.22
0.7	1.00	0.31
0.8	0.43	0.26
0.9	0.38	0.02
1.0	0.33	0.02
1.1	0.33	0.00
1.2	0.33	0.00
1.3	0.33	0.00
1.4	0.34	0.00
1.5	0.34	0.00
1.6	0.36	0.04
1.7	0.43	0.04
1.8	0.51	0.04
1.9	0.59	0.04
2.0	0.67	0.04

3.2.2 Optical Set-up

Ethylene data of how the detonation propagated around the radius were obtained via video imaging of the combustion chemiluminescence. The camera used was the Phantom 711. Figure 39 shows how the camera was setup in relation to the test-section. The camera was paired with the lens of either 50- or 35-mm. The aperture of these lenses was either f/1.8 or f/2.2. No wavelength filters were used. The Phantom camera recorded the chemiluminescence data in a 16-bit monochrome video. The video had a resolution of 256 x 352 pixels^2. The exposure time was 0.5 μs. After the videos were recorded gamma and gain corrections were performed in the Phantom camera video application to correct image brightness.

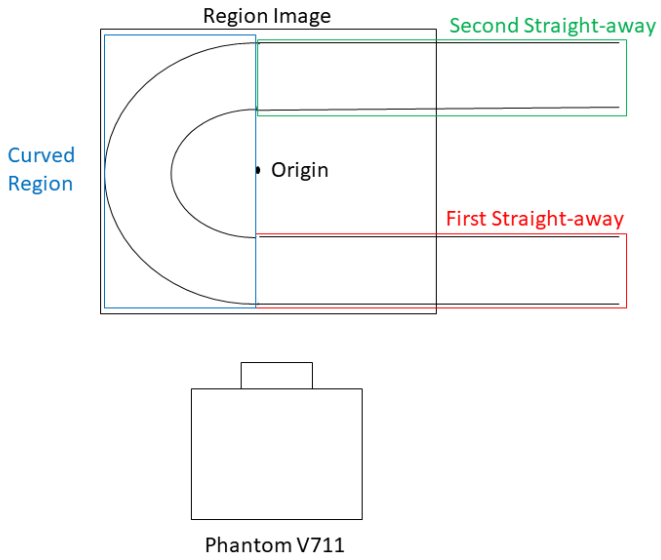

Figure 39. Setup of Phantom v711 in relation to test-section.

Hydrogen data was also obtained using chemiluminescence imaging using the same Phantom 711. The Phantom camera used the 35-mm lens with no wavelength filter. The aperture for the lenses were either f/1.4 or f/2.2. The resolution for the recording varied. The resolution of the video was 688 x 544, 608 x 592, or 592 x 512 pixels^2. The exposure time was 1 μs. After videos were recorded, gamma and gain corrections were made to image brightness using the phantom software.

3.2.3 Calculation of Detonation Speed

Analysis of the images were done visually and computationally. Visual comparison of the leading and lagging wave helped identify the wave classification. To calculate the speed of the inner and outer wave, a Matlab computer code was created.

The code first isolated the detonation wave front for each image in the series. A threshold between 3000-7000 counts intensity was applied to create a binary image of the detonation wave front. A ‘blobs’ method (Equation 3.4) of tracking was applied to detect the binary detonation wave front. To discriminate the detonation wave front from noise, the area of the blob must have been greater than 100 pixels or it was rejected as noise. The location of the detonation wave front in the image is then recorded. All images possessing the detonation wave front had their location recorded. Figure 40 is an example of how detonation wave front is isolated.

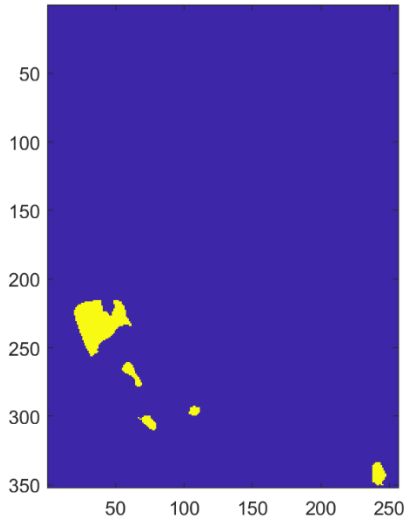

Figure 40. Example of isolation of the detonation wave front.

From the stored locations of the detonation wave front, the Taubin fit was applied to locate the origin of the horseshoe. The code used for the Taubin fit was coded by Chernov [26]. The Taubin fit also provided the radius of the horseshoe in pixels. The

radius provided was from the center of the channel width. The resolution of the image was calculated from the radius provided in pixels. Ro and Ri were calculated into pixels from known values. From these calculations, an outer radius polar mesh and an inner radius polar mesh were created. Each bin of the mesh correlated to one degree. Both polar mesh widths consisted of 1/3 of the channel. Figure 41 is an example of the polar mesh.

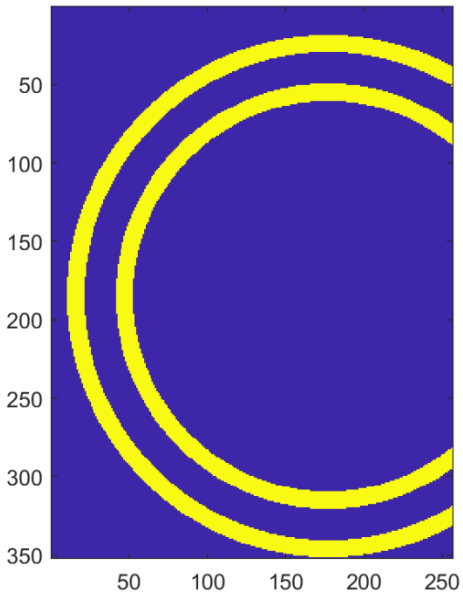

Figure 41. Example of the polar mesh applied

Before data can be placed into the bins of the mesh, a window was applied. The purpose of the window was to assist with noise suppression. The location of where the window was applied was based of the location of where the detonation wave front was

located. The window size ranged from 50 pixels in width to size of the image, depending on level of noise suppression was needed.

An image was created using all the polar meshes from each frame. The bins of the mesh were created by the polar coordinates of the mesh. The cartesian coordinates were first shifted so that the origin was at (0,0) for the shifted graph (Equations 3.7, 3.8). From here, all points were converted to polar coordinates by Equation 3.9.

$$v = x - origin_x \tag{3.7}$$

$$d = origin_y - y \tag{3.8}$$

$$\theta = \tan^{-1}\left(\frac{d}{v}\right) \tag{3.9}$$

Where v is the new shifted x-component, d is the shifted y-component and θ is the degrees in the polar coordinates, $origin_x$ is the x-axis location of the origin, and $origin_y$ is the y-axis location of the origin. The radius of the mesh were known values from the test-section dimensions. Each column of the image corresponded to the specific values of the mesh. Before placing the data into the bins, a second threshold on the main image was applied. For the ethylene data this threshold was the same as the threshold used to detect detonation wave front. For hydrogen, this threshold was about 1000 counts intensity above the threshold used to detect the wave front. All columns were normalized using the max value of the mesh in the given windowed frame. A binary image was created by

thresholding the normalized bins by the values of 0.04-0.06. Figure 42 is the original polar mesh image and Figure 43 is the binary image. The y-axis of the image was the degrees of the mesh, and the x-axis was the time of the frame.

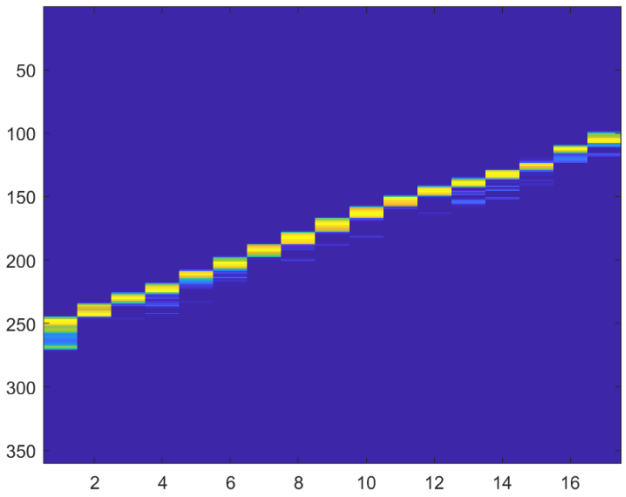

Figure 42. Example of polar mesh image. X-axis is frame number and y-axis is degrees (θ).

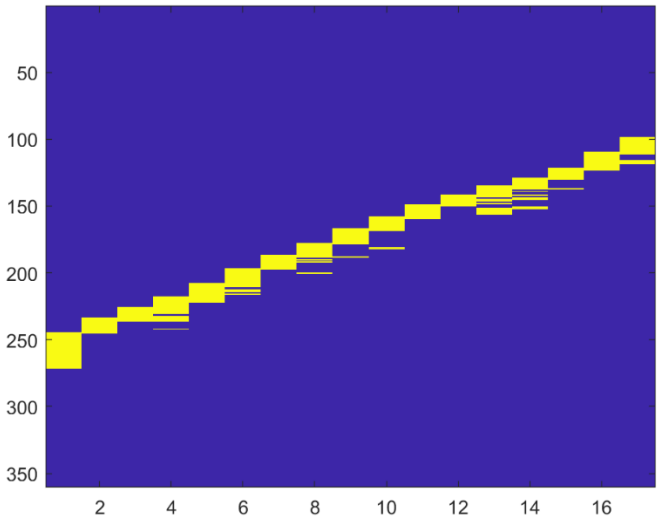

Figure 43. Example of binary polar mesh image. X-axis is frame number and y-axis is degrees (θ).

The speed of the inner and outer waves was calculated using the binary image. To determine where the wave is using the binary image, the last bin with a non-zero number was declared the location of the wave in the bin. The change in degrees between frames and the resolution was used to calculate the arclength the wave traveled. From there, the change in arc length was multiplied by the frame rate of the camera to provide the detonation speed of both the inner and outer wave. Equation 3.10 is how speed across the arc is calculated.

$$D = \left(\frac{\Delta\theta}{360}\right) * 2\pi r * fps \tag{3.10}$$

With r being either the known values of the inner or outer radius. The speed of the waves in the arc were then normalized by the speed coming from first straight portion (D_{str}) of the test section. The speeds in both straight portions were calculated by looking for the last one occurring in the binary image and claiming the one as the location of the wave. Figure 44 is an example of what the code outputs.

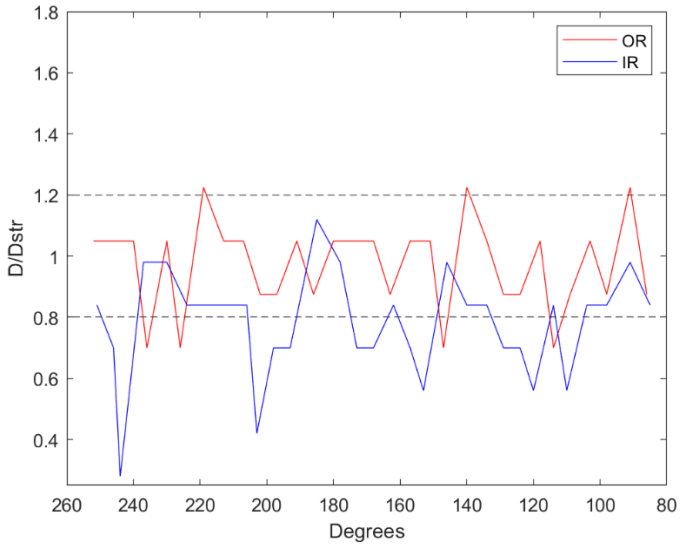

Figure 44. Example of detonation speed.

IV. Analysis and Results

4.1 Analysis of 2-D Predet Channels

Section 4.1 contains all data concerning the two-dimensional pre-mixed pre-detonation channels. The purpose of this research was to study how detonations behave in a two-dimensional plane. The first phase of testing consisted of only the test-section

connected to a shock-tube. The second phase of testing had the test-section with an extension connected to a shock-tube.

4.1.1 Results from the Test-Section Without an Extension

For the 2-D channels, the fuel was a mixture of hydrogen and ethylene. The amount of oxidizer remained a constant at nine moles. The amount of diluent (nitrogen and argon) remained a constant at seven moles. The amount of hydrogen and ethylene in moles were tailored to maintain a stoichiometric equivalence with oxygen at nine moles. Test cases varied based off of percentage of hydrogen as fuel. The approximate hydrogen proportions for these cases were 100%, 92%, 75%, 55% and 0%. The exact molar volumes are listed in Section 3.

All imagery data taken for this experiment were collected by the Shimadzu camera using the shadowgraph technique. Shadowgraph behaves like Schlieren but instead is the second derivative in the images (while Schlieren is the first). The camera frame rate was set to 2 MHz. The spatial resolution for all the images was found to be 23 pixels/mm. Image resolution was 250x400 pixels^2. The images were broken up into five regions to better track the wave velocity throughout the image.

Only a portion of the entire test region (50.76 x 50.76 mm^2) imaged by the Shimadzu camera. Keeping the resolution constant, the entire test region would require 1168 x 1168 pixels, but the camera is limited to 250 x 400 pixels were captured. The regions are orientated so that region 1 is the area closest to the center of the test region, while region 5 is closest to end of the test region. Each region is 50x400 pixels. This translates into the region being 2.17 x 17.39 mm^2.

Detonations with the nitrogen dilution did not have a straight detonation wave-front. When compared to argon dilutions, the nitrogen wave front was not as uniformed across. This can be explained by nitrogen dilution causing an increase in the cells in the detonation cell size compared to the argon cases. Figure 45 is an example of a detonation diluted with nitrogen. The percentage of hydrogen in the fuel blend was 55%. Figure 46 is an example of a detonation diluted with argon with the same percentage of hydrogen in the fuel blend.

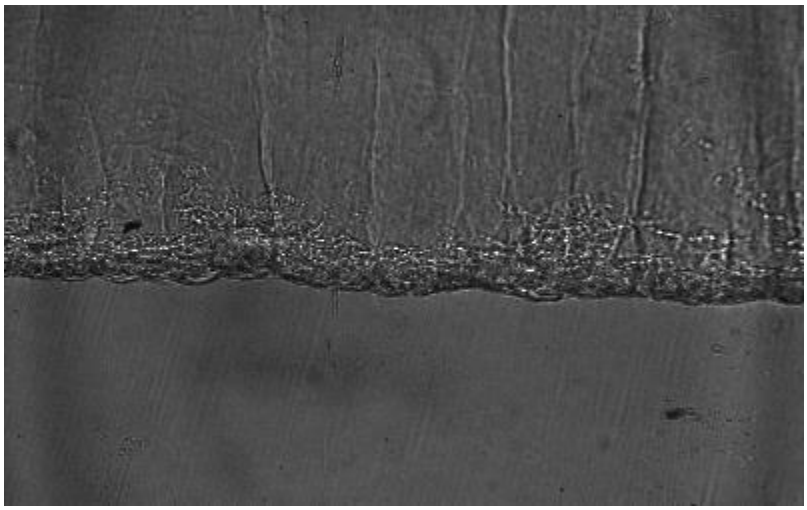

Figure 45. Shadowgraph of detonation with nitrogen-dilution with 55% hydrogen fuel.

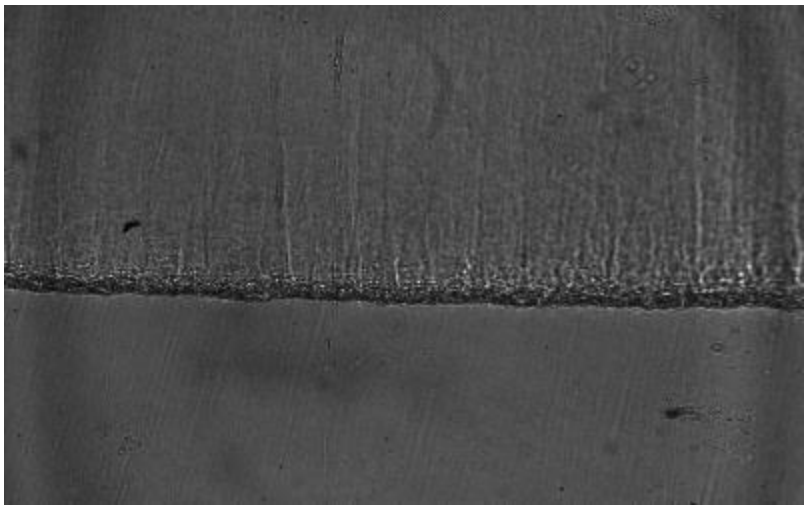

Figure 46. Shadowgraph of detonation with argon-dilution with 55% hydrogen fuel.

For this section wave stability was studied based on the velocity calculated. The data from the detonations diluted with nitrogen produced the more unstable waves when compared to the argon dilution. Figure 47 presents the velocity data for 55% hydrogen fuel diluted with nitrogen. Figure 48 presents the velocity data for 55% hydrogen fuel diluted with argon. These two figures are examples of what is generally found in the rest of the data. Runs diluted with nitrogen had more instability in their velocity when compared to argon. Runs diluted with Argon velocity had better grouping, with their mean velocity data almost forming straight line.

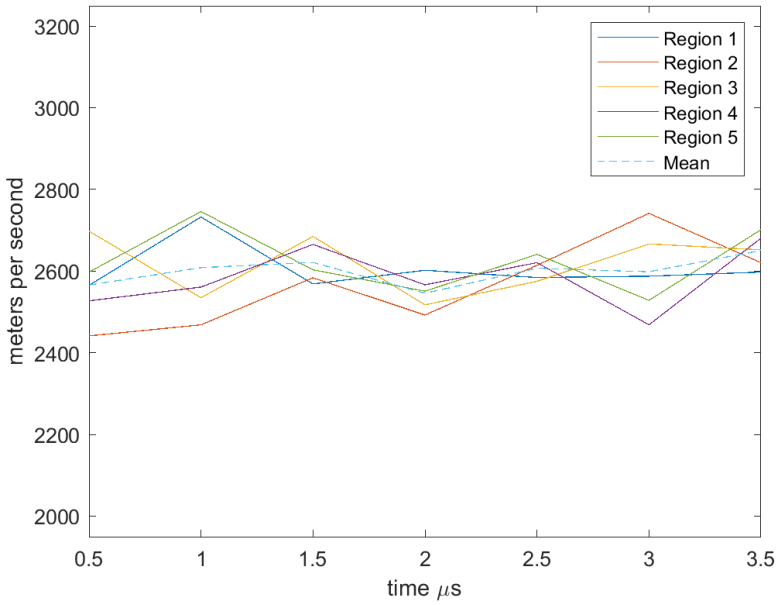

Figure 47. Velocity of the detonation wave in all five regions. Data is from 55% hydrogen fuel with the nitrogen diluent.

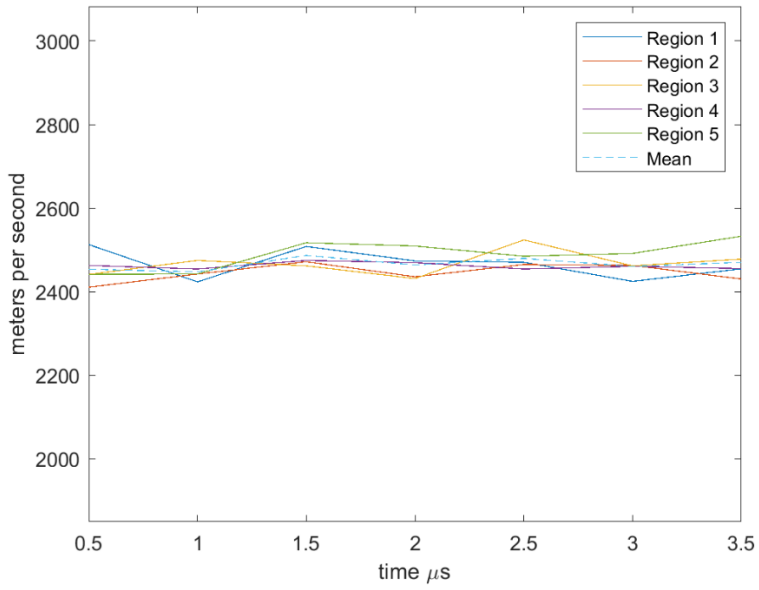

Figure 48. Velocity of the detonation wave in all five regions. Data is from 55% Hydrogen fuel with the argon diluent.

The mean velocity for all regions and all data sets were calculated. Table 12 contains all mean velocity data for the nitrogen diluted runs with varying ethylene and hydrogen. Higher percentages of hydrogen fuel resulted in faster the detonation speeds. This correlates well to pure hydrogen-oxygen detonations having a higher CJ point compared to ethylene-oxygen detonations. Table 13 contains the standard deviation of the data presented in Table 12. There appears to be a trend of increased speed variance throughout the wave with proportion of hydrogen fuel present.

Table 12 contains the mean velocity data for nitrogen cases. Pure (100%) H_2 fuel has the highest mean velocities in the table. The trend in velocity is linear, as in the less H2 fuel presented, the slower the velocity. This can be attributed to hydrogen in general having a faster CJ speed then ethylene.

Table 12 contains all mean velocity data for the nitrogen diluted runs with varying ethylene and hydrogen. Higher percentages of hydrogen fuel resulted in faster the detonation speeds. This correlates well to pure hydrogen-oxygen detonations having a higher CJ point compared to ethylene-oxygen detonations. Table 13 contains the standard deviation of the data presented in Table 12. There appears to be a trend of increased speed variance throughout the wave with proportion of hydrogen fuel present.

Table 12. Region's mean velocity data for the diluent nitrogen.

%H2 Fuel	Diluent (%)	Region 1 mean Velocity (m/s)	Region 2 mean velocity (m/s)	Region 3 mean velocity (m/s)	Region 4 mean velocity (m/s)	Region 5 mean velocity (m/s)
100	21	2766.4	2750.3	2712.7	2799.5	2841.2
92	24	2707.9	2725.2	2726.2	2748.8	2739.4
75	29	2619.8	2540.7	2576.9	2546.9	2578.1
55	33	2579.7	2533.1	2583.7	2547	2591.5
0	37	2503.4	2478	2516.6	2512.3	2584.2

Table 13. Region's standard deviation (STD) velocity data for the diluent Nitrogen

%H2 Fuel	Diluent (%)	Region 1 STD Velocity (m/s)	Region 2 STD velocity (m/s)	Region 3 STD velocity (m/s)	Region 4 STD velocity (m/s)	Region 5 STD velocity (m/s)
100	21	248.5288	276.5386	249.4715	264.9536	274.9399
92	24	215.2935	164.0421	181.1215	177.3488	192.036
75	29	126.9076	178.7075	151.2885	150.1947	110.065
55	33	91.6241	120.5197	105.8132	84.1502	87.4953
0	37	105.0028	118.6555	76.8741	78.421	117.1771

Table 14 contains the mean velocity data of the detonations diluted with argon. The same trend occurred with argon dilution as with the nitrogen dilution, velocity was higher with more hydrogen present in the fuel blend. Table 15 is the standard deviation of the argon velocity data. The argon standard deviation when compared to the nitrogen is much smaller. This decrease in the cell size explains why the velocity data grouping was much smaller for the argon cases: smaller cell sizers support increased stability.

Table 14. Region's mean velocity data for the diluent Argon.

%H2 Fuel	Diluent (%)	Region 1 mean Velocity (m/s)	Region 2 mean velocity (m/s)	Region 3 mean velocity (m/s)	Region 4 mean velocity (m/s)	Region 5 mean velocity (m/s)
100	21	2667	2669.9	2688	2695.3	2721.9
92	24	2608.5	2607	2614.3	2632.3	2636.4
75	29	2502.6	2498.1	2495.5	2501.7	2562.7
55	33	2467	2445.7	2467.7	2467.7	2488.6
0	37	2444.3	2416	2439	2426.6	2471.6

Table 15. Region's STD velocity data for the diluent argon.

%H2 Fuel	Diluent (%)	Region 1 STD Velocity (m/s	Region 2 STD velocity (m/s)	Region 3 STD velocity (m/s)	Region 4 STD velocity (m/s)	Region 4 STD velocity (m/s)
100	21	65.9532	37.0933	43.3876	64.9563	83.9307
92	24	42.081	35.5323	56.5441	36.1197	58.644
75	29	55.65	39.4647	44.5936	36.1803	42.0775
55	33	35.7813	22.036	29.9897	8.0471	35.5448
0	37	59.3756	32.0773	67.826.5	28.1202	35.5523

After all cases had been examined, it was determined all cases were significantly above the CJ point. This fact infers all data points were unstable overdriven detonation waves. This instability was believed to be caused by insufficient distance for the detonation to stabilize before reaching the windows. A 12 in extension was built to counteract this problem.

4.1.2 Results with Extension

The first experiment with the extension verified that the extension created more wave stability. Ethylene-oxygen detonation with the diluent of argon was chosen to do this. It was run at stoichiometric with the equation being $C_2H_4 + 3O_2 + xAr$ with x

denoting for number of moles of argon. This variable differed for the tests. The tests used the Shimazu camera operating at 5 MHz. Resolution was found to be 33.75 pixel/mm. Similar to the setup with no extension, the whole test region is not imaged at once. Only about half the test region can be imaged.

The detonation wave front was examined for all argon dilution cases. It was found that at least one mole of argon presented would produce a uniform detonation wave front. Figure 49 is an example of the dilution cause. The data was taken using six mols of argon. For the neat (no dilution) case, the detonation was found to exhibit a curvature. Figure 50 is an example of the detonation curve occurring when no dilution is present. The edge of the test section is on the left-hand side of the image.

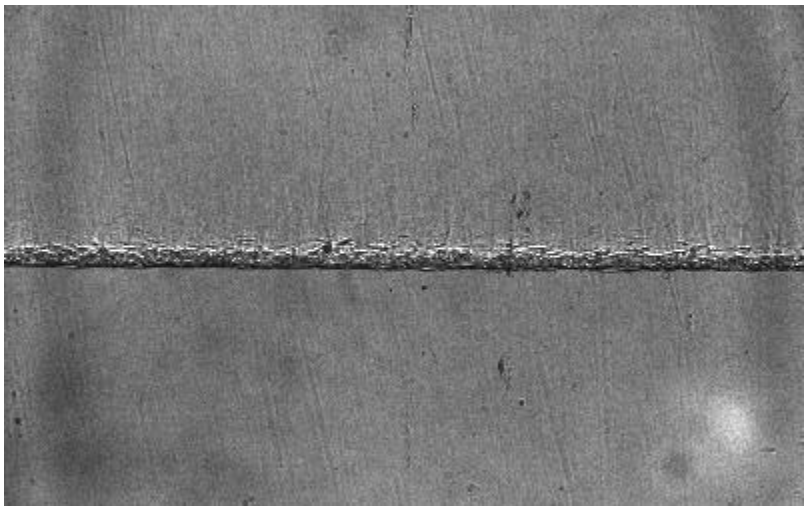

Figure 49. Ethylene-oxygen detonation with six moles of argon dilution.

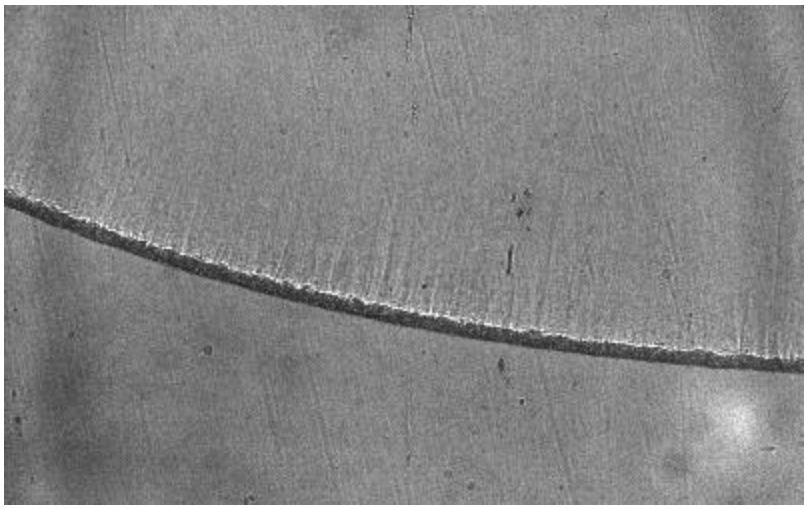

Figure 50. Ethylene-oxygen dilution with no argon dilution.

Detonation speeds of ethylene diluted with argon were near the CJ speeds. Table 16 presents the velocity data of ethylene diluted with argon. Ethylene and oxygen moles were held constant at one mole of ethylene and three moles of oxygen. Data was produced by running the velocity code on the shadowgraph data. The velocity follows the trend of the addition of more diluent, the slower the detonation propagates. Table 17 is the standard deviation of the velocity data for ethylene-oxygen detonations diluted with argon. The standard deviations got smaller as less diluent was applied. The only cases where this trend was not observed were the neat detonations. This was believed to be caused by the detonation curve and the median filter not accounting for said curve.

Table 16. Extension mean velocity data for ethylene-oxygen detonation diluted with argon.

Diluent (mols)	Trial	Diluent (%)	Region1 mean (m/s)	Region 2 mean (m/s)	Region 3 mean (m/s)	Region4 mean (m/s)	Region 5 mean (m/s)
9	1	69.2	1757.2	1757.6	1757.5	1761.9	1768.1
10	1	71.4	1732	1734.5	1736	1742.6	1744.9
6	1	60	1826.9	1827	1829.4	1827.8	1835.4
3	1	42.9	1951.2	1954.9	1957.7	1951.3	1959.1
0	1	0	2396.8	2400.2	2395.1	2404.6	2384.5
0	2	0	2470.6	2451.4	2439.3	2426.1	2402

Table 17. Extension standard deviation of the velocity for ethylene-oxygen detonation diluted with argon.

Diluent (mols)	Trial	Diluent (%)	Region1 std (m/s)	Region 2 std (m/s)	Region 3 std (m/s)	Region4 std (m/s)	Region 5 std (m/s)
9	1	69.2	68.259	61.096	56.483	61.747	54.439
10	1	71.4	72.772	81.746	56.859	65.888	57.281
6	1	60	32.422	46.033	25.183	38.190	43.673
3	1	42.9	36.217	34.552	42.458	43.631	55.797
0	1	0	48.481	62.747	58.199	34.133	67.446
0	2	0	52.230	105.10	64.155	68.484	66.150

Dilution with nitrogen was then preformed using the narrow channels. For the nitrogen cases, the fuel varied between hydrogen and ethylene. Mixed fuel of hydrogen and ethylene diluted with nitrogen was also ran. The ion probs were placed in the first and fourth holes of the extension. The time between the two points were recorded and marked as the speed in the extension.

Detonation speeds for ethylene diluted with nitrogen speeds were near the CJ point. The speeds were also around the velocity found in the extension. Table 18 presents the velocity data of the ethylene-oxygen detonations diluted with nitrogen. All test had two moles of ethylene per six moles oxygen. The data was taken using shadowgraph. In the table, the speeds calculated from the video are a little higher than those calculated

from the ion probs, but within the standard deviation of velocity. Increased dilution reduced the detonation speed, this trend agrees with the common knowledge of dilution reducing the CJ velocity of a detonation. Table 19 presents the ethylene-oxygen diluted with nitrogen cases. The standard deviation of the wave velocity in general got smaller as less diluent was added. When compared mole for mole of the diluents argon and nitrogen, nitrogen produced more deviations in the velocity.

Table 18. Velocity of the ethylene-oxygen detonations diluted with nitrogen.

Mols Dilution	Diluent (%)	Region 1 (m/s)	Region 2 (m/s)	Region 3 (m/s)	Region 4 (m/s)	Region 5 (m/s)	Extension (m/s)
0	0	2335.3	2341.3	2341.3	2340.3	2346.4	2336
2	20	2178.9	2201.9	2195.2	2196.3	2209.3	2185
6	42.9	2056.6	2061	2077.3	2056.7	2049.3	2025
7	46.7	1978.2	2004.6	2036.2	1995.7	2023.4	1982

Table 19. Standard deviation of the ethylene-oxygen diluted with nitrogen velocities.

Mols Dilution	Diluent (%)	Region 1 (m/s)	Region 2 (m/s)	Region 3 (m/s)	Region 4 (m/s)	Region 5 (m/s)
0	0	167.3691	76.3889	81.7148	68.5204	65.5367
2	20	132.7261	115.4586	97.5337	63.8946	78.768
6	42.9	135.5165	177.715	82.3322	112.8779	83.4117
7	46.7	171.4683	142.6542	137.9028	119.4545	114.8468

Hydrogen-oxygen detonations diluted with nitrogen had the same trends as the ethylene. All tests had eight moles of hydrogen and four moles of oxygen. Velocity of the hydrogen-oxygen detonations decreased as dilution increased. Table 20 shows velocity data of the hydrogen-oxygen detonations. The data was taken using shadowgraph. The velocities of the hydrogen-oxygen detonations were higher than the ethylene. This is to be expected since hydrogen-oxygen has higher CJ points when compared to the ethylene-

oxygen data points. All speeds in all five regions were around the speeds calculated in the extension. The standard deviations decreased as the diluent decreased as well. Table 21 presents the data of the standard deviation of the velocity in the five different regions.

Table 20. Velocity of the hydrogen-oxygen detonations diluted with nitrogen.

Mols Dilution	Dilution (%)	Region 1 (m/s)	Region 2 (m/s)	Region 3 (m/s)	Region 4 (m/s)	Region 5 (m/s)	Extension (m/s)
8	40	2119.9	2132.3	2130.4	2137.4	2147.1	2170
10	45.5	2039.9	2089.3	2066	2034.9	2123.7	2044
6	33.3	2253.2	226.9	2198	2223.6	2218.9	2233
4	25	2315	2337.9	2307.4	2317.1	2315.9	2313
4	25	2282.7	2323.9	2311	2324.4	2328.3	2348
2	14.3	2500.5	2496.5	2500.9	2491.5	2493	2476
0	0	2707.5	2712.2	2716.8	2716.4	2714	2663
0	0	2705.7	2717.2	2714.1	2708.6	2739.7	2648

Table 21. Standard deviation of velocity from the hydrogen-oxygen detonation diluted with nitrogen.

Mols Dilution	Dilution (%)	Region 1 (m/s)	Region 2 (m/s)	Region 3 (m/s)	Region 4 (m/s)	Region 5 (m/s)
8	40	125.31	70.930	128.11	159.06	69.908
10	45.5	244.33	150.26	68.577	115.00	144.10
6	33.3	96.356	99.335	118.30	86.266	80.330
4	25	101.85	59.315	100.15	100.16	75.430
4	25	84.600	93.582	92.362	82.873	53.574
2	14.3	74.087	70.280	43.512	60.066	67.965
0	0	76.69	46.618	77.543	60.508	47.088
0	0	53.353	64.603	63.954	70.959	95.135

The fuel blends chosen were a mix of hydrogen and ethylene diluted with nitrogen. The blends were run at stoichiometric equivalence the amount of dilutant equal to the amount of oxygen. Table 22 presents the velocity data calculated from the shadowgraph images. It was found that the fuel blends with the highest amount of

hydrogen, had the fastest velocity. Hydrogen typically has a higher CJ point than ethylene, which is why this phenomenon occurred. Table 23 presents the velocities standard deviation. No conclusion can be made about how the standard deviations varied based on fuel blend.

Table 22. Velocity of the shadowgraph stoichiometric fuel blends.

H_2 (mol)	Ch_2H_4 (mol)	O_2 (mol)	N_2 (mol)	Dilution (%)	Region 1 (m/s)	Region 2 (m/s)	Region 3 (m/s)	Region 4 (m/s)	Region 5 (m/s)	Extension (m/s)
0.5	1.5	4.75	4.75	41.3	2075.6	2102.1	2117.7	2101.2	2079.6	2100
1	1	3.5	3.5	35.5	2100.4	2124.6	2121.2	2123.7	2136.5	2008
3	1	4.5	4.5	34.6	2135.3	2155.7	2155.6	2147	2155	2256

Table 23. Velocity standard deviation of the shadowgraph stoichiometric fuel blends.

H_2 (mol)	Ch_2H_4 (mol)	O_2 (mol)	N_2 (mol)	Dilution (%)	Region 1 (m/s)	Region 2 (m/s)	Region 3 (m/s)	Region 4 (m/s)	Region 5 (m/s)
0.5	1.5	4.75	4.75	41.3	114.43	82.10	68.839	59.212	130.90
1	1	3.5	3.5	35.5	105.35	123.26	74.986	98.769	69.730
3	1	4.5	4.5	34.6	143.32	48.682	97.032	66.904	80.860

Vertical Schlieren was performed on ethylene-oxygen detonations and one mixed-fuel blend. Velocity data for the cases performed using shadow graph match with the velocities provided by the vertical Schlieren. The velocities calculated for the vertical schlieren when compared to the extension are with the standard deviation. Table 24 presents the velocity data for the vertical Schlieren. Table 25 presents the standard deviation of the vertical Schlieren data. The standard deviation for the vertical Schlieren is much higher than the shadowgraph standard deviation. This can be explained by vertical schlieren removing the vertical gradients and only allowing the horizontal

gradients through. The standard deviation does follow the general trend of the more diluent added, the more it varies.

Table 24. Velocity of the detonations captured by vertical Schlieren detonations.

H_2 (mol)	C_2H_4 (mol)	O_2 (mol)	N_2 (mol)	Region 1 (m/s)	Region 2 (m/s)	Region 3 (m/s)	Region 4 (m/s)	Region 5 (m/s)	Extension (m/s)
0	2	6	6	2069.4	2074.7	2085.4	2080	2075.3	2100
0	2	6	8	1997.4	1998.6	2001.5	2004.4	2020.5	2008
0	2	6	0	2284.2	2303.7	2309.5	2311.4	2312.3	2324
0.5	1.5	4.75	4.75	2086.6	2084.3	2114.2	2104	2100.8	2081

Table 25. Velocity standard deviation of the vertical Schlieren detonations.

H_2 (mol)	C_2H_4 (mol)	O_2 (mol)	N_2 (mol)	Region 1 (m/s)	Region 2 (m/s)	Region 3 (m/s)	Region 4 (m/s)	Region 5 (m/s)
0	2	6	6	209.86	165.48	78.514	115.67	102.09
0	2	6	8	189.98	215.06	150.37	184.60	182.77
0	2	6	0	160.84	171.77	120.35	102.87	77.830
0.5	1.5	4.75	4.75	207.78	241.22	82.701	78.651	106.96

Horizontal Schlieren was only performed on ethylene-oxygen. The velocity of the five different regions were similar to the velocity calculated in the extension portion. Table 26 contains the velocity data. A similar trend of velocity decreasing when more diluent was added was observed. Table 27 contains the horizontal Schlieren standard deviation data. The standard deviation did not observe the normal trend. This may be due to the vertical gradients being image.

Table 26. Velocity of the horizontal Schlieren detonations.

C_2H_4 (mol)	O_2 (mol)	N_2 (mol)	Region 1 (m/s)	Region 2 (m/s)	Region 3 (m/s)	Region 4 (m/s)	Region 5 (m/s)	Extension (m/s)
2	6	8	1983.7	1997.5	1991.3	1983.4	2004.9	2008
2	6	0	2134.3	2309.9	2308.1	2302.8	2299.6	2324
2	6	0	2296.6	2293	2286.5	2286.8	2280.2	2301
2	6	8	1993.6	2013.3	2028.6	2016.8	2001.1	2008

Table 27. Standard deviation of velocity for horizontal Schlieren detonations.

H_2 (mol)	C_2H_4 (mol)	O_2 (mol)	N_2 (mol)	Region 1 (m/s)	Region 2 (m/s)	Region 3 (m/s)	Region 4 (m/s)	Region 5 (m/s)
0	2	6	8	162.30	85.327	121.51	126.87	150.03
0	2	6	0	61.702	61.443	59.324	49.917	82.577
0	2	6	0	167.18	389.55	191.05	225.94	198.14
0	2	6	8	147.51	130.10	144.06	155.36	101.92

4.1.3. Shadowgraph vs Schlieren

For the mixed fuel, shadowgraph and vertical Schlieren were taken for both the mixed fuel diluted with nitrogen in the extension. The amount of hydrogen was 0.5 moles for both cases. Figure 51 is the shadowgraph of the mixed fuel blend. Figure 52 is the vertical schlieren for the fuel blend. This figure has some noise in the form of water droplets on the test section. Both of these images are the raw images taken at 5 MHz using the Shimadzu. They both show similar thickness in the detonation. The vertical schlieren helps bring out the movement of the transverse waves more.

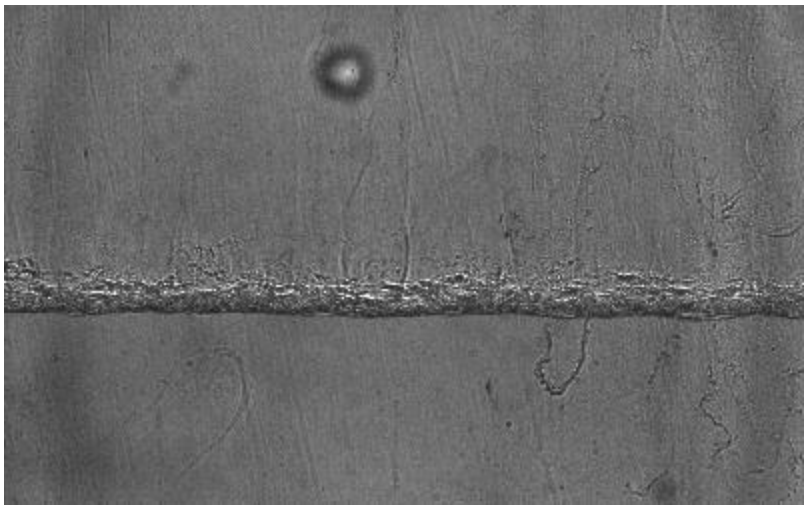

Figure 51. Shadowgraph of mixed fuel blend utilizing 0.5 mol of hydrogen and diluted with nitrogen.

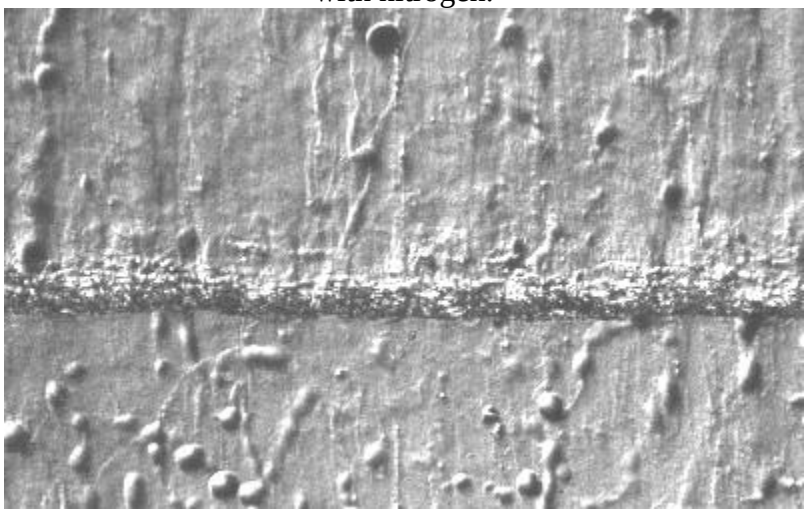

Figure 52. Vertical Schlieren of mixed fuel blend utilizing 0.5 mol hydrogen and diluted with nitrogen.

Hydrogen-oxygen detonation diluted with 8 moles of nitrogen were performed using shadowgraph and horizontal schlieren. Figure 53 is the shadowgraph image. Figure 54 is the horizontal schlieren image. These are both the raw images taken using the Shimadzu at 5 MHz. For both of these images the thickness of the detonation wave appears to be similar. Both of the images, the transverse waves sluffing off the main

detonation front can be seen. These waves are highlighted much more in the horizontal schlieren. The horizontal schlieren images gives in much better detail the structures behind the detonation wave front. Here it can be seen there are circular wave-like structures propagating in the back of the wave. The lines of the transverse waves are also better visualized using the horizontal schlieren. They are more visible when compared to the shadowgraph image.

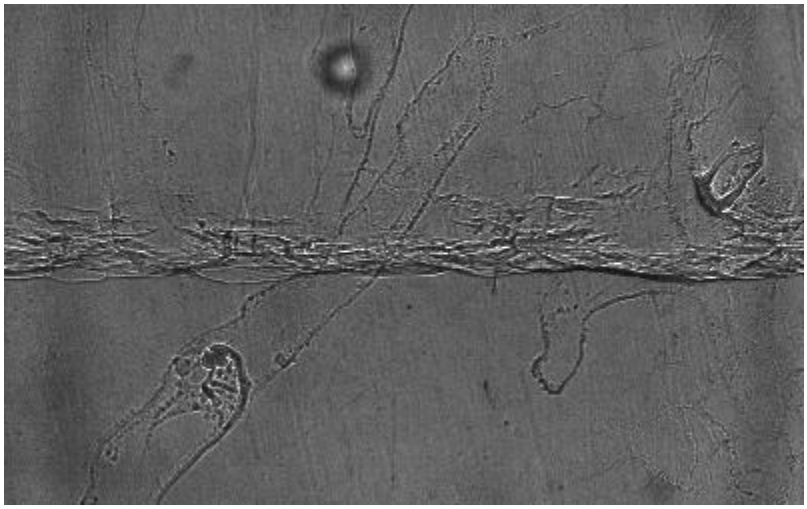

Figure 53. Shadowgraph of hydrogen-oxygen detonation diluted with eight mols of Nitrogen.

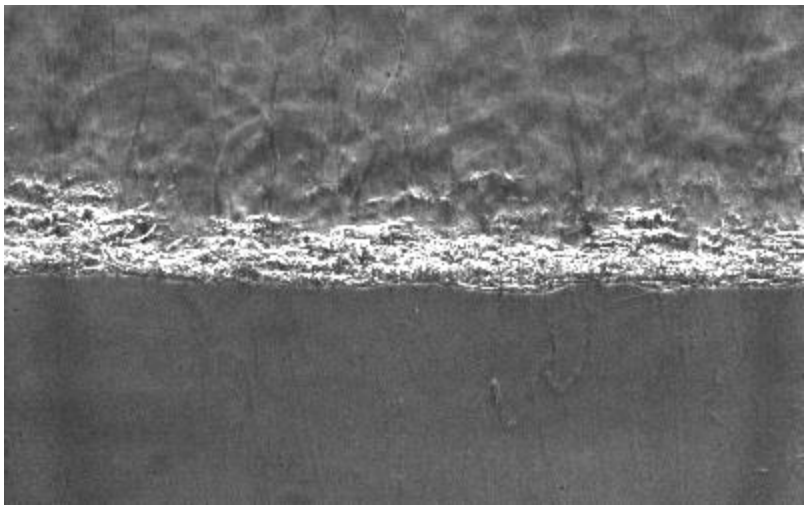

Figure 54. Horizontal Schlieren of hydrogen-oxygen detonation diluted with eight mols of Nitrogen.

4.1.4. Detonation Thickness

Detonation thickness calculations were only performed on shadowgraph images. Ethylene, hydrogen, and mixed fuels were diluted with nitrogen. Table 28 lists the detonation thickness for ethylene-oxygen detonations diluted with nitrogen. Table 29 is the detonation thickness for hydrogen-oxygen detonations diluted with nitrogen. Table 30 is the mixed-fuels diluted with nitrogen. Detonation thickness was observed to increase with nitrogen dilution. This was the case for both the ethylene-oxygen, and hydrogen-oxygen cases in nitrogen. The smallest detonation thickness was observed in ethylene with no dilution. The largest detonation thickness was observed in ethylene with seven moles of diluent. For the mixed fuel, the addition or subtraction of hydrogen did not have a significant effect on the detonation thickness. These two observations support that the

amount of diluent contributes to the detonation thickness more strongly than the type of fuel used. When comparing the mixed fuels to hydrogen, and ethylene, the mixed fuels had smaller detonation thickness by percentage of diluent.

Table 28. Detonation thickness for stoichiometric ethylene and oxygen in nitrogen.

Nitrogen (Moles)	Dilution (%)	Thickness(mm)
0	0	0.362
2	20	0.3903
6	42.9	0.7162
7	46.7	0.9366

Table 29. Detonation thickness for stoichiometric hydrogen and oxygen in nitrogen.

Nitrogen (moles)	Dilution (%)	Avg Thick (mm)
8	40	0.722
10	45.5	0.8319
6	33.3	0.6751
4	25	0.6155
4	25	0.5459
2	14.3	0.4487
0	0	0.3939
0	0	0.404

Table 30. Detonation thickness for mixed-fuel in nitrogen.

H_2 (mol)	C_2H_4 (mol)	O_2 (mol)	N_2 (mol)	Dilution (%)	Thickness (mm)
0.5	1.5	4.75	4.75	41.3	0.6412
1	1	3.5	3.5	35.5	0.6471
3	1	4.5	4.5	34.6	0.655

The case of diluting ethylene-oxygen detonations with argon told a different story. Ethylene-oxygen detonations diluted with argon showed no significant change in their

detonation width. Table 31 shows all the average thickness of the detonation through the image data set.

Table 31. Detonation thickness for stoichiometric ethylene and oxygen in argon.

Argon (moles)	Dilution (%)	Trial	Average Thickness
9	69.2	1	0.3809
10	71.4	1	0.3439
6	60	1	0.4646
3	42.9	1	0.4304
0	0	1	0.45
0	0	2	0.3846

4.1.5 Cell size

The soot foils were composed and analyzed using the method described in Chapter 3. Most of the data were captured using the Shimadzu at 5 MHz (with only two cases at 10 MHz). The combination of the wave velocity, frame rate, and suspected cell sizes made for poor spatial resolution in general. However, the mixed-fuel cell sizes were calculated. Multiple cells were visually resolved in this data set allowing for a calculation of an average. Table 32 lists the cell size averages.

Table 32. Cell sizes for the shadowgraph mixed fuel.

H_2 (mol)	C_2H_4 (mol)	O_2 (mol)	N_2 (mol)	Cell size (mm)
0.5	1.5	4.75	4.75	2.214
1	1	43.5	3.5	2.312
3	1	4.5	4.5	2.097

Further work needs to be done with creating the soot foils. The next step is to take data at 10 MHz using the Shimadzu and refining the algorithm to produce the soot foils. Another possible method to calculate the cells is to perform chemiluminescence and do time-average intensity mapping from data taken at 10 MHz. From the literature [27,28,29], on cell size and dilution, cell size should decrease with decreased dilution.

In this study, both ethylene-oxygen detonations were diluted with both nitrogen and argon. Mole for mole, the nitrogen cases had greater standard deviations in their velocity. This can be ascribed by nitrogen having much larger cells when compared to argon with similar percent dilutions [26,28]. It can be concluded that the addition of dilution decreases wave stability. The diluent argon decreases the stability of detonation at a much lower rate than the use of nitrogen as a diluent. This decrease in stability is related to how large the cells of the detonation become with the addition of dilution.

4.2 Analysis of Horseshoe Channels

The following section contains the analysis of different horseshoe channel configurations with different fuels. Equivalence ratios (Φ) varied for the fuels. The first configurations tested and analyzed were those utilizing ethylene-air. The Φ varied from 0.7-1.8. The second round of testing used hydrogen-air detonations. Here the Φ varied between 0.5-2.0. The Phantom V711 camera was used as the acquisition system. The framerate and resolution varied throughout the tests.

4.2.1. Categorizing Wave Structure

The first study with ethylene produced only unstable results. The second study done with hydrogen-air produced stable and unstable events. The classifications of these waves were broken down by stable, unstable, unstable with outer wave restart, and unstable with inner wave restart.

A stable wave consists of having a defined detonation wave front propagate and maintain its front over the entire test section. For larger channels, the inner and outer wave only deviate by 2 degrees. For smaller channels, the deviation can be up to three degrees. Stable waves were observed in only the hydrogen test data.

An unstable event was categorized by the leading and lagging of the inner radius when compared to the outer radius of the wave. These events are typically described as the inner wave lags behind the outer wave. The inner wave will then catch up or overshoot past the outer wave. Figure 55 is an example of the leading and lagging event. For this specific run the inner radius (R_i) was 8 in, the outer radius (R_o) was 10 in and Φ of 1.6. A) The detonation wave front was linear. B) The inner wave begins the process of lagging behind the outer wave. C) The inner wave continuous to lag behind the outer wave. D) The inner wave catches up with outer wave and detonation wave front is uniformed.

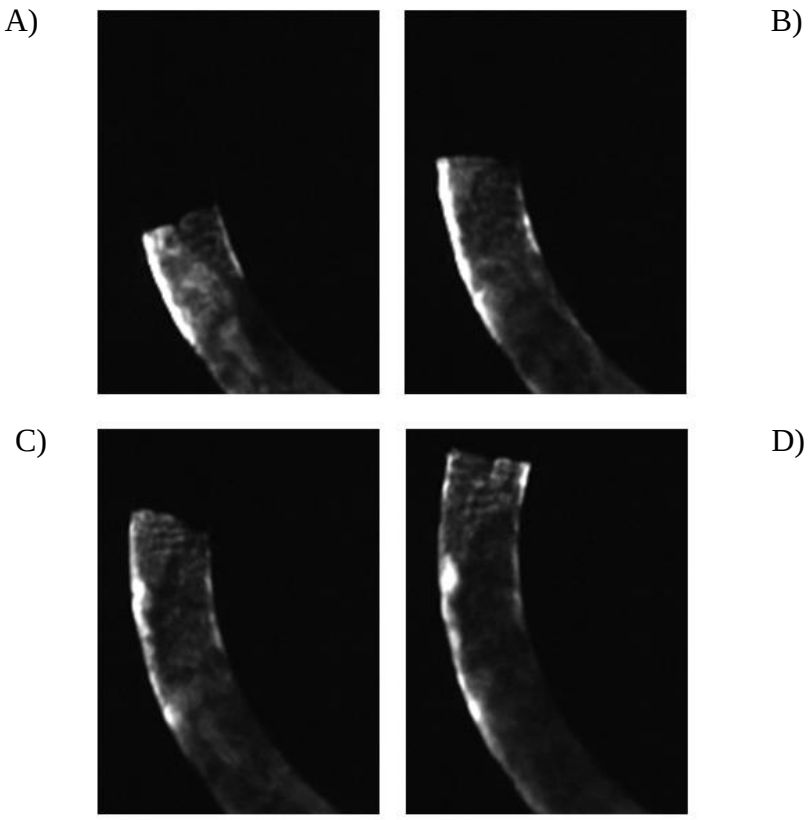

Figure 55. Example of an unstable event. Images are from ethylene-air detonation, Configuration 2 with an Φ of 1.6.

An unstable restart event can be described as a detonation wave dying and then suddenly propelling itself forward. Figure 56 is an example of an unstable restart event. The data for this image came from a run with an R_i of 8 in, Ro of 10 in, and an Φ of 1.2. In A) the detonation wave appears to be dissipating. The outer wave has a highly intense area jutting out from the middle of the detonation. B) The reignition of the outer wave begins to propagate across the channel with. C) The outer wave fully engulfs the channel width. D) The detonation wave continues as if nothing has happened. The restart was also

marked by having a much less intense wave moving in the opposite direction of the main propagating wave. This retonation can be somewhat observed in the images.

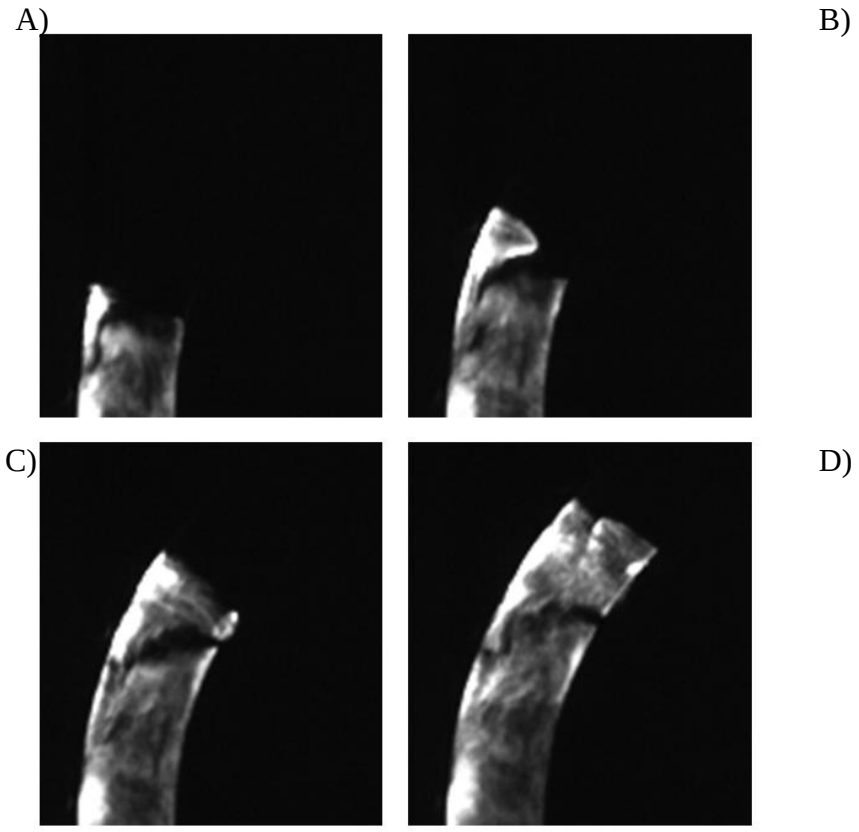

Figure 56. Example of an outer wave reignition event. Images are from ethylene-air detonation Configuration 2 with Φ was 1.7.

An unstable inner wave restart is similar to the outer wave restart. The restart event occurs in the outer wave and the retonation is still present. Figure 57 is an example of how an inner wave reignitions resembles. In A) the inner wave begins to lag behind the outer wave. B) The inner wave catches back up and speeds past the outer wave, with

a highly intense event occurring. C) The wave continues to propagate down the test section. In both C) and D) the retonation event can be clearly seen. This type of deflagration-to-detonation transition (DDT) was only observed in the ethylene data.

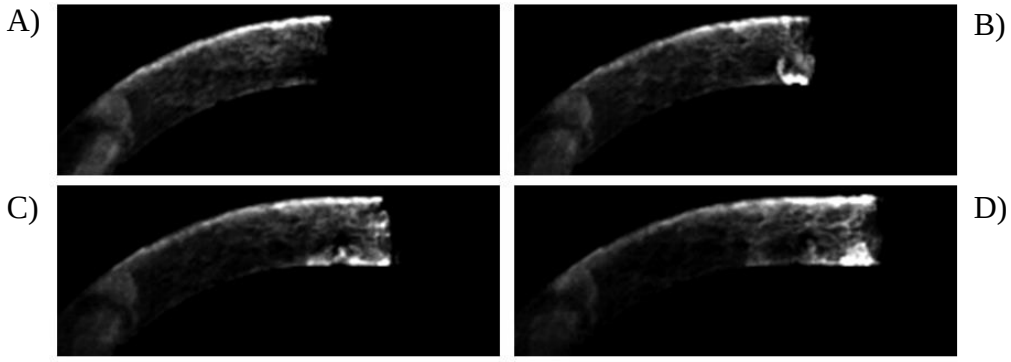

Figure 57. Example of an unstable inner wave start event. Images are from ethylene-air detonation Configuration 3 with Φ of 1.1.

These wave back up events are called retonation. In these events the detonation dissipates and transitions into deflagration. There are still hot hydrocarbons present where the wave failed. These unburned pockets can be thought of as potential energy for a new wave. The outside curve of the test-section is reinforcing the wave, while the inner curve is a point of continuous failure. When there is complete failure in both the inner and outer wave, a reflected shock from the inner radius hits the deflagration in the outer wave and transitions the combustion process into detonation.. The process is known as DDT. The unburned pockets present in the channel are then combusted by a detonation. The

unburned pockets give fuel to the detonation propagating in the opposite direction of the main propagating detonation.

Wave dissipation consisted of a detonation propagating through the straight portion of the channel, then proceeding to die on the curved portion or second straight portion. Wave dissipation is similar to an outer wave restart, in which the detonation wave front loses its definition. The only difference is that wave dissipation does not have the bright intensity event propelling the wave forward. Instead, the wave continues to lose its defined wave front, slow in velocity, and dissipate.

A stable wave consists of having a defined detonation wave front propagate and maintain its front over the entire test section. For larger channels, the inner and outer waves only deviate by two degrees. For smaller channels, the deviation can be up to three degrees. Stable waves were observed in only the hydrogen test data.

4.2.2. Detonation Propagation Velocity

Hydrogen-air detonations were the only combination to produce stable waves in the data sets taken. Most of the stable hydrogen-air detonations were produced from Configuration 1 and Configuration 7 which shared a similar R_i/R_o. One observation from the speed code output was that stable waves' outer and inner velocities did not vary greatly and resembled a straight line. Figure 58 is a non-dimensional speed versus angle around the curve for a stable wave. D is the velocity around the curve, while D_{str} is the velocity of the detonation in first straight-away. Figure 59 is the total velocity of the run. The gray lines mark the transition from the straight potion to the curve and vice versa. This data shown in Figure 58 and Figure 59 come from Configuration 7. Configuration 7

possessed an inner radius of 10.04 in and an outer radius of 12 in. The ER of the data was 1.2. The camera acquired the data at a frame rate of 17,000 fps.

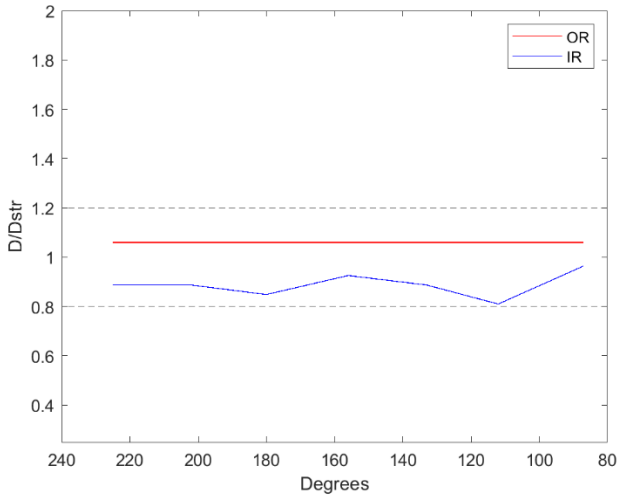

Figure 58. Stable wave non-dimensional velocity data around the curve. Data is from hydrogen-air detonation, Configuration 7, ER of 1.2.

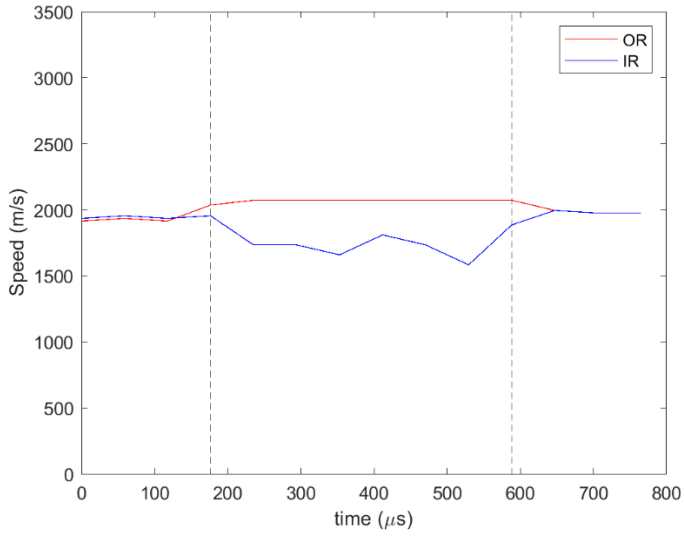

Figure 59. Stable wave velocity for entire horseshoe. Data is from hydrogen-air detonation Configuration 7, ER of 1.2

Examining the speed code output, normalized velocity of an unstable ethylene wave can be classified by outer wave speed varying around 0.8-1.2 times the normalized value. The inner wave non-dimensionalized value drops significantly comparted to the outer wave value. The inner wave will then speed up to catch the outer wave, causing the inner wave to move faster than the outer wave. Occasionally, the inner wave velocity increased dramatically, causing the inner wave to overshoot the outer wave. After overshooting, the inner wave slowed down to try to maintain the detonation wave front with the outer wave, causing the pattern to repeat. Figure 60 is the non-dimensionalized speed around the curved portion of test section. D is the velocity around the curve, while D_{str} is the velocity of the detonation in first straight-away. The data set used to produce this image had an outer radius of 12 in, inner radius of 9.6, and an ER of 1.2. The acquisition system captured 63,000 fps. Figure 61 is the speed of the entire run the dotted lines mark the transition from the straight potions to the curved portions.

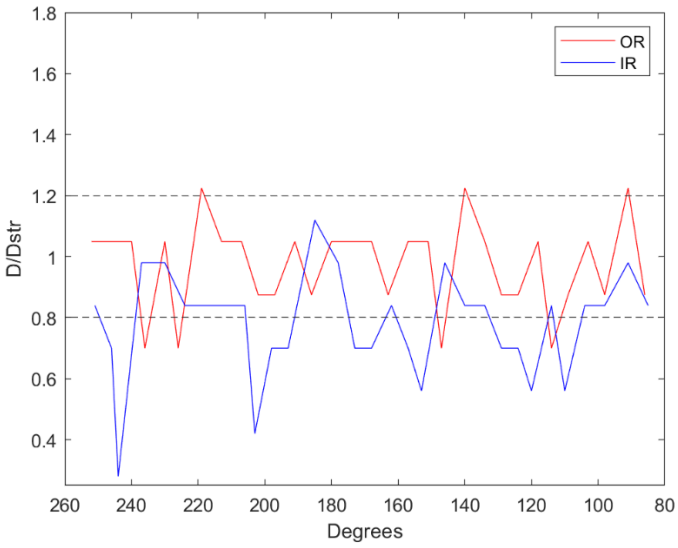

Figure 60. Unstable non-dimensional velocity data for ethylene-air detonation, Configuration 3 with an ER of 1.2.

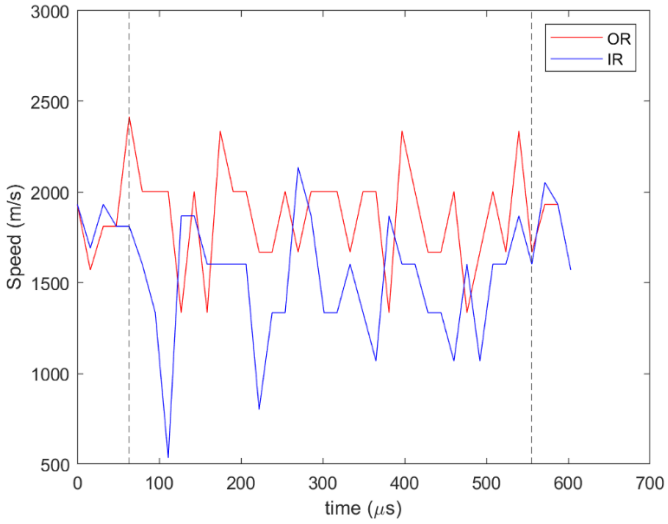

Figure 61. Unstable velocity data across entire horseshoe test-section. Data is from ethylene-air detonation, Configuration 3 with an ER of 1.2

Unstable hydrogen data can occasionally appear similar to the ethylene but only infrequently. For most unstable cases with hydrogen, the outer wave detonation speed is

consistent throughout while the inner wave speed will have varying velocities. From examining the code, it appeared that the outer wave was stable while the inner wave was unstable. Figure 62 shows the non-dimensional run of an unstable wave with the appearance of a stable outer wave and unstable inner wave. D is the velocity around the curve, while D_{str} is the velocity of the detonation in first straight-away. Figure 63 showcases the entire run's velocity. This data was taken with an inner radius of 9 in, outer radius of 6.37 in, hydrogen-air ER of 1.2, and a camera acquisition rate of 17,000 fps.

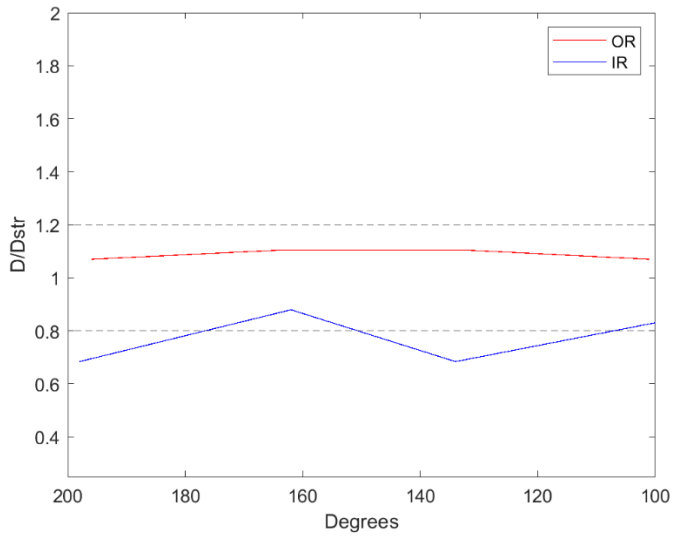

Figure 62. Non-dimensional velocity data plotted across the curved portion of the test-section. Data is from hydrogen-air detonation, Configuration 6 with an ER of 1.2

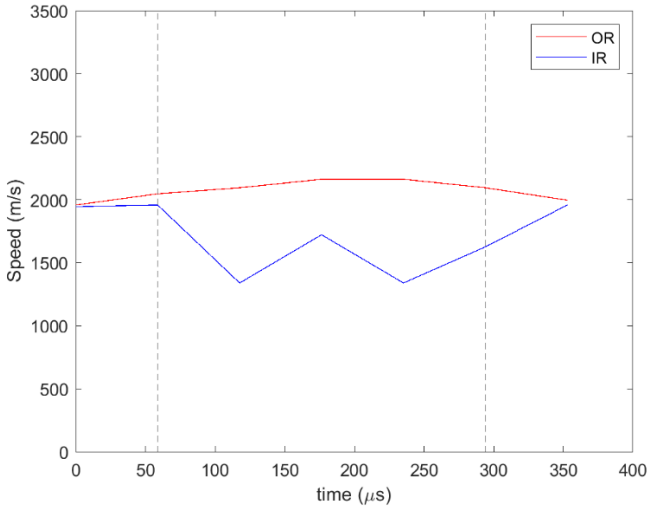

Figure 63. Velocity data for entire horseshoe test-section. Data is from hydrogen-air detonation, Configuration 6 with an ER of 1.2.

An outer wave restart can be characterized by examining the speed code and seeing, the outer wave and the inner wave slowing down, and then rapidly speeding back up. When examining the video, this wave restart phenomena can be characterized by the wave dying with the inner wave lagging behind the outer wave. Suddenly the wave propelled itself forward, resulting in a sharp increase in speed. Often times, the images brightened in the restart location but not always. After the restart event, typically the wave speed dropped to the expected speed of the detonation. Figure 64 is an example of a non-dimensional speed restart event. The conditions for this run were an outer radius of 10 in, an inner radius of 8 in, and an ER of 1.7. The data was collected at 58,000 fps. D is the velocity around the curve, while D_{str} is the velocity of the detonation in first straight-away .The reignition event occurred around 205 degrees in the curved portion of the channel. Figure 65 is the data for the entire run. The dotted grey lines mark the transition

from straight to curved portion and vice versa. Hydrogen outer wave restart events occur similar to the ethylene restart events.

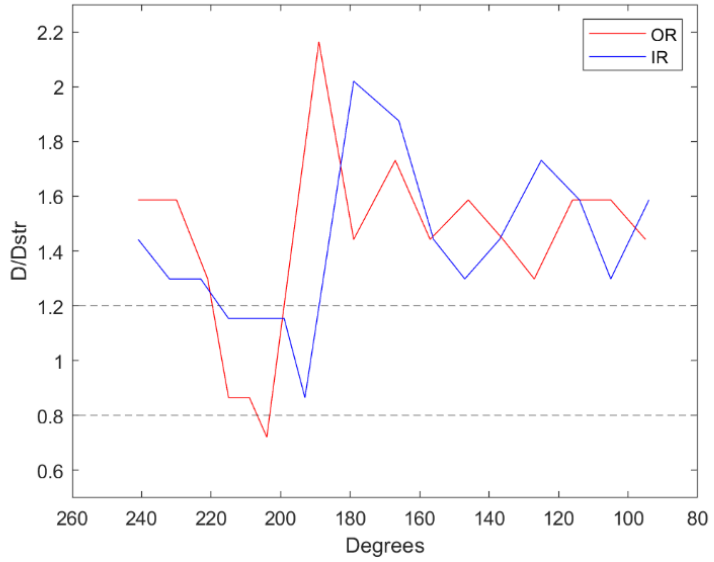

Figure 64. Outer wave reignitation non-dimensional velocity data for an ethylene-air detonation around the curve. Data is from ethylene-air, Configuration 2 with an ER 1.7.

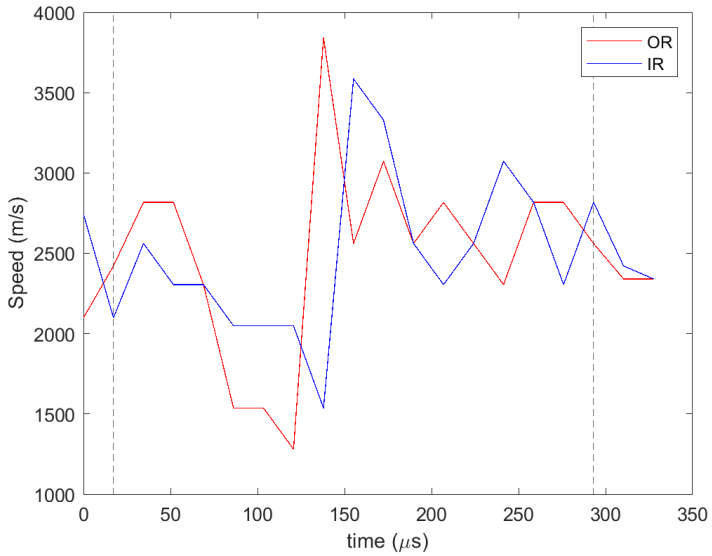

Figure 65. Outer wave restart velocity data for the entire horseshoe test-section. Data is from ethylene-air detonation, Configuration 2 with an ER of 1.7.

For ethylene, the reignitions also appeared to have a high intensity event propagating backwards from the propagating direction of the wave propagation called a retonation. This event can be examined in the video but also be seen in the polar mesh. Figure 66 is the non-dimensional speed data from a run of Configuration 2, possessing the inner radius of 8 in, outer radius of 10 in and an ethylene-air ER of 1.7. The camera acquisition recorded at 58,000 fps. This data possessed a restart event which occurred around 200 degrees. Figure 67 is the outer wave polar mesh of the Figure 66. The restart occurred around 200 degrees. In the image, the high intensity even slowly moves back through the curved portion of the test-section.

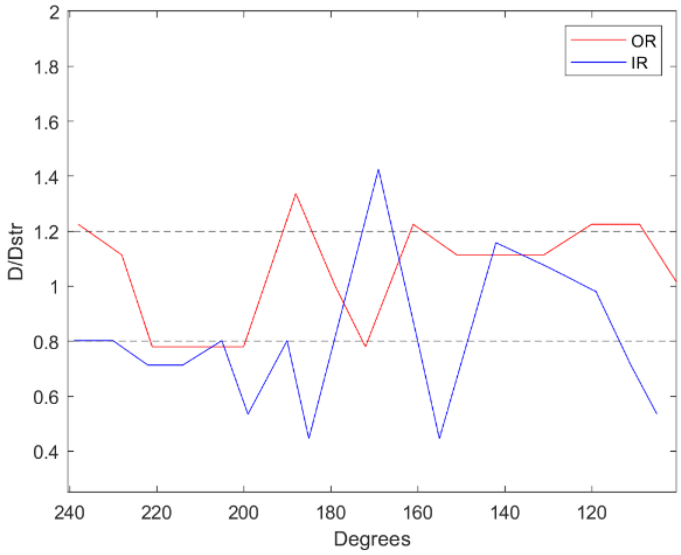

Figure 66. Non-dimensional speed around curved portion of Configuration 2 for ethylene-air detonation. ER was 1.7 for the run.

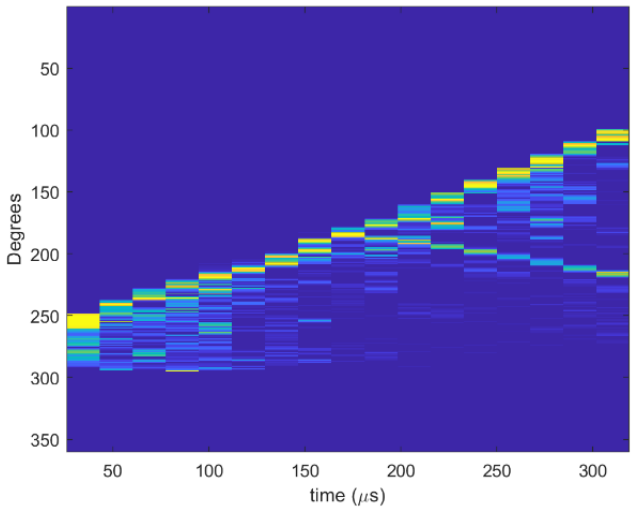

Figure 67. Outer wave polar mesh of ethylene-air detonation Configuration 2. ER for the run was 1.7.

Hydrogen data with the outer wave restarts did not have much of a wave 'back-up' event. Figure 68 is the velocity data for hydrogen-air detonation across horseshoe channel. Figure 69 is the outer wave polar mesh of a wave back for hydrogen. The data comes from Configuration 8 with an inner radius of 9.3 in, outer radius of 12 in, an ER of 1.5, and an acquisition rate of 17,000. The wave restart occurred around 180 degrees. There appears to be something resembling the wave back-up even seen in the ethylene data but only last for a frame in Figure 69 and can be easily mistaken as noise.

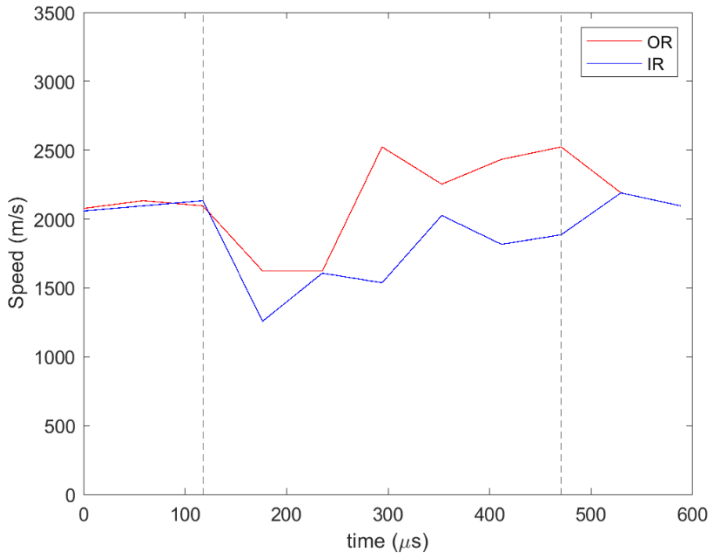

Figure 68. Hydrogen-air detonation restart velocity data across entire horseshoe channel. Data came from Configuration 8 with an ER of 1.5.

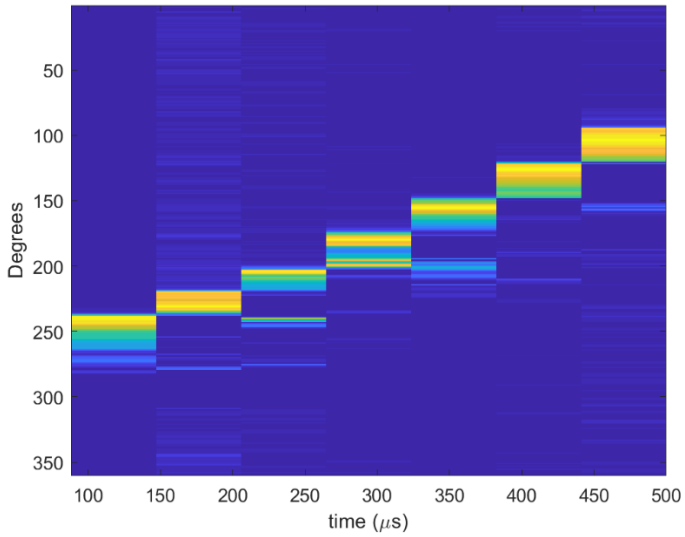

Figure 69. Outer wave polar mesh for restart event occurring at 180 degrees. Data comes from Configuration 8 with an ER of 1.5.

The speed code for cases with the inner wave restart either did not work due to images being too dark or the inner wave restart did not occur in the curved portion of the

test-section. What can be noted is the loss of the detonation wave front and the inner wave speeding forward to define the wave front, and the wave retonation event occurring.

4.2.3 Equivalence Ratio Test Classifications

Figure 70 through Figure 73 are all the ethylene-air detonation classifications with their equivalence ratios. Ethylene-air Φ varied from 0.7-1.7. The number of trials varied for the different configurations. Configuration 2 was run on two separate test days. This configuration is represented in Figure 70 and Figure 73. The different classifications found in the ethylene data were unstable wave, unstable wave-1 outer restart, unstable wave-2 outer restarts, failure from start, wave dissipation, and failure from start-reignition.

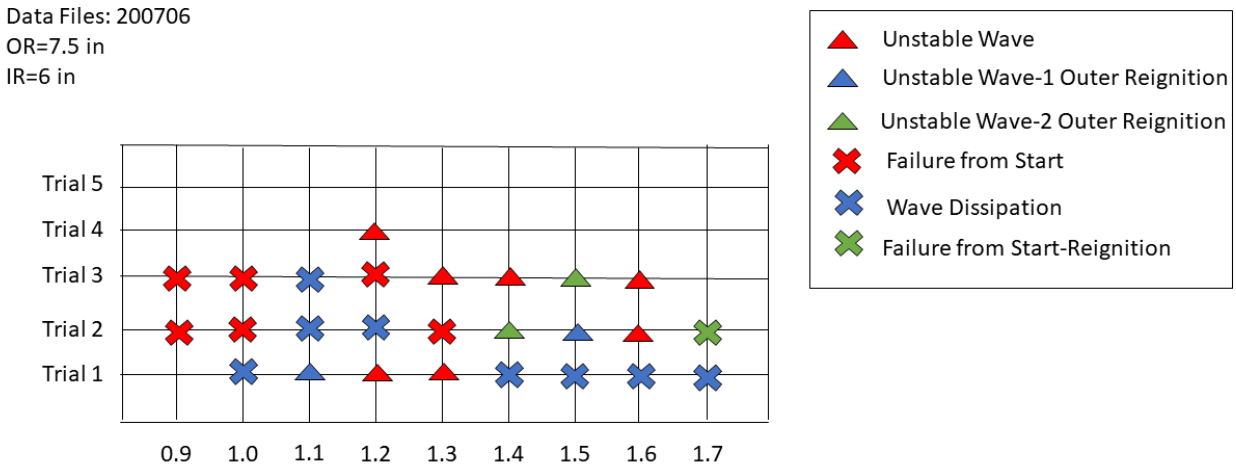

Figure 70. Ethylene-air classifications for Configuration 1.

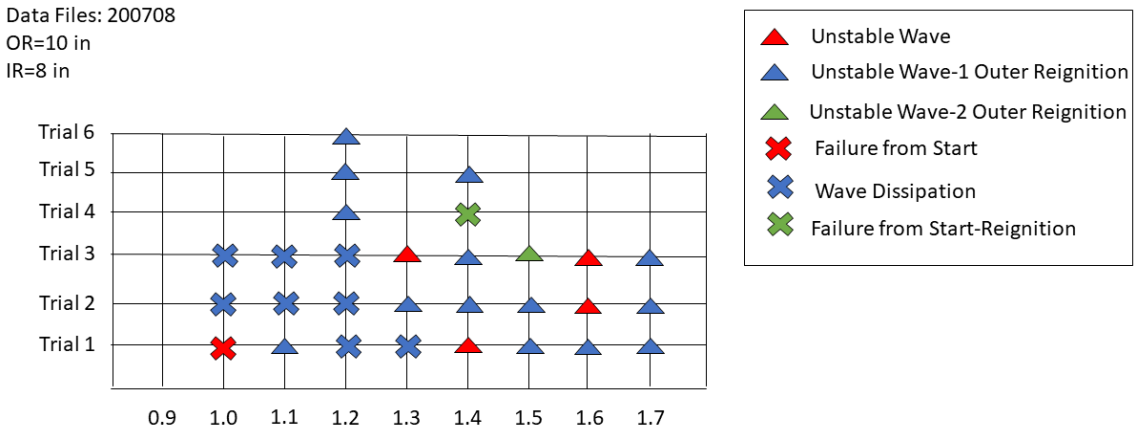

Figure 71. Ethylene-air classification for Configuration 2, round 1.

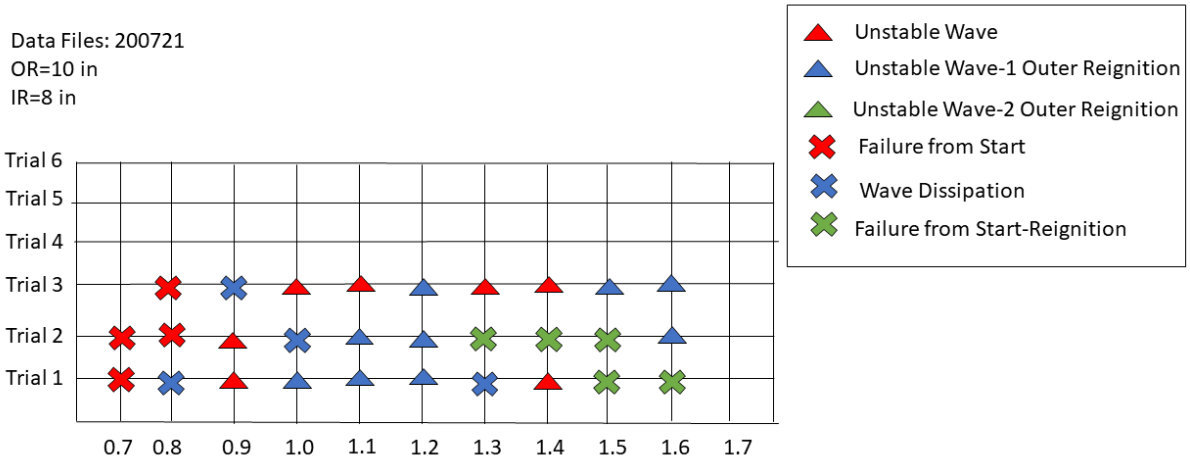

Figure 72. Ethylene-air classification for Configuration 2, round 2.

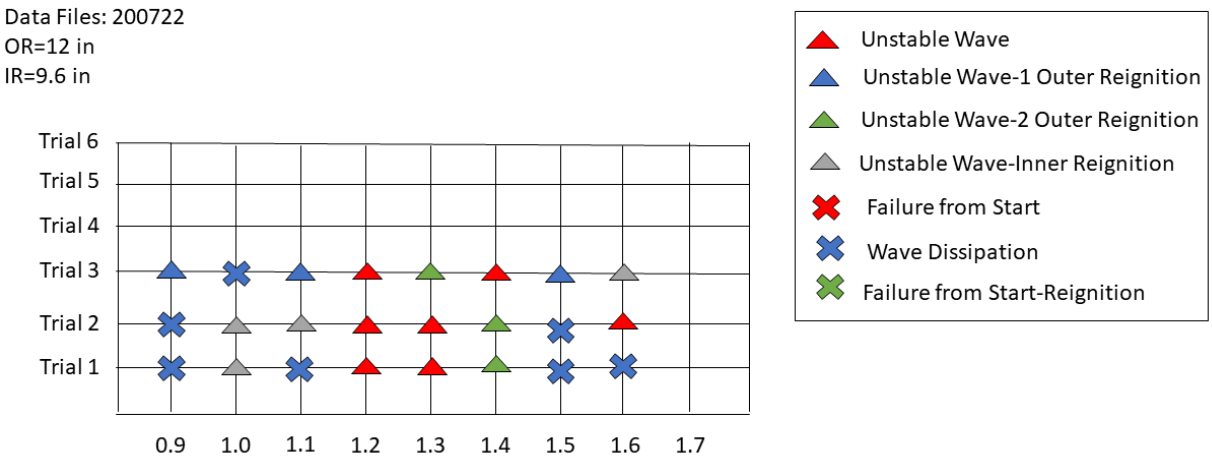

Figure 73. Ethylene-air detonation classification for Configuration 3.

Figure 74 through Figure 82 are all the classifications for the hydrogen-air detonations compared to 0.5-2.0 Φ. Trial 1 for all configurations suffered from the polycarbonate wall cracking. Configuration 6, Configuration 7, and Configuration 8 both suffered from catastrophic polycarbonate cracks resulting in missing data. Only 5 different classifications were observed such as stable wave, unstable wave, unstable wave- 1 outer reignition, failure from start and wave dissipation. No failure from start-reignitions were observed. All Trial 2 of the hydrogen-air detonations had thicker polycarbonate walls, resulting in no cracking of the polycarbonate. Due to no cracks in the polycarbonate, Trial 2 produced more reliable results.

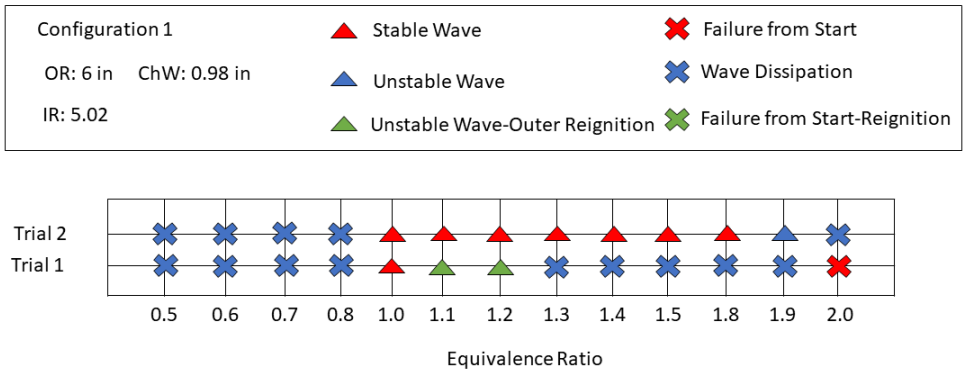

Figure 74. Hydrogen-air detonation classification for Configuration 1.

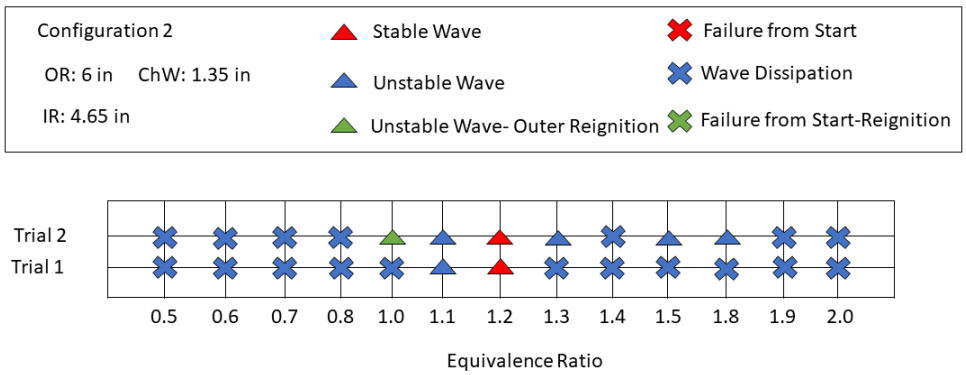

Figure 75. Hydrogen-air detonation classification for Configuration 2.

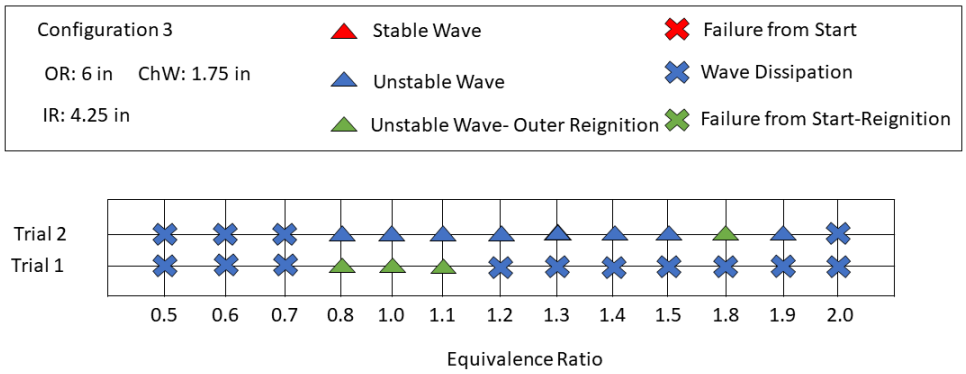

Figure 76. Hydrogen-air detonation classification for Configuration 3.

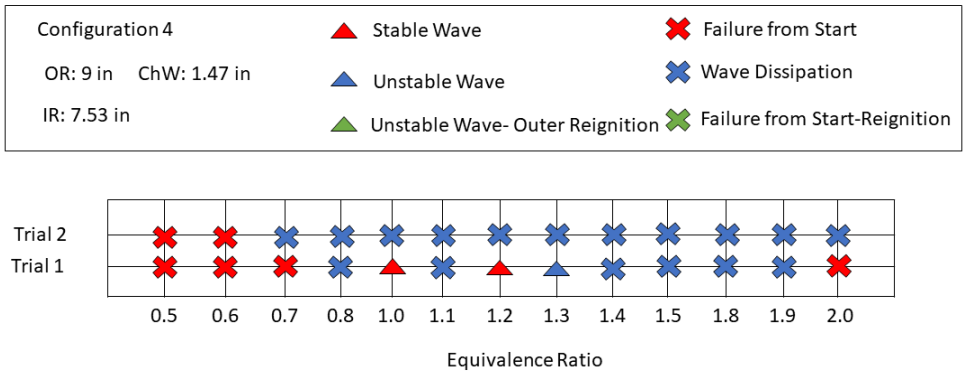

Figure 77. Hydrogen-air detonation classification for Configuration 4.

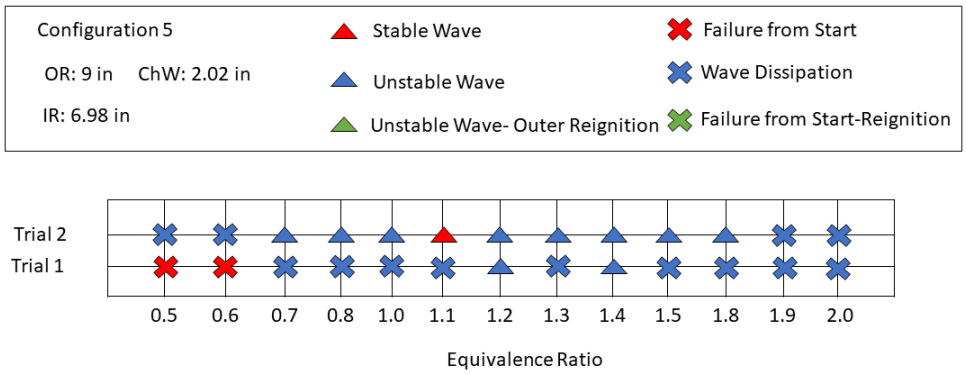

Figure 78. Hydrogen-air detonation classification for Configuration 5.

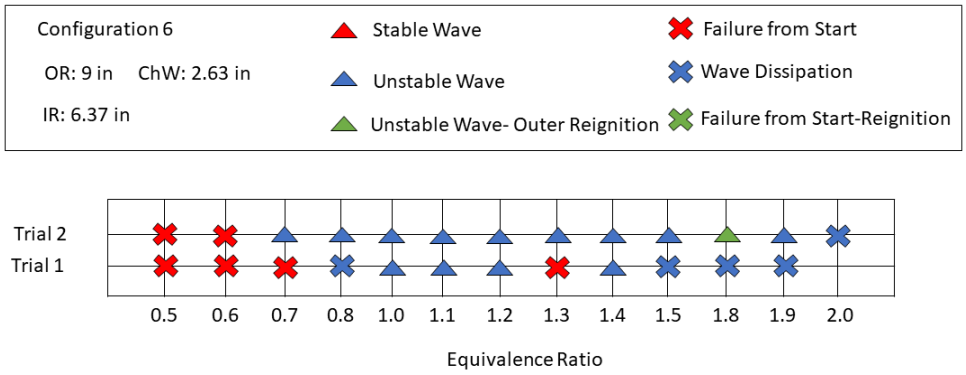

Figure 79. Hydrogen-air detonation classification for Configuration 6.

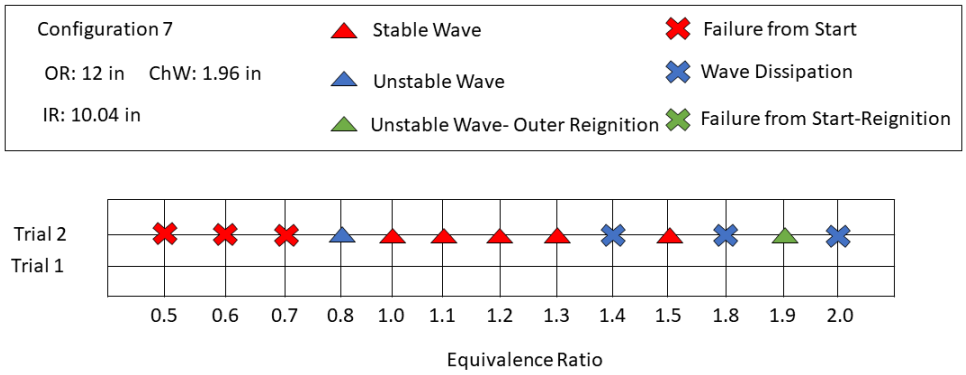

Figure 80. Hydrogen-air detonation classification for Configuration 7.

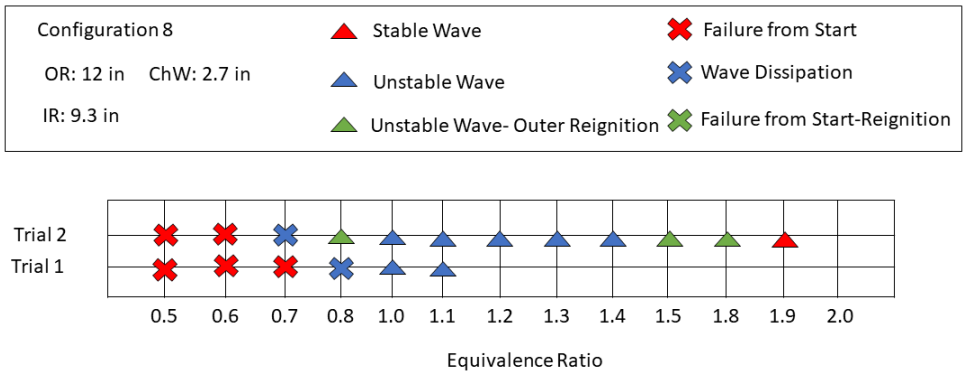

Figure 81. Hydrogen-air detonation classification for Configuration 8.

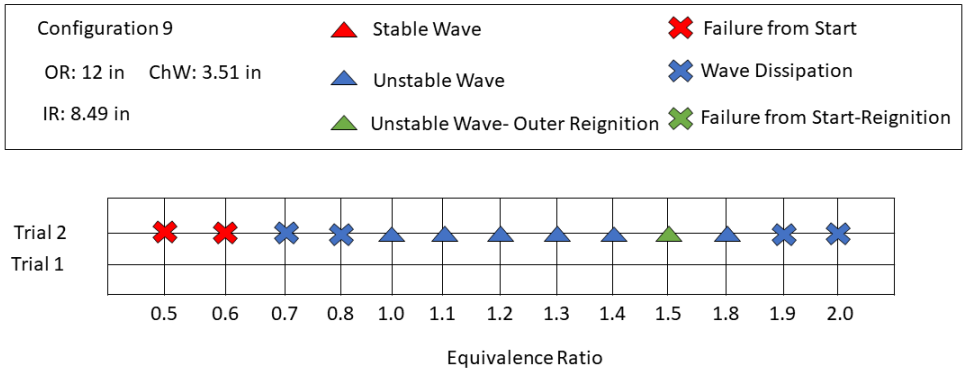

Figure 82. Hydrogen-air detonation classification for Configuration 9.

4.2.4 Wave speeds compared to Chapman-Jouguet Point

This section compares the detonation velocities to the theoretical value of their velocity known as the Chapman-Jouguet point.

4.2.4.1 Ethylene-air detonations Compared to Chapman-Jouguet Point

Ethylene-air detonations were compared to their so-called upper Chapman-Jouguet (CJ) point. Most of the data was either overdriven or underdriven. This may be attributed to the detonation in the first straight potion of the test section not being stable, prompting the rest of the sections to not be stable.

Ethylene-air detonations for Configuration 1 (inner radius of 6 in, and outer radius of 7.5 in) were much slower than the CJ. Table 33 contains the mean speed of the outer wave for all successful runs through speed code. Table 34 showcase all the mean speeds of the successful inner wave speeds. Table 35 contains the mean outer wave speeds for

the first straight portion of the test-section. From examining the three tables, the detonation coming into the test-section was under-driven. Through the curved portion, the outer wave and inner wave continued to be under driven, with the inner wave much slower than the outer.

Table 33. Mean outer wave speed for ethylene-air Configuration 1

Φ	CJ (m/s)	Trial 1 (m/s)	Trial 2 (m/s)	Trial 3 (m/s)	Trial 4 (m/s)
1.1	1821.5	1333.9			
1.2	1841.9	1388.7			1379.3
1.3	1857.8	1379.3		1385.8	
1.4	1869.5		1304.3	1407.5	
1.5	1877.4		1407.5	1398.1	
1.6	1881.8		1473.2	1435.6	
1.7	1883.3		1066.7		

Table 34. Inner wave speed for ethylene-air Configuration 1

Φ	CJ (m/s)	Trial 1 (m/s)	Trial 2 (m/s)	Trial 3 (m/s)	Trial 4 (m/s)
1.1	1821.5	1074			
1.2	1841.9	1118.5			1111
1.3	1857.8	1111		1108.7	
1.4	1869.5		1058.4	1111	
1.5	1877.4		1156	1126	
1.6	1881.8		1178.5	1148.5	
1.7	1883.3		1185.3		

Table 35. Outer wave mean speed in first straight portion for Configuration 1

Φ	CJ (m/s)	Trial 1 (m/s)	Trial 2 (m/s)	Trial 3 (m/s)	Trial 4 (m/s)
1.1	1821.5	1359.6			
1.2	1841.9	1216.5			1320.7
1.3	1857.8	1325.5		1325.5	
1.4	1869.5		1337.9	1369.1	
1.5	1877.4		1419.8	1375.2	
1.6	1881.8		1387.4	1381.2	
1.7	1883.3		931.38		

Ethylene-air detonations for Configuration 2, Round 1 velocities when compared to CJ point were much higher. Table 36 are the mean outer wave velocities of Configuration 2, round 1. In general the outer wave velocities were over driven when compared to the CJ point. Table 37 are the mean inner wave velocities. In general, these are very similar to the CJ point, but the wave is still over driven. The inner wave will always be slower than the outer wave. For the inner wave not to be considered overdriven, it would need to be slower than the CJ point. Table 38 presents the speeds used to normalize the data. Here the straight away speeds are over driven.

Table 36. Mean outer wave speed for ethylene-air, Configuration 2, round 1

Φ	CJ (m/s)	Trial 1 (m/s)	Trial 2 (m/s)	Trial 3 (m/s)	Trial 4 (m/s)	Trial 5 (m/s)
1.1	1821.5	2278				
1.2	1841.9				2319.2	2214.1
1.3	1857.8		2337	2513.1		
1.4	1869.5	2276.5	2497.1	2470.7		
1.5	1877.4	2449	2418.8	2333.4		
1.6	1881.8	2513.1	2593.1	2657.1		
1.7	1883.3	2646.5	1908	2385		

Table 37. Mean inner wave speed for ethylene-air, Configuration 2, round 1

Φ	CJ (m/s)	Trial 1 (m/s)	Trial 2 (m/s)	Trial 3 (m/s)	Trial 4 (m/s)	Trial 5 (m/s)
1.1	1821.5	1822.4				
1.2	1841.9				1866.8	1811.6
1.3	1857.8		1805.6	1933.6		
1.4	1869.5	1741.5	1984.8	1976.6		
1.5	1877.4	1946.4	2418.8	2305		
1.6	1881.8	2513.1	2061.7	2609.1		
1.7	1883.3	2130.8	N/A	1831.2		

Table 38. First straight away section velocity of Configuration 2, round 1. Velocity in which wave was normalized.

Φ	CJ (m/s)	Trial 1 (m/s)	Trial 2 (m/s)	Trial 3 (m/s)	Trial 4 (m/s)	Trial 5 (m/s)
1.1	1821.5	2166.4				
1.2	1841.9				2084.2	2429.1
1.3	1857.8		2134.3	2266.8		
1.4	1869.5	2227.9	2538.8	2527.5		
1.5	1877.4	2407.2	2349.7	1968.5		
1.6	1881.8	2259.8	2477.1	2535.2		
1.7	1883.3	2672.6	N/A	2299.6		

Similar to Configuration 2, round 1, Configuration 2, round 2 had overdriven detonations. Table 39 contains the mean outer wave velocity of Configuration 2, round 2. All detonation velocity presented in this table are overdriven. Table 40 presents the inner wave detonation velocity. Unlike round 1, the velocity presented here, in general, are overdriven. Table 41 presents the detonation velocity found in the first straight test-section. Majority of the detonation waves presented in this table are overdriven.

Table 39. Mean outer wave velocity of Configuration 2, round 2.

Φ	CJ (m/s)	Trial 1 (m/s)	Trial 2 (m/s)	Trial 3 (m/s)
0.9	1766.3	2474.4	2420	
1	1796.6	2426.4		2430.5
1.1	1821.5	2187.6	2459.8	2519.1
1.2	1841.9	2503.7	2488.2	2552.8
1.3	1857.8		2328	2565.5
1.4	1869.5	2438.2		2590.6
1.5	1877.4	2601.9	2503.7	2585.5
1.6	1881.8	2764.5	2534.6	2472.8

Table 40. Mean inner wave velocity of Configuration 2, round 2.

Φ	CJ (m/s)	Trial 1 (m/s)	Trial 2 (m/s)	Trial 3 (m/)
0.9	1766.3	1991.2	1947.3	
1	1796.6	1978.2		1967.8
1.1	1821.5	1719.7	1967.8	2040
1.2	1841.9	1990.6	2040	1989.9
1.3	1857.8		1885.8	2052.4
1.4	1869.5	1963.7		2030.8
1.5	1877.4	2107.7	1978.2	2042.2
1.6	1881.8	2197.7	1990.6	1978.2

Table 41. First straight away velocity of Configuration 2, round 2.

Φ	CJ (m/s)	Trial 1 (m/s)	Trial 2 (m/s)	Trial 3 (m/s)
0.9	1766.3	2427.7	2385.1	
1	1796.6	2434.1		2437
1.1	1821.5	2421.4	2540.8	2625.2
1.2	1841.9	1687.7	2674	2522.7
1.3	1857.8		1779.7	2591.9
1.4	1869.5	2341.6		2409.2
1.5	1877.4	1795.9	1882.9	2674.2
1.6	1881.8	2288.3	2631.2	2605.3

Ethylene-air detonations for Configuration 3 were near the CJ point. Most of the successful data collected for this configuration could not be run through the speed code due to the quality of the images. The images were too dark for the code to work

appropriately on the image set. Table 42 presents the mean outer wave detonation velocity. These numbers hovered around the CJ point. Table 43 presents the mean inner wave velocity of the detonation wave. These numbers were underdriven compared to the CJ. This can be expected due to the outer wave velocity hovering around CJ point. Table 44 presents the velocity of the detonation which came into the curved portion of the test section. These numbers also hovered around CJ point.

Table 42. Mean outer wave velocity data of Configuration 3.

Φ	CJ (m/s)	Trial 1 (m/s)	Trial 2 (m/s)	Trial 3 (m/s)
1	1796.6	1724.8		
1.1	1821.5		1795.8	1813.8
1.2	1841.9		1847.2	1852.2
1.3	1857.8	1784.2	N/A	
1.6	1881.8		1802.7	1784.2

Table 43. Mean inner wave velocity of Configuration 3.

Φ	CJ (m/s)	Trial 1 (m/s)	Trial 2 (m/s)	Trial 3 (m/s)
1	1796.6	1397.6		
1.1	1821.5		1409	1433.2
1.2	1841.9		1477.7	1481.8
1.3	1857.8	1436.6		
1.6	1881.8		1451	1372.1

Table 44. Velocity of first straight away of test-section. Velocity used to normalize speed data.

Φ	CJ (m/s)	Trial (m/s)	Trial (m/s)	Trial (m/s)
1	1796.6	1812.5		
1.1	1821.5		1776.6	1731.1
1.2	1841.9		1803.5	1908
1.3	1857.8	1794.7		
1.6	1881.8		1916.7	1852.8

4.2.4.2 Hydrogen-air Detonations Compared to Chapman-Jouguet Point

Compared to the Ethylene data, hydrogen was much more stable. This may be attributed to the first straight sections consistently producing stable detonations. Trial 1 of the hydrogen data was less consistent due to the polycarbonate cracking. Trial 2 was the most consistent out of all data sets. This can be attributed to the stable detonations coming into the curved section, and no cracks forming in the polycarbonate.

The first hydrogen trial had more data in the smaller than in the larger configurations. The polycarbonate was more likely to crack earlier in the larger configurations. No runs from Configuration 7 were successful and they were removed from chart. Table 45 presents all the configurations mean outer wave detonation velocity. All outer wave velocity in the chart is close to CJ point suggesting that the detonation 'tries' to maintain the CJ point regardless of the classification. Table 46 contains the max velocity of the outer wave. The variation of the max velocity when compared to the CJ velocity depends on the stability of the wave. The restart events produced the highest velocities. Table 47 presents the mean inner wave velocity of the detonation for all configurations. All velocities were below the CJ point as expected. The decrease in velocity below CJ point correlated with the classification of the wave. The unstable waves had the lowest mean value, and the restart events had the highest mean value. This result is expected since unstable inner waves are constantly lagging behind the outer wave, and restart events were characterized by large velocity increases. Table 48 showcases that the speeds along the first straight portion of the test-sections are nearly at the CJ point which suggested a stable wave.

Table 45. Mean outer wave detonation velocity for all hydrogen trial 1 configurations.

Φ	CJ (m/s)	C1 (m/s)	C2 (m/s)	C3 (m/s)	C4 (m/s)	C5 (m/s)	C6 (m/s)	C8 (m/s)
0.8	1839.2			1669.1				
1	1932	1725.3		2058.6	2074.5		2163.9	1986.9
1.1	1966.1	1328.9	1858.3	1919.5			2110.3	1996.8
1.2	1994.3		2058.6		1931.4	2174.6	2088.8	
1.3	2018.2				1917.1		2088.8	
1.4	2038.8					2003		

Table 46. Max velocity of detonation outer wave for all hydrogen trial 1 configurations.

Φ	CJ (m/s)	C1 (m/s)	C2 (m/s)	C3 (m/s)	C4 (m/s)	C5 (m/s)	C6 (m/s)	C8 (m/s)
0.8	1839.2			1947.3				
1	1932			2336.8	2146		2432.2	2071.8
1.1	1966.1	2156.6		2169.9			2360.6	2161.9
1.2	1994.3		1947.3		2003	2432.2	2289.1	
1.3	2018.2		2114.2		2003		2289.1	
1.4	2038.8					2074.5		

Table 47. Mean inner wave detonation velocity for all hydrogen trial 1 configurations.

Φ	CJ (m/s)	C1 (m/s)	C2 (m/s)	C3 (m/s)	C4 (m/s)	C5 (m/s)	C6 (m/s)	C8 (m/s)
0.8	1839.2			1135				
1	1932	1297.2		1418.8	1864.7		1708.8	1515.9
1.1	1966.1	1160.6	1422.9	1330.1			1544.2	1957.5
1.2	1994.3		1578.2		1699.8	1620	1448	
1.3	2018.2				1674.5		1468.3	
1.4	2038.8					1525.7		

Table 48. Detonation velocity in first straight portion of the test-section for hydrogen-air detonations. Detonation speed used for normalization.

Φ	CJ (m/s)	C1 (m/s)	C2 (m/s)	C3 (m/s)	C4 (m/s)	C5 (m/s)	C6 (m/s)	C8 (m/s)
0.8	1839.2			1762.4				
1	1932	2020.8		1989.5	2055.3		1822.9	1889.5
1.1	1966.1	1990.3	1994.5	2016.5			1901.7	1930.8
1.2	1994.3		1975.3		1937.9	2086.8	1916.3	
1.3	2018.2				1949.9		2028.2	
1.4	2038.8					1985.7		

The second Hydrogen trial was more successful with respect to data collection due to the thicker polycarbonate. There were no successful waves for Configuration 4, so data from that configuration were not included in the tables. Table 49 contains the detonation's mean outer wave velocity. Stable waves appeared to hover right around the CJ point. Unstable waves were typically above the CJ point. Table 50 contains the detonation outer wave's max velocity. The max velocity of stable waves did not vary much from the mean, but there was high variance in the max velocity of the unstable waves. Table 51 contains the mean inner wave velocity. All velocities found on this table are below the CJ point. Table 52 contains all the velocity data of the detonation wave before entering the curved section. All the velocities were found to be around the CJ point, which indicated a stable wave entering the curved portion.

Table 49. Mean outer wave velocity for hydrogen-air detonations trial 2 configurations.

ER	CJ (m/s)	C1 (m/s)	C2 (m/s)	C3 (m/s)	C5 (m/s)	C6 (m/s)	C7 (m/s)	C8 (m/s)	C9 (m/s)
0.7						1824.1			
0.8	1839.2			2003	1837.6	2212.6	1878.8	1598.9	
1	1932	2058.6	1891.7	2132.8	1976.1	2111.2	1981.8	2027	2161.9
1.1	1966.1	2086.4	2030.8	2114.2	2107.9	2134.9	2046.1	2267	2372.1
1.2	1994.3	2156	2086.4	2267.2	2094.4	2128.1	2071.8	2267	2297
1.3	2018.2	2142	2058.6	2239.4	2094.4	2178.8	2084.7	2342.1	2282
1.4	2038.8	2156		2211.6	2161.9		1621.4	2297	2342.1
1.5	2057.2	2188.4	2156	2142	2161.9	2139.4	2071.8	2161.9	2086.9
1.8	2103.1	2114.2	2183.8	2225.5	2128.1	2229.5		2198	2216
1.9	2116.4	2016.9		2183.8		2188.9		2297	
2	2128.9								

Table 50. Max velocity of outer wave for hydrogen-air trial 2 configurations.

ER	CJ (m/s)	C1 (m/s)	C2 (m/s)	C3 (m/s)	C5 (m/s)	C6 (m/s)	C7 (m/s)	C8 (m/s)	C9 (m/s)
0.7						1959.2			
0.8	1839.2			2058.6	2094.4	2229.5	1981.8	2071.8	
1	1932	2114.2	2114.2	2225.5	1976.1	2229.5	2071.8	2342.1	2342.1
1.1	1966.1	2169.9	2058.6	2281.1	2107.9	2229.5	2071.8	2432.2	2612.3
1.2	1994.3	2281.1	2169.9	2336.8	2161.9	2161.9	2071.8	2342.1	2432.2
1.3	2018.2	2169.9	2225.5	2503.7	2229.5	2229.5	2161.9	2432.2	2522.2
1.4	2038.8	2225.5		2392.4	2229.5		2071.8	2432.2	2432.2
1.5	2057.2	2336.8	2448.1	2503.7	2229.5	2297	2161.9	2522.2	2522.2
1.8	2103.1	2169.9	2392.4	2503.7	2364.6	2499.7		2522.2	2342.1
1.9	2116.4	2336.8		2448.1		2364.6	2020.4	2522.2	
2	2128.9								

Table 51. Mean inner wave velocity for hydrogen-air detonations trial 2 configurations.

ER	CJ (m/s)	C1 (m/s)	C2 (m/s)	C3 (m/s)	C5 (m/s)	C6 (m/s)	C7 (m/s)	C8 (m/s)	C9 (m/s)
0.7						1281.5			
0.8	1839.2			1369.5	1425.2	1458.4	1539.6	1274.1	
1	1932	1699.1	1476.8	1523.9	1467.1	1422.6	1658.1	1640.6	1540.2
1.1	1966.1	1699.1	1638.5	1537	1582.4	1520.6	1711.9	1756.9	1603.9
1.2	1994.3	1803.8	1617	1576.4	1624.3	1506.2	1733.4	1756.9	1603.9
1.3	2018.2	1792.2	1609.8	1477.9	1611.2	1494.3	1722.7	1815.1	1582.7
1.4	2038.8	1768.9		1566.5	1611.2		1292	1780.2	1593.3
1.5	2057.2	1753.4	1638.5	1458.2	1676.7	1474.4	1720.9	1687.4	1455.2
1.8	2103.1	1780.5	1527.1	1625.7	1650.5	1558.8		1731.3	1567.8
1.9	2116.4	1734		1625.7		1472.8	1690.4	1781.8	
2	2128.9			1566.5					

Table 52. First straight portion detonation velocity of hydrogen-air detonations

ER	CJ (m/s)	C1 (m/s)	C2 (m/s)	C3 (m/s)	C5 (m/s)	C6 (m/s)	C7 (m/s)	C8 (m/s)	C9 (m/s)
0.7						1725.2			
0.8	1839.2			1833.4	1747	1921.2	1814.8	1834.3	
1	1932	1937.2	1932.9	1919.7	1856.6	1901.6	1875.3	2037.4	1955.6
1.1	1966.1	1974.9	1964.1	1950.7	1954.7	1946.7	1886	1980.1	2089.8
1.2	1994.3	1932.6	1966.1	2051.3	1984.5	1957.5	1954.1	2008.5	2130.6
1.3	2018.2	1960.1	1979	1993.6	1975.3	1969.4	2000.3	2087.7	2127.6
1.4	2038.8	1984.5		2039.5	1996		1976	2123.5	2133.7
1.5	2057.2	2002.7	1978	1982.5	2025.4	1913.5	1953.8	2132.4	2131
1.8	2103.1	1992.6	2030	1987.5	2008.5	2027.2		2122.9	2011.5
1.9	2116.4	2027.8		2079.4		1844.3	1997.8	2165.7	
2	2128.9								

4.2.5 Standard Deviation of Velocity compared to Classification

The speed code program calculated velocity through use of arc length. The mathematics behind arc length required the calculation in degrees of the location of both the inner and outer wave. The data presented in this section are from the configurations of hydrogen-air detonation trial two. The purpose of presenting hydrogen-air detonations with their degree difference between the inner and outer wave of the detonation, is to

showcase the difference of locations between stable, unstable, and restart waves. Only hydrogen-air detonation data possessed these three classifications. Hydrogen trial two was also the most successful trial of the hydrogen data.

Configuration 1 had the most narrow channel of all the configurations used for hydrogen-air detonations. It was also of the set of configurations with the smallest outer radius. The camera acquisition rate for this configuration was 21,000 fps. Configuration 1 also provided a good example of how leading and lagging events occurred in the curved channel. Figure 83 is a graph of the difference between the outer wave and inner wave for all successful runs of the configuration. Only one successful run was considered unstable while the rest were stable. In general all stable waves exhibited a maximum angular deviation of three degrees between the image frames. The only exception was ER 1.0 with a max change between data points of six degrees. This angular deviation appeared to be an outlier among the data sets. The unstable wave (Φ of 1.9) possessed a degree change of up to five. The general rule for stable waves is the degree difference change was in general only 3 degrees between frames.

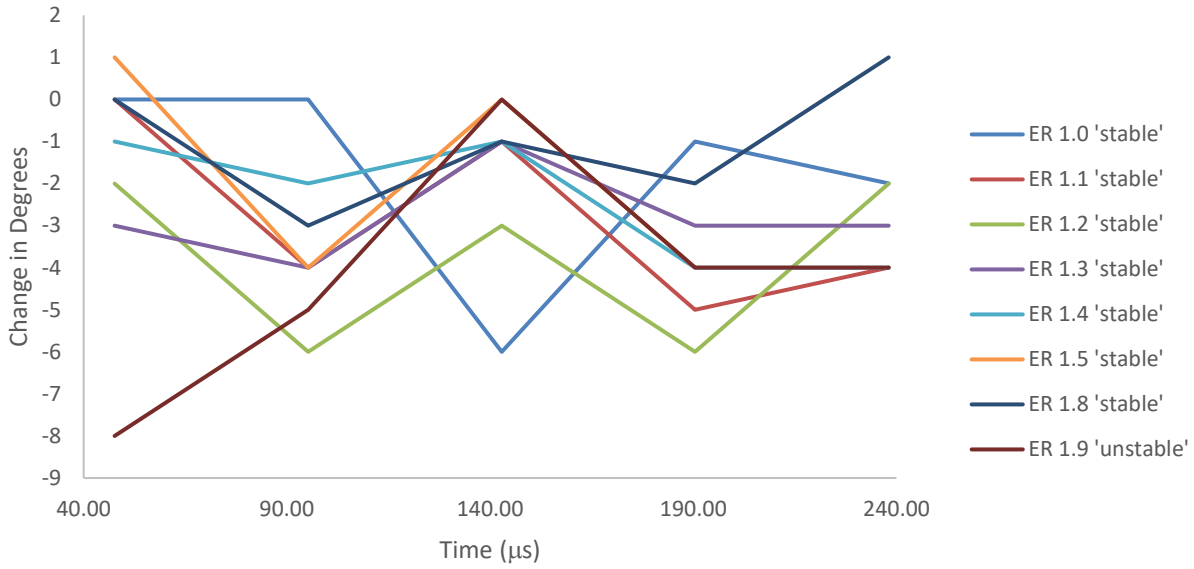

Figure 83. Plot of the degree difference between the outer and inner detonation wave for Configuration 1.

Configuration 2 was part of the set of configurations with the smallest outer radius. It had the second smallest channel width. Configuration 2 possessed a good overall example of how angular difference between inner and outer waves behaved for the unstable cases. Figure 84 is a graph of the difference between the location of the outer and inner wave in degrees compared to time in the curved portion of the test-section. ER of 1.0 was a restart event with a degree difference of three. ER of 1.2 had a max change of degree difference of between time of two. This data set was more of an exception than the rule for a restart event. The rest of the waves had a classification of unstable. The max change of degree difference for this data set were six. ER of 1.8 had a consistent lagging of the inner wave but the change in degree difference of this run was at a max of three.

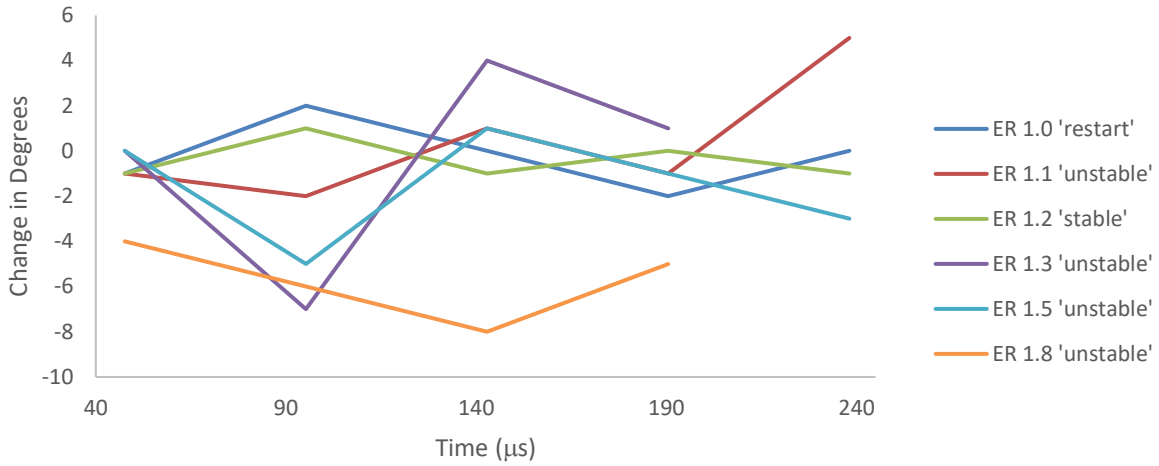

Figure 84. Plot of the degree difference between the outer and inner detonation wave for Configuration 2.

Configuration 7 was of the data set with the largest outer radius. Out of the three configurations, Configuration 7 possessed the narrowest channel width. Channel 7 also possessed good examples of all three different classifications. The camera frame rate of the captured images were 17,000 fps. Equivalence ratios of 1.0, 1.1, and 1.3 were deemed stable. The angular difference in degrees between frames only changed by, at most, two degrees. The case with $\Phi = 0.8$ was classified as unstable. Here the angular difference between frames changed at a max of 5 degrees. The case with $\Phi = 1.9$ was classified as a restart. Here the max angular change between frames was seven degrees. Plot of these angular degree difference is in Figure 85.

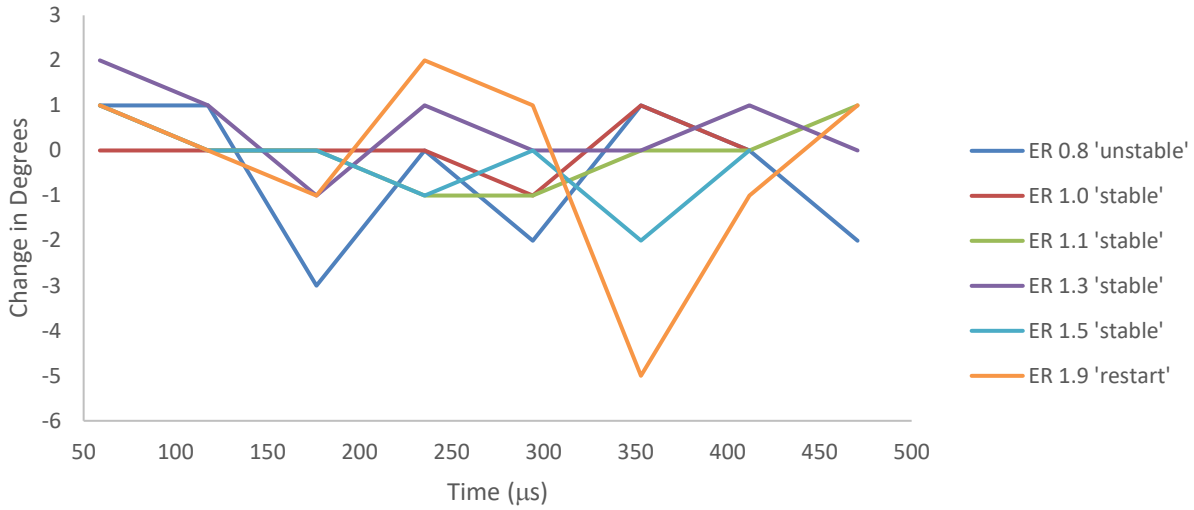

Figure 85. Plot of the degree difference between the outer and inner detonation wave for Configuration 7.

In general. the angular difference between frames of a set is based on wave classification. Stable waves have up to three degrees change between frames (baring the exceptions). Unstable waves have a max of five degrees change between frames. Unstable waves have a max angular difference exceeding five degrees.

4.2.6 Standard Deviation of Velocity Compared to Classification

Using the speed code, the standard deviation of the velocity found in the curved portion for both the inner and outer waves were calculated. This was done for only hydrogen-air detonations, trial one due to the stability of the wave entering and the repeatability of events.

The velocity standard deviations for outer and inner stable waves varied. Configurations 1 and 7 ($R_i/R_o = 0.837$) produced most of the stable wave data. In general,

a stable wave seemed to have standard deviations in both the inner and outer velocity of less than 100 m/s. Table 53 shows all the standard deviations of the velocity in the curved section for both the inner and outer wave.

Table 53. Standard deviation for both the outer wave and inner wave velocity measurements in the curved test portion for stable waves.

Configuration	ER	OR STD (m/s)	IR STD (m/s)
1	1	78.6835	195.66
1	1.1	96.3672	89.1367
1	1.2	192.7343	38.008
1	1.3	55.6376	60.096
1	1.4	53.269	38.008
1	1.5	169.9757	117.1486
1	1.8	78.6835	79.4995
2	1.2	96.3672	143.01
5	1.1	58.2114	57.0453
7	1	98.6776	126.1129
7	1.1	43.9545	71.6882
7	1.2	0	97.2982
7	1.3	96.2995	147.1011
7	1.5	98.6776	174.5954

The unstable waves velocity standard deviations had two different break downs. This relates to the different types of unstable wave discussed in Section 4.2.2. The two different break downs is the standard deviation presented in the outer wave. Some unstable waves had stable outer waves but unstable inner wave. Other unstable waves had both inner and outer waves unstable.. These unstable waves typically had a standard deviation above 100 m/s for both waves. The unstable waves presented with a stable outer wave and an unstable inner wave, the standard deviation also showcased these events. For these waves, the outer wave standard deviation was less than 100, while the inner wave velocity standard deviation was higher than 100. Table 54 lists all velocity

standard deviations around curved portion for unstable waves with $R_i/R_o = 0.775$. Table 55 list all velocity standard deviations around curved portion for unstable waves with $R_i/R_o = 0.708$. Larger channel widths ($R_i/R_o = 0.708$) tended to have higher variance in the velocity data.

Table 54. Unstable wave velocity standard deviation across the curved portion of the test-section. This table contains all configurations with an $R_i/R_o = 0.775$.

Configuration	ER	OR STD (m/s)	IR STD (m/s)
2	1.1	32.1224	168.8451
2	1.3	147.2033	361.6186
2	1.4	266.3448	136.3547
2	1.8	250.8839	237.4817
5	1	64.6837	64.6837
5	0.8	193.4623	68.3167
5	1.2	55.1625	355.3703
5	1.3	165.4874	227.8896
5	1.4	95.5442	108.0181
5	1.5	55.1625	213.9078
8	1	136.613	295.3631
8	1.1	105.3075	322.6994
8	1.2	88.5659	231.189
8	1.3	90.0799	300.2725
8	1.4	124.1666	244.84
8	1.9	203.4291	267.3594

Table 55. Unstable wave velocity standard deviation across the curved portion of the test-section. This table contains all configurations with an $R_i/R_o = 0.708$.

Configuration	ER	OR STD (m/s)	IR STD (m/s)
3	0.8	78.6835	141.6385
3	1	115.8189	60.1997
3	1.1	147.2033	68.2601
3	1.2	105.3203	263.3892
3	1.3	210.0274	288.7077
3	1.4	159.8069	158.8667
3	1.5	309.7771	235.3626
3	1.8	210.6406	383.9524
3	1.9	319.2099	141.6385
6	0.7	82.7437	441.3733
6	0.8	33.78	544.5032
6	1	85.0111	268.7294
6	1.1	90.6412	192.4614
6	1.2	39.0058	197.1563
6	1.3	64.6837	343.4321
6	1.5	132.8488	264.3689
6	1.9	101.3399	143.4523
9	1	188.9533	619.76
9	1.1	167.7197	368.1382
9	1.2	148.0164	419.6938
9	1.3	194.5949	249.8299
9	1.4	113.9431	668.4222
9	1.8	102.7069	199.5113

Reignition events had the largest range for their standard deviation in velocity. Generally, the standard deviation was larger in the outer wave than in the inner wave. This is believed to be because the outer wave in general is much faster than the inner wave, allowing a greater range of speed to occur. The inner wave velocity standard deviation varied the same amount compared to the unstable wave. The reason for this large standard deviation is the inner wave still is playing catch up with the outer wave.

Table 56 shows all standard deviation values for the inner and outer wave velocity measurements taken in the curved test section.

Table 56. Reignition standard deviation for both the outer wave and inner wave velocity measurements in the curved test portion.

Configuration	ER	OR STD (m/s)	IR STD (m/s)
2	1	301.3377	166.3352
3	1.8	299.6089	193.7017
6	1.8	252.7862	513.4532
7	1.9	332.4309	274.7091
8	0.8	478.4787	355.4832
8	1.5	430.1258	277.2041
8	1.8	395.737	276.6175
9	1.5	501.2741	495.9882

4.2.7 Regime Diagrams

To create a regime diagram for ethylene-air detonations, cell size was compared to the channel width. Classifications were chosen based on the mean of the trials for the given ER. Equivalence ratio was then converted to cell sizes based on values pulled from the Cal Tech [23,24,25]data base. For the graph to be formed, only ER of 1.1 and above were charted. The reason for this limit at ER = 1.1 was that 1.1 coincides with the smallest cell size and because ERs below 1.1 usually resulted in wave dissipation. Figure 86 is the graph of the R_i over cell size compared to the channel width. No regime can be charted in the graph. This is believed to be caused by the R_i/R_o ratio equaling 0.8 for all ethylene-air configurations.

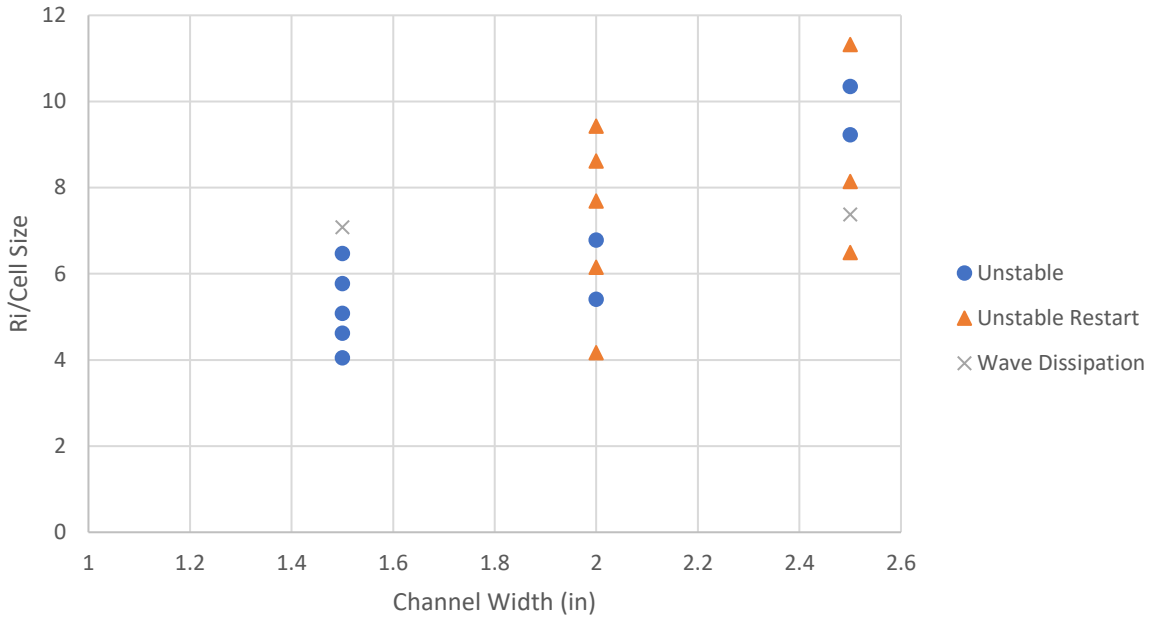

Figure 86. Ethylene-air detonation regime diagram for ERs above 1.1.

Trial 2 data of the hydrogen-air detonation was chosen to create a regime diagram. For hydrogen diagrams, cell size calculations were done for the ERs of one and above. It is obvious from the data that the $R_i/R_o = 0.837$ produced most of the stable events (Configuration 1 and 7, indicating a specific ratio for the radii. The curious case to this is that Configuration 4 only produced wave dissipation classifications. To further break down the regimes, two charts were created. The first regime created was to map the successful detonations versus the unsuccessful ones. The successful ones were classified as stable, unstable, and restart. The unsuccessful ones were classified as wave dissipations, also known as wave dissipation. Figure 87 is the regime for successful and unsuccessful waves. The figure was created by comparing the channel width to the cell size. Unsuccessful waves have a small channel width and in comparison, a large cell size.

The largest ratio for a successful wave appeared to be 0.5 in cell size to a 2-in channel width. Anything with the ratio above this appeared to be an unsuccessful wave.

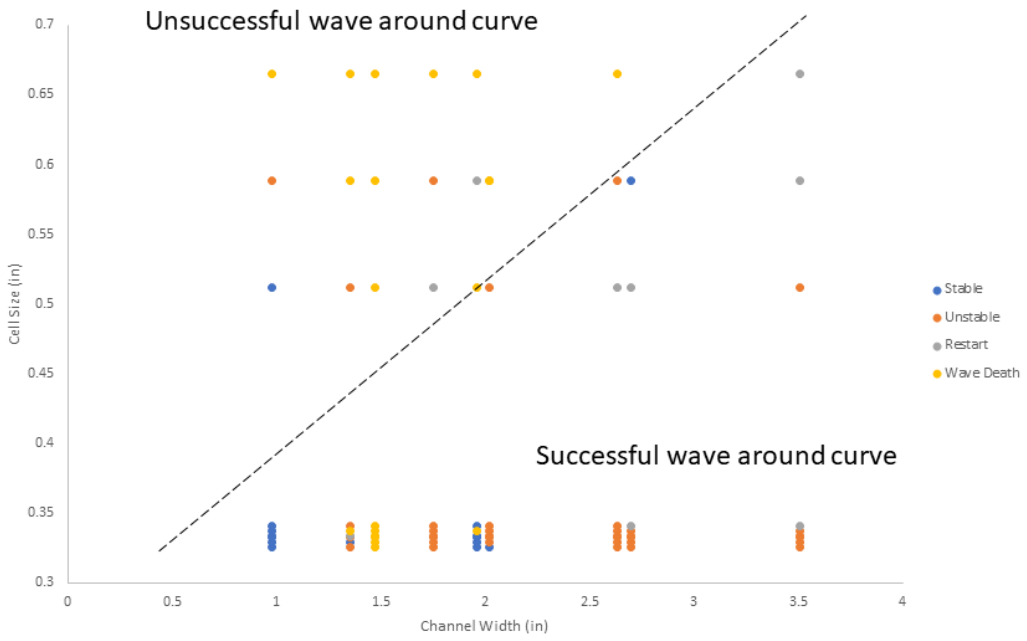

Figure 87. Regime diagram for successful wave around curve.

The second regime diagram created shows the regime for stable and unstable waves. Unstable waves in this case had the classification of unstable and restart classification. Table 54 is the regime diagram for this classification. The regime was created by comparing the R_i/cell size to the channel width for all runs with an ER of one and above. From the diagram, it appeared that the larger the R_i/cell size is compared to the channel width, the more likely the wave is to be stable. The slope for an unstable wave appears to be 10*R_i/cell size to a one channel width for unstable wave. Anything above this line falls into the stable regime.

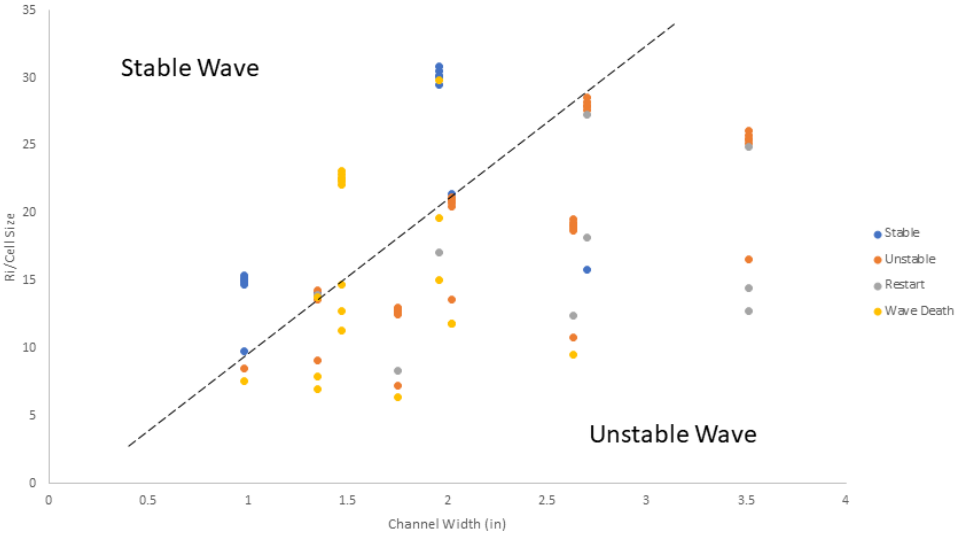

Figure 88. Regime diagram for stable and unstable waves.

V. Conclusions and Recommendations

5.1 Overview

This chapter summarizes the research performed on detonation stability. Section 5.2 talks about the conclusions made throughout the experiment. Section 5.3 talks about how this research pertains to rotating detonation engines (RDE) and why it is important. Section 5.4 gives an overview of future work for continuing on this research.

5.2. Research Conclusions

The strategy of this study was to apply image processing techniques to a set of images containing a detonation propagating down a field. The primary data produced from these sets of images were velocity of different regions of the wave. By comparing the wave-front velocity for 2-D detonations of different radius ratios, effect of the

transverse detonation waves was isolated from the effects of overall curvature on detonation stability. Similarly, the effect of overall detonation reactivity was controlled through dilution, and the 2-D wave-structure was compared to variation in velocity. The velocity variability was quantified using the standard deviations of individual measurements to study instabilities of the waves. This strategy was successful in characterizing the velocity of 2-D detonation waves for a range of geometric curvatures and chemical dilutions.

5.2.1. Conclusions for 2-D Channels

This research studied how velocity varied for ethylene-oxygen, hydrogen-oxygen, and mixed-fuel-oxygen detonations diluted with nitrogen or argon. The first part of this research examined the detonation as it passed only through the test region. Ultimately it was determined the detonations were above the CJ velocity and were overdriven. An extension was added to allow more time for the detonation to stabilize before reaching the test region.

Ethylene-oxygen detonations diluted with argon were studied first with the extension. Here the dilution of argon varied from 0-71.4 percent dilution. The velocity standard deviation varied with dilution. The general trend was increasing the argon dilution did not increase the velocity standard deviation.. The exceptions to this trend were observed in the neat ethylene-oxygen detonations where the velocity variance was higher than expected. However, the high velocity variance could be an artifact attributed to the fact that the median filter applied was not circular. The detonation thickness was

calculated as well. A similar trend here was observed, addition of dilution did not affect detonation wave thickness..

Ethylene-oxygen detonations diluted with nitrogen however showed different trends. The amount diluent varied from 0-46.7 percent of nitrogen while the amount of ethylene-oxygen remained constant and in stoichiometric proportion. The standard deviation of the wave's velocity increased as dilution increased. The detonation's thickness also increased with the increase in dilution. Addition of nitrogen dilution tends to increase the cell sizes in ethylene-oxygen detonation. This increase in cell sizes is believed to be correlated to the decrease detonation velocity.

Comparisons can be made between the ethylene-oxygen detonations with their various dilutions. Argon dilution cases had slower velocities compared to their nitrogen counterparts. This was not expected since nitrogen has a higher heat capacity which lowers the chemical reactivity of the reaction. Diatomic nitrogen has mass of about 28 AMU while argon has a mass of 40 AMU. It is suspected that the lower velocity was caused by overall atomic weight of the reaction.

The standard deviations of the wave velocities can be compared between the ethylene-oxygen detonations and their diluents. The detonations diluted with argon velocity did not vary significantly with different levels of dilution. The detonations diluted with nitrogen did vary with the levels of nitrogen. This can be explained by the cells of the detonations. In general detonations diluted with argon have much smaller cells compared to their nitrogen counter parts. It is believed these differences in cells are the reason for the standard deviations of the wave. The cell formation and the variation along the wave front can be observed for the detonations in the images, with the nitrogen

cases having a less defined wave front. Transverse waves of the detonation make the cells occur. When these waves hit each other, they speed the detonation up. When collisions do not occur, the wave in these places slow down. Since argon has smaller cells, the transverse waves are continually colliding with one another, keeping the wave front defined. With nitrogen, there are bigger areas where collisions do not occur, allowing the wave to lag or speed up. This is believed to be the case of why nitrogen has a greater variation in their detonation speed.

Detonations are a combustion wave coupled with a shockwave. The detonation thickness is the average distance between these two waves. The test were also ran to the point where max dilution before turning into deflagration (or decoupling of the shockwave). The average thickness of the detonation diluted with argon did not change with the percentage of dilution. The average thickness of an ethylene-oxygen detonation diluted with nitrogen increased exponentially with the increase in dilution. This difference is accredited to the difference in heat capacity with nitrogen having about twice the heat capacity as argon.

Hydrogen-oxygen detonations diluted with nitrogen showed similar trends as the ethylene-oxygen detonations diluted with nitrogen. The amount of diluent varied from 0-45.5 percent dilution of nitrogen. The amount of oxygen and hydrogen were held constant at a stoichiometric amount. Like the ethylene-oxygen detonations, the wave velocity of hydrogen-oxygen detonations increased in variability as diluent increased. The detonation wave thickness also increased as the amount of diluent increased.

Hydrogen-oxygen detonations diluted with nitrogen can be compared to the ethylene-oxygen detonations diluted with nitrogen. Hydrogen-oxygen detonations when compared to the same dilution level as the ethylene-oxygen detonations, were more chemically reactive, and had higher velocities. Hydrogen at the same percentage of dilution of ethylene, had larger wave thickness. This is believed to be caused by the heat of combustion between hydrogen and ethylene. Hydrogen as a fuel is a diatomic molecule with one single bond. When the bond is broken, heat is released. Ethylene contains four hydrogen to carbon bons, and one carbon to carbon bonds. In general hydrogen bonds release less heath, then the hydrogen to carbon or carbon to carbon bonds. Ethylene having stronger and more complex bonds release more heat into the detonation. This theory also agrees with why nitrogen dilution increases the detonation wave thickness, with the addition of more heat going into the detonation and not into the molecules themselves. Overall, the conclusion can be made that the detonation thickness is a function of heat released in the detonation process.

For the mixed-fuel blends, the amount of diluent did not vary much but the amount of hydrogen moles did. It was found that the amount of hydrogen had an effect on how fast the detonation propagated. The fuel with the most hydrogen content tended to have a higher velocity overall, as expected. This is attributed to the fact that hydrogen-oxygen detonations tend to have higher CJ points compared to ethylene-oxygen. The detonation thickness for the mixed-fuels did not vary enough to draw conclusions on how hydrogen percentage changes the detonation thickness. However, when comparing detonation thickness of the mixed fuel with their non-mixed counterparts, the mixed fuels with similar levels of dilution to the non-mixed fuels had smaller cells. This is believed to

be caused by the complexity of the mixed fuels. Cell sizes were calculated for the mixed-fuel blends.

Overall wave stability was studied by finding the velocity of the detonation wave across five regions and taking the standard deviation of these velocities in each region. Hydrogen-oxygen and ethylene-oxygen detonations with nitrogen dilution had more variance in their velocities as dilution increased. The same cannot be said about the ethylene-oxygen detonations in argon. Dilution causes increased detonation cell size. Detonations diluted with nitrogen cell size increases rapidly while detonations diluted with argon do increase but at a much slower rate. This variance in velocity is likewise attributed to the increased cell size with increases in diluent. Ethylene-oxygen detonations were observed to have higher velocity variability when diluted with nitrogen compared to argon on a molar basis. This same effect is observed in the increase in cell size for nitrogen dilution compared to argon. This is attributed to the size of the cells, with nitrogen having much larger cells. Ethylene-oxygen detonations speeds were compared to their dilution's levels of nitrogen and argon. It was found that the detonations diluted with argon had less chemical reactivity (slower velocities) than those diluted with nitrogen. This is believed to be caused by the molar mass of diatomic nitrogen being about two-thirds the weight of argon. The wave thickness ethylene-oxygen detonation diluted with nitrogen. was thicker than the ethylene-oxygen detonation diluted with argon. This effect can be attributed to the higher molar heat capacity of nitrogen compared to that of argon. Hydrogen-oxygen detonations diluted with nitrogen had larger detonation wave thickness than the ethylene-oxygen detonations. This can be attributed to hydrogen having a much smaller heat of combustion than ethylene.

5.2.2 Conclusion for Horseshoe Detonations

This research examined the instability of an oblique detonation wave. Ethylene or hydrogen were used as fuels, and the equivalence ratio (Φ) varied throughout the runs. All detonations were open to the atmosphere and used air as the oxidizer.

The first study examined unstable ethylene-air detonations. All waves in this study were found to be unstable. Contributing to this instability, the ethylene-air detonations were observed to be unstable in the first straight-away portion of the horseshoe prior to the curve. All detonation waves in the first straight-away were either overdriven or underdriven, creating the instability. Three different wave classifications were made; unstable, unstable outer wave restart, and unstable inner wave restart.

The unstable classification was denoted by the leading and lagging of the inner and outer wave. The outer wave restart was denoted as what appeared a dissipating wave, and then rapidly igniting the detonation. It was marked with a sharp increase in velocity and the outer wave appearing to propagate across the channel, engulf the entire channel and continuing to propagate normally. The retonation was examined in the image set and also found in the polar meshes. The inner wave restart was very similar to the outer wave, with instead the inner wave restarting and having the retonation as well.

Multiple simultaneous detonation waves have been observed in RDEs, and these multiple waves can be moving in both directions (counterclockwise and clockwise) in the same combustion chamber. These retonation events may help explain why this phenomenon occurs and link it to the stability of the detonation wave with other counter propagating or clapping RDE modes.

The cell size of the ethylene-air detonations were calculated and compared to R_i/cell size. A stability regime could not be created for the ethylene-air detonations. This was believed to be caused by the R_i/R_o being held constant throughout the ethylene configurations at 0.8.

The second study was completed using hydrogen-air detonations. Stable waves were found in this data set with the wave classifications being, stable, unstable, and outer wave restart. Stable waves were classified by having a defined detonation front throughout the run. Unstable waves were denoted as having leading and lagging inner and outer waves. The outer wave reignitions were similar to those observed in the ethylene-air detonations, but exhibited a shorter duration - the outer wave restarts, if present, were for about 100 μs. Ethylene-air detonations were measured to be at a minimum of 350 μs. The difference in the wave back up event is believed to be caused by the complexity of the fuels. Ethylene is much more complex than hydrogen and has multiple radicals and recombination's that can occur when broken. It is believed these left over products become reactants for the backwards propagating wave.

For these hydrogen data sets, all detonation waves in the first straight away were considered stable. All of the detonation waves were within the error of the velocity code when compared to their CJ velocities. Stable waves were found to have outer wave velocities slightly above CJ point and inner waves slightly below CJ point when propagating around the curve. There were two types of unstable waves. The first type of unstable wave had a very stable outer wave, while the inner wave velocity varied significantly around the curved portion. The other type of unstable wave had both the

inner wave and outer wave velocities varying greatly around the curve. The outer wave restart was marked by both the inner wave and outer wave velocity greatly decrease, then sudden increase in the outer wave, followed by a sudden increase in the inner wave.

Angular differences between the inner and outer wave were compared for the hydrogen-air detonations. It was found that stable waves possessed up to three angular degree difference between the inner and outer wave per frame. The unstable waves max angular difference were found to be up to five degrees between frames. The unstable reignitions max angular difference exceeded five degrees.

The angular difference and the standard deviation of velocity suggests a restart event occurs when a detonation is dissipation and then it rapidly ignites itself. It is theorized that a transverse wave hits the outer wave to start the process of re-ignition. A failed detonation wave, the transverse wave either does not occur or does not hit the outer wave to propel the wave forward.

This study also looked into the hydrogen-air detonations standard deviations of velocity. Hydrogen-air detonations were examined in this area over the ethylene-air detonations because to the presence of stable waves. In general, stable waves had a standard deviation of below 100 m/s in the outer wave. The inner wave varied more, but in general a stable wave also had a standard deviation of 100 m/s or less in the inner wave. Only 5 out of 14 stable inner wave velocities were found to be above 100 m/s standard deviation. For an unstable wave, there were two distributions of the wave here when compared to standard deviation. One distribution was a stable outer velocity and an unstable inner velocity. An unstable inner velocity was categorized by having above 100 m/s standard deviation. The other type of unstable wave had both waves varying greater

than 100 m/s std for the most part. The outer wave restart possessed much higher standard deviations in both the inner and outer velocities. All restart events had a standard deviation greater than 250 m/s in either the inner or outer velocity.

Max velocities were examined for the hydrogen-air unstable and restart event waves. The max velocities did not vary much with the two classes. In fact unstable waves tended to have slightly higher max velocities than the unstable waves. It seems the higher max velocities had more to do with channel width. Configuration 8 and 9 unstable waves had the highest max velocities. This contrasts what is found for the standard deviation of the waves. Restart classification inner and outer waves can vary up to 25% of their CJ point value, while unstable outer waves vary up to 15% their CJ value. This suggests (and can be examined in the velocity data) that restart events variation comes from the wave gradually slowing down.

The angular difference and the standard deviation of velocity suggests a restart event occurs when a detonation is dying and then it rapidly ignites itself. It is theorized that a transverse wave hits the outer wave to start the process of re-ignition. After re-ignition, the wave attempts to stabilize itself but is still an unstable wave. An actual dying wave the transverse wave either does not occur or does not hit the outer wave to propel the wave forward.

These unstable events would not be ideal for occurrence in an RDE. The whole purpose of an RDE over a PDE is to increase the stability of the combustion process so the turbomachinery is not damaged and the detonation does not fail. These unstable waves could possibly cause problems down the line for an engine.

It was found that the ratio R_i/R_o of 0.837 produced most of the stable events. Two regimes were observed from the hydrogen-air detonations. The first regime had a successful detonation circulate around the curve. The largest ratio to be considered a success appeared to be a 0.5-in cell to a 2-in channel. Anything above this ratio appeared to cause wave failure. This ratio correlates to having four cells in the channel at a given time. A second regime was found depicted when a stable or unstable wave would occur. The slope of this line appeared to be $10R_i$/cell size to the channel width. Anything above this line fell into the stable regime and anything below this line fell into the unstable regime. This suggests smaller cells are more likely to produce stable wave. This suggestion contradicts successful detonation propagation across the curve. To produce a stable wave, the determining factor is the number of cells and how large the inner radius is. For a stable wave, small cell widths and large inner curvatures are preferred.

5.3 Importance of this Research

This research provides more understanding of the fundamentals of how detonations propagate. These fundamentals are vital to other concepts of detonation combustion engines in the form of rotating detonation engines (RDE).

5.3.1 Importance of 2-D channels

The importance of the 2-D channel is studying how detonations propagate while constricted to a 2-D plane. By constricting the detonation to the 2-D plane, it forces the detonation to move in an expected manner and remove averaging error from the imaging

device. This research further studies how detonation stability and chemical reactivity were affected by the addition of dilution. This concept is important for RDE air-breathing applications because the addition of air contains the diluent nitrogen. The diluents used for this research were argon and nitrogen, with nitrogen pertaining more to the air-breathing applications. In this study it was proven that the addition of nitrogen decreases the stability of the wave and increases the detonation thickness.

It was found that larger cells produce more variance along the detonation wave front and ultimately effecting the variance of the detonation velocity. Argon was found to have less variance in the detonation velocity, but this is attributed to argon having much smaller cells than nitrogen. Wave thickness was calculated and compared for the ethylene-oxygen dilutions. It was found dilution with argon did not affect detonation thickness, but dilution with nitrogen did. This is believed to be caused by nitrogen having about twice the specific heat value than argon. Hydrogen-oxygen diluted with nitrogen detonation thickness was compared to the ethylene-oxygen diluted with nitrogen. It was found that hydrogen-oxygen detonations were not as thick as the ethylene-oxygen when diluted with nitrogen. This was believed to be caused by the heat of formation of the two compounds. Ethylene has a much higher heat of formation, taking more energy to completely break down the compound.

Detonations are combustion waves coupled with a shock wave. It is believed the detonation thickness is a link between the distance between the two. With detonation thickness being linked to heat absorbance, it is suggested that decoupling occurs when there’s too much heat absorbed to keep the two waves coupled.

5.3.2 Importance of Horseshoe Detonations

The horseshoe detonation provides fundamental understanding of how a detonation propagates around a curve. It helps isolate the different types of instability that can be exhibited once a detonation becomes oblique. The application for this is to further the research of RDEs since RDEs themselves inherently have oblique detonations waves circulating around the annulus. A regime diagram for hydrogen-air detonations was produced to further aid the construction and design of RDEs.

This research helps to explain why multiple detonations in an RDE can occur and why they can move in the opposite direction of each other. The theory behind this is a second detonation wave happened because of one of these wave restarts. It also helps explain the galloping behavior of a detonation in an RDE. The theory for this is the detonation is in the unstable category of waves.

This research also helps define stable and unstable waves found in RDEs. It goes so far to classify these waves based on the standard deviations of the velocity and their angular differences. A regime diagram was created to aid with the development of RDEs based on predicted cell sizes found in the detonations.

A regime of operation was created for hydrogen-air detonations. The regime shows that producing a stable wave is a balancing act of the number of cells that can fit in the channel. For the detonation to propagate across the channel, the channel needs four or more cells. Stable waves want the smallest possible cell that can occur. This information pertaining to stability will help the future of RDE research and construction.

5.4 Future work

This section describes the possible future work for the detonations in the 2-D channels and the horseshoe channels.

5.4.1 Future Work for 2-D Channel

There are multiple different directions the work for the 2-D channels can take. Further work of the current setup can be done with imaging shadowgraph and Schlieren at 10 MHz. Work can also be done on perfecting the optical soot foil algorithm either through shadowgraph at 10 MHz or developing a new one of chemiluminescence intensity-time average. Blob tracking of the transverse waves could also possibly be done using chemiluminescence. More work can also be done with the study of mixed fuel detonations. Also work can be done utilizing two Shimadzus as well.

Another option for future work of these channels is to move the test-section to a detonation tube capable of running air. Here the study can be repeated but with air as the diluent. Also further work of mixed-fuel blends can be done as well. This study would be more pertinent to the air-breathing applications of RDE.

5.4.2 Future Work for Horseshoe Detonations

Future work for the Horseshoe detonations is to run the same configurations of the hydrogen-air detonations but using stable ethylene-air detonations in the first straight-aways. This would further the knowledge of how ethylene-air detonations propagate around a curve and may shed light on stability regimes.

Appendix A. Detonation Velocity Code Example

```
% Full Run of the Camera_14_02_13_analysis V5

%Updates
% V2 runs from reading from file
% V3 New function to only have detonation wave in the binary image
% V4 includes background subtraction
% V5 Code bug found in im2 sob function not background subtraction

%Requirements
% Image Processing Toolbox
% Sobel Function Code
% detwavefind Function Code
clc
clear
%% Constants

fps=5e6;
resolution=33.75;      % pixels/mm
filtsize=5;
sobthresh=0.10;
numregion=5;        %currently hardcoded
area=500;


photo_start=66;
photo_end=75;

% Reading files in


files=dir(fullfile('Camera_14_02_13', '*.tiff'));
totalfiles=numel(files);

basefilename=files(1).name;
fullfilename=fullfile(files(1).folder,basefilename);
background1=imread(fullfilename);

basefilename=files(2).name;
fullfilename=fullfile(files(2).folder,basefilename);
background2=imread(fullfilename);

basefilename=files(3).name;
fullfilename=fullfile(files(3).folder,basefilename);
```

```
background3=imread(fullfilename);

basefilename=files(4).name;
fullfilename=fullfile(files(4).folder,basefilename);
background4=imread(fullfilename);

backgroundavg=(double(background1)+double(background2)+double(backgroun
d3)+double(background4))./4;


sootfoil=zeros(250,400);
ii=0;

for k=photo_start+1:1:photo_end

   ii=1+ii;

   basefilename=files(k-1).name;
   fullfilename=fullfile(files(k-1).folder,basefilename);
   im1=imread(fullfilename);

   basefilename=files(k).name;
   fullfilename=fullfile(files(k).folder,basefilename);
   im2=imread(fullfilename);

   lengthy=size(im1,1);
   lengthx=size(im1,2);

   im1backsub=double(im1)-backgroundavg;
   im1sob=Sobel(im1backsub);
   im1sob=im1sob>sobthresh*max(max(im1sob));
   im1med=medfilt2(im1sob, [filtsize filtsize]);
   im1det=detwavefind(im1med, area);

   im2backsub=double(im2)-backgroundavg;
   im2sob=Sobel(im2backsub);
   im2sob=im2sob>sobthresh*max(max(im2sob));
   im2med=medfilt2(im2sob, [filtsize filtsize]);
   im2det=detwavefind(im2med, area);

   for i=1:lengthx
      for j=1:lengthy
         if im1det(j,i)==1;
            detloc1(i)=j;
         end
```

```
   end
end

for i=1:lengthx
   for j=1:lengthy
      if im2det(j,i)==1;
         detloc2(i)=j;
      end
   end
end

%section of calculating the speed
reg1_1=detloc1(3:80)';
reg1_2=detloc1(81:160)';
reg1_3=detloc1(161:240)';
reg1_4=detloc1(241:320)';
reg1_5=detloc1(321:398)';

reg2_1=detloc2(3:80)';
reg2_2=detloc2(81:160)';
reg2_3=detloc2(161:240)';
reg2_4=detloc2(241:320)';
reg2_5=detloc2(321:398)';

speed1(ii)=(mean(reg2_1)-mean(reg1_1))*fps*1/resolution/1000;
speed2(ii)=(mean(reg2_2)-mean(reg1_2))*fps*1/resolution/1000;
speed3(ii)=(mean(reg2_3)-mean(reg1_3))*fps*1/resolution/1000;
speed4(ii)=(mean(reg2_4)-mean(reg1_4))*fps*1/resolution/1000;
speed5(ii)=(mean(reg2_5)-mean(reg1_5))*fps*1/resolution/1000;

% calculating the soot foil

locmin1=islocalmin(detloc1, 'MinProminence',2);
locmin2=islocalmin(detloc2, 'MinProminence',2);

for i=1:lengthx-2
   if locmin1(i)==1;
      sootfoil(detloc1(i), i)=1;
   end
end

for i=1:lengthx-2
   if locmin2(i)==1;
      sootfoil(detloc2(i), i)=1;
   end
```

```
    end

end

time=(1:1:size(speed1,2))./fps*1e6;
speedmean=(speed1+speed2+speed3+speed4+speed5)/5;

RegionMeans=[mean(speed1);mean(speed2); mean(speed3); mean(speed4);
mean(speed5)]

RegionSTDS=[std(speed1);std(speed2); std(speed3); std(speed4); std(speed5)]

figure(1)
plot(time,speed1)
hold on
plot(time,speed2)
plot(time, speed3)
plot(time, speed4)
plot(time, speed5)
plot(time, speedmean, '--')

xlabel('time \mus')
ylabel('meters per second')

legend('Region 1', 'Region 2', 'Region 3', 'Region 4', 'Region 5', 'Mean')

xlim([min(time) max(time)])

ylim([0.75*mean(speedmean) 1.5*mean(speedmean)])

figure(2)
imagesc(sootfoil)
```

Appendix B. Detonation Thickness Code Example

```
% Full Run of the 13_43_05_soot_thick_v2

% Purpose of code is to calculate the soot foils and the thickness of the
% detonation waves. Copy and paste with some edits of the velocity data.

%Updates
% v2 different median filters for soot foil and thickness
```

```
%Requirements
% Image Processing Toolbox
% Sobel Function Code
% detwavefind Function Code
clc
clear
%% Constants

fps=5e6;
resolution=33.75;      % pixels/mm
filtsize=15;           % filter for thickness detection
filtsize2=5;           % Filter for soot foil formation
sobthresh=0.10;
numregion=5;        %currently hardcoded
area=500;


photo_start=87;
photo_end=105;

% Reading files in


files=dir(fullfile('Camera_13_43_05', '*.tiff'));
totalfiles=numel(files);

basefilename=files(1).name;
fullfilename=fullfile(files(1).folder,basefilename);
background1=imread(fullfilename);

basefilename=files(2).name;
fullfilename=fullfile(files(2).folder,basefilename);
background2=imread(fullfilename);

basefilename=files(3).name;
fullfilename=fullfile(files(3).folder,basefilename);
background3=imread(fullfilename);

basefilename=files(4).name;
fullfilename=fullfile(files(4).folder,basefilename);
background4=imread(fullfilename);

backgroundavg=(double(background1)+double(background2)+double(background3)+do
uble(background4))./4;
```

```
sootfoil=zeros(250,400);
ii=0;

for k=photo_start+1:1:photo_end

   ii=1+ii;

   basefilename=files(k-1).name;
   fullfilename=fullfile(files(k-1).folder,basefilename);
   im1=imread(fullfilename);

   basefilename=files(k).name;
   fullfilename=fullfile(files(k).folder,basefilename);
   im2=imread(fullfilename);

   lengthy=size(im1,1);
   lengthx=size(im1,2);

   % wave thickness imagess
   im1backsub=double(im1)-backgroundavg;
   im1sob=Sobel(im1backsub);
   im1sob=im1sob>sobthresh*max(max(im1sob));
   im1med=medfilt2(im1sob, [filtsize filtsize]);
   im1det=detwavefind(im1med, area);

   im2backsub=double(im2)-backgroundavg;
   im2sob=Sobel(im2backsub);
   im2sob=im2sob>sobthresh*max(max(im2sob));
   im2med=medfilt2(im2sob, [filtsize filtsize]);
   im2det=detwavefind(im2med, area);

   % soot foil section
   im2medsoot=medfilt2(im2sob, [filtsize2 filtsize2]);
   im2detsoot=detwavefind(im2medsoot, area);

   % for thickness
   for i=1:lengthx
      for j=1:lengthy
         if im2det(j,i)==1;
            detloc1(i)=j;
            break
         end
      end
```

```
    end

    for i=1:lengthx
        for j=1:lengthy
            if im2det(j,i)==1;
                detloc2(i)=j;
            end
        end
    end

    for i=1:lengthx
        for j=1:lengthy
            if im2detsoot(j,i)==1;
                detloc2soot(i)=j;
            end
        end
    end
    %section for Calculating Thickness

    detthickness=(detloc2-detloc1)./resolution;
    frame_avg_thick(ii)=mean(detthickness);

    % calculating the soot foil

    %locmin1=islocalmin(detloc1, 'MinProminence',2);
    locmin2=islocalmin(detloc2soot, 'MinProminence',2);


    for i=1:lengthx-2
        if locmin2(i)==1;
            sootfoil(detloc2soot(i), i)=1;
        end
    end

end


figure(2)
imagesc(sootfoil)

avg_det_thickness=mean(frame_avg_thick) %in mm
```

Appendix C. Detonation Wave Find Function

```
function y=detwavefind(binaryimage, areathreshold)

% Enter the thresholded image of the detonation wave

labeledImage=bwlabel(binaryimage,8);
blobsmeasurement=regionprops(labeledImage, binaryimage, 'all');
allblobsAreas=[blobsmeasurement.Area];
allowableAreaIndexes=allblobsAreas>areathreshold;
KeeperIndexes=find(allowableAreaIndexes);
Keeperblobsimage=ismember(labeledImage,KeeperIndexes);
y=Keeperblobsimage;
end
```

Appendix D. Sobel Function

```
function y=Sobel(x)

%Input is for an image.


length=size(x);
sobelx=[-1 0 1; -2 0 2; -1 0 1];
sobely=[-1 -2 -1; 0 0 0; 1 2 1];

xpad=padarray(x,[length(1,1) length(1,2)], 0, 'post');
sobelxpad=padarray(sobelx, [2*length(1,1)-3 2*length(1,2)-3], 0, 'post');
sobelypad=padarray(sobely, [2*length(1,1)-3 2*length(1,2)-3], 0, 'post');
xdir=ifft2(fft2(sobelxpad).*fft2(xpad));
ydir=ifft2(fft2(sobelypad).*fft2(xpad));
mag=(xdir.^2+ydir.^2).^(1/2);
y=mag(1:length(1,1), 1:length(1,2));
end
```

Appendix E. Curve Detonation Velocity Code Example

```
% Variables List

% filter          -- Size of Median Filter for calculation of blob
% filter2         -- Size of Median Filter used for actual images for
```

```
%                  speed calcs
% area             -- Size of area to detect wave in pixels
% threshold        -- Value in 16 units to threshold image
% OR               -- Outer Radius in inches
% IR               -- Inner Radius in inches
% fps              -- frames per second
% winsize          -- Window size from positive direction for wave cleanup
% pmeshinnervalue  -- Value must be over of the pixel intensity/max of the
%                  the theta value for inner wave
% pmeshoutervalue  -- Value must be over of the pixel intesity/max
%                  intensity of the theat value for outer wave
% StartStraight1   -- File number for start of Straight Portion 1
% EndStraight1     -- File number for end of Straight Portion 1
% StartCurve       -- File number for start of Curved Portion
% EndCurved        -- File number for end of Curved Portion
% StartCurvedAn    -- File number, curved analysis (For Debugging)
% EndCurvedAn      -- File number, curved analysis (For Debugging)
% StartStraight2   -- File number for start of Straight Portion 2
% EndStraight2     -- File number for end of Straight Portion 2
% files            -- Name of file to read from
% totalfiles       -- Number of files in folder
% basefilename     -- basefile name
% fullfilesname    -- full directory of the file location
% s                -- number of wave blobs detected
% im2              -- image being read in
% im3              -- image being read in
% im2med           -- im2 with median filtering applie
% im3med           -- im3 with median filtering applied
% z                -- im3med-im2med
% a                -- im3-im2, value for debugging
% loc              -- location of the centroid of the waveblob
% xy               -- location of all wave blobs found in image set
% TaubinFit        -- Output of function CircleFitByTaubin
% orginx           -- x-corrdinate of orgin for circle found by Taubin fit
% orginy           -- y-coordinate of orgin for circle found by Taubin fit
% R                -- Radius found by taubin fit (radius to middle of the
%                  Outer and inner radiuses
% Resolution       -- Resolution of image
% ORpix            -- Outer radius dimension in pixels
% IRpix            -- Inner radius dimension in pixels
% length           -- dimension of the image
% IRloc            -- location of wave front in the inner radius
% ORloc            -- location of wave front in the outer radius
% SpeedIRStraight  -- Speed of inner radius wave in first straight away
% SpeedORStraight  -- Speed of outer radius wave in first straight away
```

```
% pmeshouter        -- Polar mesh for outer radius
% pmeshinner        -- Polar mesh for inner radius
% xcorrplus         -- max coordiante to read image in for x-direction
% xcorrminus        -- min corrdinate to read image in for x-direction
% ycorrplus         -- max coordinate to read image in for y-direction
% ycorrminus        -- min coordinate to read image for in y-direction
% newim             -- image with only wave front in it
% v                 -- new coordinate system for x value
% d                 -- new coordinate system for y value
% c                 -- placeholder
% theta             -- theta value in degrees for the polar mesh
% pmeshouterbinary  -- polar mesh outer radius with binary values only
% pmeshinnerbinary -- polar mesh inner radius with binary values only
% value             -- max value for binary values (1)
% thetaOR           -- location of max values in degrees for OR
% thetaIR           -- location of max values in degrees for IR
% delta             -- change in theta bewteen data points
% arcLIR            -- arclength for the delta for Inner radius
% arcLOR            -- arclength for the delta for OUter radius
% SpeedOR           -- Speed of wave transversing curved outer radius
% SpeedIR           -- Speed of wave transversing curved inner radius
% IRlocend          -- Loc of inner wave front in 2nd straight away
% ORlocend          -- Loc of outer wave front in 2nd straight away
% SpeedIRstraightend -- Speed of inner radius in 2nd straight away
% SpeedORstraightend -- Speed of outer radius in 2nd straight away
% lengthstraight1   -- number of data points of speed in straight away 1
% lengthcurved      -- Number of data points of speed in curved region
% lengthstraight2   -- Number of data points of speed in straight away 2
% SpeedIRtot        -- All speed data points for IR
% SpeedORtot        -- All speed data points for OR
% NonDSpeedIR       -- Non dimensional speed around curved reagion;
%                   dimensionalized with first straight section speed
% NonDSpeedOR       -- Non dimensional speed around curved region;
%                   dimensionalized with first straight section speed
% manualResolution  -- Resolution done manual used for testing.



% variables used for iteration
% i,k, j, l, q

clc
clear
%% Global Variables
% User should change what is need here for global variables
```

```
filter=25;
filter2=5;
area=800;
threshold=4000;
OR=12/2;
IR=9.3/2;
fps=21000;
winsize=450;

channelthird=11; % Currently Automatted.

pmeshoutervalue=0.10;
pmeshinnervalue=0.12; % Changed here was a little too low

manualResolution=15.177; %Currently automated

%% Files Loading
% User should manually change values here for reading in files. Number is
% the number of the file in the folder not the actual frame number.

StartStraight1=6;
EndStraight1=8;

StartCurved=9;
EndCurved=12;
StartCurvedAn=9;
EndCurvedAn=12;

StartStraight2=13;
EndStraight2=15;


files=dir(fullfile('12_21_2020_1525', '*.tif'));
totalfiles=numel(files);

%% Reading all circular files to apply the Taubin fit to it

i=0;
for k=StartCurved:1:EndCurved

   i=1+i;

   basefilename=files(k-1).name;
   fullfilename=fullfile(files(k-1).folder,basefilename);
```

```
    im2=imread(fullfilename);

    basefilename=files(k).name;
    fullfilename=fullfile(files(k).folder,basefilename);
    im3=imread(fullfilename);

    im2med=medfilt2(im2, [filter filter]);
    im3med=medfilt2(im3, [filter filter]);

    loc=stwaveblob(im3med-im2med, threshold, area);

    s=size(loc(1,1));
    if s==1
        xy(i,1)=loc(1,1);
        xy(i,2)=loc(1,2);
    end

    if s~=1
        xy(i,2)=mean(loc(:,1));
        xy(i,2)=mean(loc(:,2));

    end
end

TaubinFit=CircleFitByTaubin(xy);

orginx=TaubinFit(1,1);
orginy=TaubinFit(1,2);
R=TaubinFit(1,3);

Resolution=R/((OR-IR)/2+IR);

ORpix=Resolution*OR;

IRpix=Resolution*IR;

Channelthird=(OR-IR)*Resolution/3;
%% Calculating first straight-away section

i=0;
for k=StartStraight1:1:EndStraight1

    i=1+i;

    basefilename=files(k).name;
```

```
    fullfilename=fullfile(files(k).folder,basefilename);
    im2=imread(fullfilename);

    length=size(im2);

    im2med=medfilt2(im2, [filter2 filter2]);

    q=0;
    loc=0;
    for x=1:1:length(1,2)
        for y=round(IRpix+orginy):1:round(IRpix+orginy)+12
         if double(im2med(y,x))>threshold
             q=q+1;
             loc(q)=x;
         end
        end
    end
    IRloc(i,:)=min(loc);

    q=0;
    loc=0;
    for x=1:1:length(1,2)
        for y=round(ORpix+orginy)-12:1:round(ORpix+orginy)
        if double(im2(y,x))>threshold
            q=q+1;
            loc(q)=x;
        end
        end
    end
    ORloc(i,:)=min(loc);

end

i=0;
for k=2:1:size(IRloc,1)
    i=i+1;
    SpeedIRstraight(i,:)=(IRloc(k-1,1)-IRloc(k,1))/Resolution*fps*0.0253;
    SpeedORstraight(i,:)=(ORloc(k-1,1)-ORloc(k,1))/Resolution*fps*0.0253;
end

%% Calculating Speed along Curved portion

i=0;
pmeshouter=zeros(360,EndCurvedAn-StartCurvedAn);
pmeshinner=zeros(360,EndCurvedAn-StartCurvedAn);
```

```
for k=StartCurvedAn:1:EndCurvedAn

   i=1+i;

   basefilename=files(k-1).name;
   fullfilename=fullfile(files(k-1).folder,basefilename);
   im2=imread(fullfilename);

   basefilename=files(k).name;
   fullfilename=fullfile(files(k).folder,basefilename);
   im3=imread(fullfilename);

   im2med=medfilt2(im2, [filter2 filter2]);
   im3med=medfilt2(im3, [filter2 filter2]);

   a=im3-im2;
   z=im3med-im2med;

   length=size(z);

   newim=zeros(length(1,1),length(1,2));

%     Applying Wave clean up
  xcorrplus=round(xy(i,1))+winsize;
  xcorrminus=round(xy(i,1))-winsize;
  ycorrplus=round(xy(i,2))+winsize;
  ycorrminus=round(xy(i,2))-winsize;

  if xcorrminus<1
     xcorrminus=1;
     xcorrplus=xcorrplus+winsize;
  end

  if ycorrminus<1
     ycorrminus=1;
     ycorrplus=ycorrplus+winsize;
  end

  if xcorrplus>length(1,2)
     xcorrplus=length(1,2);
  end

  if ycorrplus>length(1,1)
     ycorrplus=length(1,1);
```

```
  end

  for x=xcorrminus:1:xcorrplus
     for y=ycorrminus:1:ycorrplus

     newim(y,x)=z(y,x);
     end
  end

  %newimthresh=newim>threshold;
  %imagesc(newim)
  %axis image
  %pause(0.5)

  %Error is either in v and D or in PolTheta
  for x=1:1:length(1,2)
     for y=1:1:length(1,1)
        v=x-orginx;
        d=orginy-y;
        c=length(1,2)-y-orginy;
        if round(ORpix)>=round((v^2+d^2)^(1/2)) &&
round((v^2+d^2)^(1/2))>=round(ORpix-Channelthird)
           c=length(1,2)-y-orginy;
           theta=round(PolTheta(v,d));
           if double(newim(y,x))>pmeshouter(theta+1)
              pmeshouter(theta+1,i)=double(newim(y,x));
           end
        end
        if round(IRpix+Channelthird)>=round((v^2+d^2)^(1/2)) &&
round((v^2+d^2)^(1/2))>=round(IRpix)
           c=length(1,2)-y-orginy;
           theta=round(PolTheta(v,d));
           if double(newim(y,x))>pmeshinner(theta+1)
              pmeshinner(theta+1,i)=double(newim(y,x));
           end
        end
     end
   end

   pmeshouter(:,i)=pmeshouter(:,i)./max(pmeshouter(:,i));
   pmeshinner(:,i)=pmeshinner(:,i)./max(pmeshinner(:,i));
end

pmeshouterbinary=pmeshouter>pmeshoutervalue;
pmeshinnerbinary=pmeshinner>pmeshinnervalue;
```

```
[value thetaOR]=max(pmeshouterbinary);
thetaOR=thetaOR';

[value thetaIR]=max(pmeshinnerbinary);
thetaIR=thetaIR';

i=0;
for k=2:1:size(thetaIR,1)
   i=i+1;
   delta=thetaOR(k)-thetaOR(k-1);
   arcLOR(i,:)=abs((delta/360)*2*pi*OR);
end

i=0;
for k=2:1:size(thetaIR,1)
   i=i+1;
   delta=thetaIR(k)-thetaIR(k-1);
   arcLIR(i,:)=abs((delta/360)*2*pi*IR);
end

 SpeedOR=arcLOR*fps*0.0253;

 SpeedIR=arcLIR*fps*0.0253;

 %% Calculating speed at second straight portion

 i=0;
for k=StartStraight2:1:EndStraight2

   i=1+i;

   basefilename=files(k).name;
   fullfilename=fullfile(files(k).folder,basefilename);
   im2=imread(fullfilename);

   length=size(im2);

   im2med=medfilt2(im2, [filter filter]);

   q=0;
   loc=0;
   for x=1:1:length(1,2)
      for y=round(orginy-IRpix-Channelthird):1:round(orginy-IRpix)
      if double(im2med(y,x))>threshold
```

```
        q=q+1;
        loc(q)=x;
      end
      end
   end
   IRlocend(i,:)=max(loc);



   q=0;
   loc=0;
   for x=1:1:length(1,2)
      for y=1:1:round(orginy-ORpix)+12
      if double(im2med(y,x))>threshold
        q=q+1;
        loc(q)=x;
      end
      end
   end
   ORlocend(i,:)=max(loc);


end

i=0;
for k=2:1:size(IRlocend,1)
   i=i+1;
   SpeedIRstraightend(i,:)=(IRlocend(k,1)-IRlocend(k-1,1))/Resolution*fps*0.0253;
   SpeedORstraightend(i,:)=(ORlocend(k,1)-ORlocend(k-1,1))/Resolution*fps*0.0253;
end
%% Combining Speeds to plot

lengthstraight1=size(SpeedIRstraight,1);
lengthcurved=size(SpeedIR, 1);
lengthstraight2=size(SpeedIRstraightend,1);

i=0;
for k=1:1:lengthstraight1
   i=i+1;
   SpeedIRtot(i,:)=SpeedIRstraight(k);
   SpeedORtot(i,:)=SpeedORstraight(k);
end

for k=1:1:lengthcurved
   i=i+1;
```

```
   SpeedIRtot(i,:)=SpeedIR(k);
   SpeedORtot(i,:)=SpeedOR(k);
end

for k=1:1:lengthstraight2
   i=i+1;
   SpeedIRtot(i,:)=SpeedIRstraightend(k);
   SpeedORtot(i,:)=SpeedORstraightend(k);
end

for i=1:1:size(SpeedORtot,1)
   time(i)=(i-1)/fps;
end

figure(1)
plot(time.*1e6, SpeedORtot, 'r')
hold on
plot(time.*1e6, SpeedIRtot, 'b')


ylim([0 3500])

xline((lengthstraight1-1)/fps*1e6,'--');
xline((lengthstraight1+lengthcurved-1)/fps*1e6,'--');

ylabel('Speed (m/s)')
xlabel('time (\mus)')
legend('OR', 'IR')

%% Non-Dimensionalizing speed

% Assumption here is OR and IR in straight away are the same speed give or
% take

NonDSpeedOR=SpeedOR/SpeedIRstraight(end);
NonDSpeedIR=SpeedIR/SpeedIRstraight(end);

thetaORnew=thetaOR(2:end);
thetaIRnew=thetaIR(2:end);

figure(2)
plot(thetaORnew,NonDSpeedOR, 'r')
hold on
plot(thetaIRnew,NonDSpeedIR, 'b')
```

```
xlabel('Degrees')
ylabel('D/Dstr')
ylim([0.25 2.0])

yline(0.8, '--');
%yline(0.6,'--');
yline(1.2,'--');
%yline(1.4, '--');
legend('OR', 'IR')

set(gca, 'XDir','reverse')

%% Polar mesh graph

timepolar=time(lengthstraight1:lengthstraight1+lengthcurved).*1e6;

figure(3)
imagesc(timepolar, [1:1:360], pmeshouter)

xlabel('time (\mus)')
ylabel('Degrees')

figure(4)

imagesc(timepolar, [1:1:360], pmeshinner)

xlabel('time (\mus)')
ylabel('Degrees')
%% Output for xcel sheet
SpeedORmean=mean(SpeedOR)

SpeedORMax=max(SpeedOR)

SpeedIRmean=mean(SpeedIR)

SpeedIRstraight
```

Appendix F. Detonation Wave Tracking Function

```
function y=stwaveblob(x,threshold,area)

% Function is to determine locations of the leading transverse waves.
% The required inputs are the threshold you want for the image and the area
% of the blob itself. Threshold is intensity and area is area in pixels
% Version 1.2
length=size(x);

threshx=zeros(length(1,1),length(1,2));
for i=1:length(1,1)
   for j=1:length(1,2)
         if x(i,j)>threshold
            threshx(i,j)=x(i,j); %det75avg(i,j);
         end
   end

end

%threshvalue=4700;
binaryimage=threshx>threshold;
binaryimage=imfill(binaryimage, 'holes');
labeledimage=bwlabel(binaryimage);

blobmeasurements=regionprops(labeledimage, threshx,'all');
numberofblobs=size(blobmeasurements,1);

allblobsarea=[blobmeasurements.Area];

allBlobCentroids = [blobmeasurements.Centroid];
centroidsX = allBlobCentroids(1:2:end-1);
centroidsY = allBlobCentroids(2:2:end);

i=0; %this i is just a count for the for loop below

for k=1:numberofblobs
   if allblobsarea(k)>area
      i=i+1;
      centers(i,1)=centroidsX(k);
      centers(i,2)=centroidsY(k);
   end
end
centerscopy=[];
centerscopy(1,:)=centers(1,:);
```

```
i=1;
for k=2:size(centers)
   z=centers(1,1)-centers(k,1);
   v=centers(1,2)-centers(k,2); %added line
   if abs(z)<50 & abs(v)<50    %added and sign
      i=i+1;
      centerscopy(i,:)=centers(k,:);
   end
end

y=centerscopy;
end
```

Appendix G. Calculation of θ Function

```
function degree=PolTheta(x,y)

if x>0 && y>0
   z=atand(y/x);
end

if x>0 && y<0
  z=360+atand(y/x);
end

if x<0 && y>0
   z=180+atand(y/x);
end

if x<0 && y<0
  z=180+atand(y/x);
end

if x==0 && y>0
   z=90;
end

if x==0 && y<0
   z=180;
end
```

```
if y==0 && x>0
   z=0;
end

if y==0 && x<0
   z=180;
end

if y==0 && x==0
   z=0;
end

degree=z;
end
```

Bibliography

[1] Grc.nasa.gov. 2020. *Schlieren Flow Visualization*. [online] Available at: <https://www.grc.nasa.gov/www/k-12/airplane/tunvschlrn.html> [Accessed 15 September 2020].

[2] R. K. Hanson, J. M. Seitzman, and P. H. Paul, "Planar laser-fluorescence imaging of combustion gases," *Appl. Phys. B Photophysics Laser Chem.*, vol. 50, no. 6, pp. 441–454, 1990, doi: 10.1007/BF00408770.

[3] Goodman, J. (2019). *Introduction to Fourier Optics*. 3rd ed. Greenwood Village: Roberts & Company Publishers.

[4] Gonzalez, R. C., and Woods, R. E., *Digital Image Processing*, 3nd ed., PearsonEducation, Inc, Upper Saddle River, New Jersey, 2008, Chaps. 3, 4.

[5] Taubin, Gabriel, "Estimation of Planar Curves, Surfaces, and Nonplanar Space Curves Defined by Implicit Equations with Applications to Edge and Range Image Segmentation

[6] J. W. Bennewitz, B. R. Bigler, W. A. Hargus, S. A. Danczyk, and R. D. Smith, "Characterization of detonation wave propagation in a rotating detonation rocket engine using direct high-speed imaging," *2018 Jt. Propuls. Conf.*, pp. 1–22, 2018, doi: 10.2514/6.2018-4688.

[7] Smith, R. D. and Stanley, S. B., "Experimental investigation of continuous detonation rocket engines for in-space propulsion," *52nd AIAA/SAE/ASEE Jt. Propuls. Conf. 2016*, pp. 1–13, 2016, doi: 10.2514/6.2016-4582.

[8] Chacon, F., and Gamba, M. "Oh Plif Visualization of an Optically Accessible Rotating Detonation Combustor." *AIAA Propulsion and Energy Forum and Exposition, 2019*, No. August, 2019. https://doi.org/10.2514/6.2019-4217.

[9] Cho, K. Y., Codoni, J. R., Rankin, B. A., Hoke, J. L., and Schauer, F. R. "High-Repetition-Rate Chemiluminescence Imaging of a Rotating Detonation Engine." *54th AIAA Aerospace Sciences Meeting*, Vol. 0, No. January, 2016, pp. 1–14. https://doi.org/10.2514/6.2016-1648.

[10] Burr, J. R., and Yu, K. "Detonation Wave Propagation in Cross-Flow of Discretely Spaced Reactant Jets." No. July, 2017, pp. 1–8. https://doi.org/10.2514/6.2017-4908.

[11] Sosa, J., Ahmed, K. A., Fievisonh, R., Hoke, J., Ombrello, T., and Schauer, F. "Experimental Investigation of Detonation Wave Propagation in a Supersonic Crossflow." *AIAA Aerospace Sciences Meeting, 2018*, No. 210059, 2018, pp. 1–15. https://doi.org/10.2514/6.2018-0156.

[12] Chambers, J. M., Ahmed, K. A., Stevens, C. A., Hoke, J., and Schauer, F. R. "Turbulent Detonation Transition in a Linearized Rotating Detonation Engine." *AIAA Aerospace Sciences Meeting, 2018*, No. 210059, 2018, pp. 1–6. https://doi.org/10.2514/6.2018-1416.

[13] Fugger, C. A., Cho, K. Y., Hoke, J., Gomez Gomez, M., Meyer, T. R., Schumaker, S. A., and Caswell, A. W. "Detonation Dynamics Visualization From Megahertz Imaging." No. January, 2020, pp. 1–13. https://doi.org/10.2514/6.2020-0441.

[14] S. I. Jackson, J. M. Austin, and J. E. Shepherd, "Planar detonation wave initiation in large-aspect-ratio channels," *AIAA J.*, vol. 44, no. 10, pp. 2422–2425, 2006, doi: 10.2514/1.21581.

[15] J. M. Austin, F. Pintgen, and J. E. Shepherd, "Lead shock oscillation and decoupling in propagating detonations," *43rd AIAA Aerosp. Sci. Meet. Exhib. - Meet. Pap.*, no. January, pp. 4459–4463, 2005, doi: 10.2514/6.2005-1170.

[16] M. D. Frederick, R. Gejji, J. E. Shepherd, and C. D. Slabaugh, "Preliminary results from narrow channel facility experiments at purdue university," *AIAA Propuls. Energy Forum Expo. 2019*, no. August, pp. 1–8, 2019, doi: 10.2514/6.2019-4218.

[17] Cho, K. Y., Fugger, C. A., Fievisohn, R. T., Sell, B. C., Hoke, J. L., Kearney, S. P., Caswell, A. W., Gord, J. R., and Schauer, F. R. "Burst-Mode 355 Nm Plif for Detonation Wave Front Visualization and 100–300 Khz Particle Image Velocimetry." *AIAA Scitech 2019 Forum*, No. January, 2019, pp. 1–14. https://doi.org/10.2514/6.2019-2249.

[18] Grib, S., Fugger,C., Hsu, P., Jiang, N., Roy, S., and Schumaker, S. "Two-dimensional Temperature in a Detonation Channel using Two-color OH Planar-laser Induced Fluorescence Thermometry." *Combustion and Flame* (submitted)

[19] Y. Kudo, Y. Nagura, J. Kasahara, Y. Sasamoto, and A. Matsuo, "Oblique detonation waves stabilized in rectangular-cross-section bent tubes," *Proc. Combust. Inst.*, vol. 33, no. 2, pp. 2319–2326, 2011, doi: 10.1016/j.proci.2010.08.00

[20] H. Nakayama, T. Moriya, J. Kasahara, A. Matsuo, Y. Sasamoto, and I. Funaki, "Stable detonation wave propagation in rectangular-cross-section curved channels,"

Combust. Flame, vol. 159, no. 2, pp. 859–869, 2012, doi: 10.1016/j.combustflame.2011.07.022.

[21] Fotia, M. L., Hoke, J., Olson, A. J., Schumaker, S. A., "PROPAGATION OF GASEOUS DETONATIONS IN PLANAR CURVED RECTANGULAR CHANNELS," presented at theInternational Colloquium on Pulsed and Continuous Detonations, St. Petersburg, Russia, Oct. 19-22, 2020.

[22] M.H. Fernelius, B.C. Sell, K.J. Moosmann, J.L. Hoke, I.Q. Andrus, F.R. Schauer, Characterization of a premixed laboratory scale pulsed detonation burner, AIAA SciTech. (2018) 1–12.

[23] R. Knystautas, C. Guirao, J.H. Lee, and A. Sulmistras. Measurement of cell size in hydrocarbon-air mixtures and predictions of critical tube diameter, critical initiation energy, and detonability limits. In *Prog. Astronaut. Aeronaut.*, volume 94, pages 23-37, 1984.

[24] S.R. Tieszen, M.P. Sherman, W.B. Benedick, J.E. Shepherd, R. Knystautas, and J.H.S. Lee. Detonation cell size measurements in hydrogen-air-steam mixtures. In *Prog. Astronaut. Aeronaut.*, volume 106, pages 205-219, 1986.

[25] G. Ciccarelli, T. Ginsberg, J. Boccio, C. Economos, K. Sato, and M. Kinoshita. Detonation cell size measurements and predictions in hydrogen-air-steam mixtures at elevated temperatures. *Combust. Flame*, 99(2):212-220, 1994.

[26] Nikolai Chernov (2021). Circle Fit (Taubin method) (https://www.mathworks.com/matlabcentral/fileexchange/22678-circle-fit-taubin-method), MATLAB Central File Exchange. Retrieved February 20, 2021

[27] M.J. Kaneshige. Gaseous Detonation Initiation and Stabilization by Hypervelocity Projectiles. PhD thesis, California Institute of Technology, 1999.

[28] R.K. Kumar. Detonation cell widths in hydrogen-oxygen-diluent mixtures. Combust. Flame, 80(2):157-169, 1990.

[29] EDL. Califonia Institute of Technology, unpublished.

Vita

OPTIONAL

REPORT DOCUMENTATION PAGE

Form Approved
OMB No. 074-0188

1. REPORT DATE *(DD-MM-YYYY)*	**2. REPORT TYPE**	**3. DATES COVERED** *(From – To)*
25-03-2021	Master's Thesis	August 2019 – March 2021

TITLE AND SUBTITLE

Optical Study of 2-D Detonation Wave Stability

5a. CONTRACT NUMBER

5b. GRANT NUMBER

5c. PROGRAM ELEMENT NUMBER

6. AUTHOR(S)

Grodner, Eulalie T., First Lieutenant, USAF

5d. PROJECT NUMBER

5e. TASK NUMBER

5f. WORK UNIT NUMBER

7. PERFORMING ORGANIZATION NAMES(S) AND ADDRESS(S)
Air Force Institute of Technology
Graduate School of Engineering and Management (AFIT/EN)
2950 Hobson Way, Building 640
WPAFB OH 45433-7765

8. PERFORMING ORGANIZATION REPORT NUMBER

AFIT-ENY-MS-15-M-043

9. SPONSORING/MONITORING AGENCY NAME(S) AND ADDRESS(ES)
Alex Shumaker PhD
AFRL/RQTC
(w) 937-255- 3252
(e) stephen.schumaker.1@us.af.mil

10. SPONSOR/MONITOR'S ACRONYM(S)

AFRL/RQTC

11. SPONSOR/MONITOR'S REPORT NUMBER(S)

12. DISTRIBUTION/AVAILABILITY STATEMENT
DISTRUBTION STATEMENT A. APPROVED FOR PUBLIC RELEASE; DISTRIBUTION UNLIMITED.

13. SUPPLEMENTARY NOTES
This material is declared a work of the U.S. Government and is not subject to copyright protection in the United States.

14. ABSTRACT

Fundamental optical detonation study of detonations constricted to a 2-d plane propagation, and detonations propagating around a curve. All images were processed using modern image processing techniques. The optical techniques used were shadowgraph, schlieren, and chemiluminescence. In the 2-D straight channels, it was determined wave stability was a factor of cell size. It was also determined the detonation wave thickness (area between the combustion and shockwave) was a factor of how much heat available for the detonation. For the detonations propagating around a curve, it was determined the three main classifications of wave stability were stable, unstable, and detonation wave restart. The detonation wave restart was classified as having a DDT event occur. A stability regime was created for hydrogen-air detonations with the ability to propagate across a curve, the channel possessed 4 or more cells, and stable waves preferred having smaller cells. Overall, it was determined wave stability was a factor of cell size.

15. SUBJECT TERMS
Detonation, high-speed imaging, optics, image processing, 2-d channels

16. SECURITY CLASSIFICATION OF: A			**17. LIMITATION OF ABSTRACT**	**18. NUMBER OF PAGES**	**19a. NAME OF RESPONSIBLE PERSON**
a. REPORT	**b. ABSTRACT**	**c. THIS PAGE**			Maj Levi Thomas, AFIT/ENY
U	**U**	**U**	**UU**	165	**19b. TELEPHONE NUMBER** *(Include area code)* (937) 257-3636, ext 4500 (NOT DSN) (levi.thomas@afit.edu)

Standard Form 298 (Rev. 8-98)
Prescribed by ANSI Std. Z39-18